Università degli Studi di Pavia
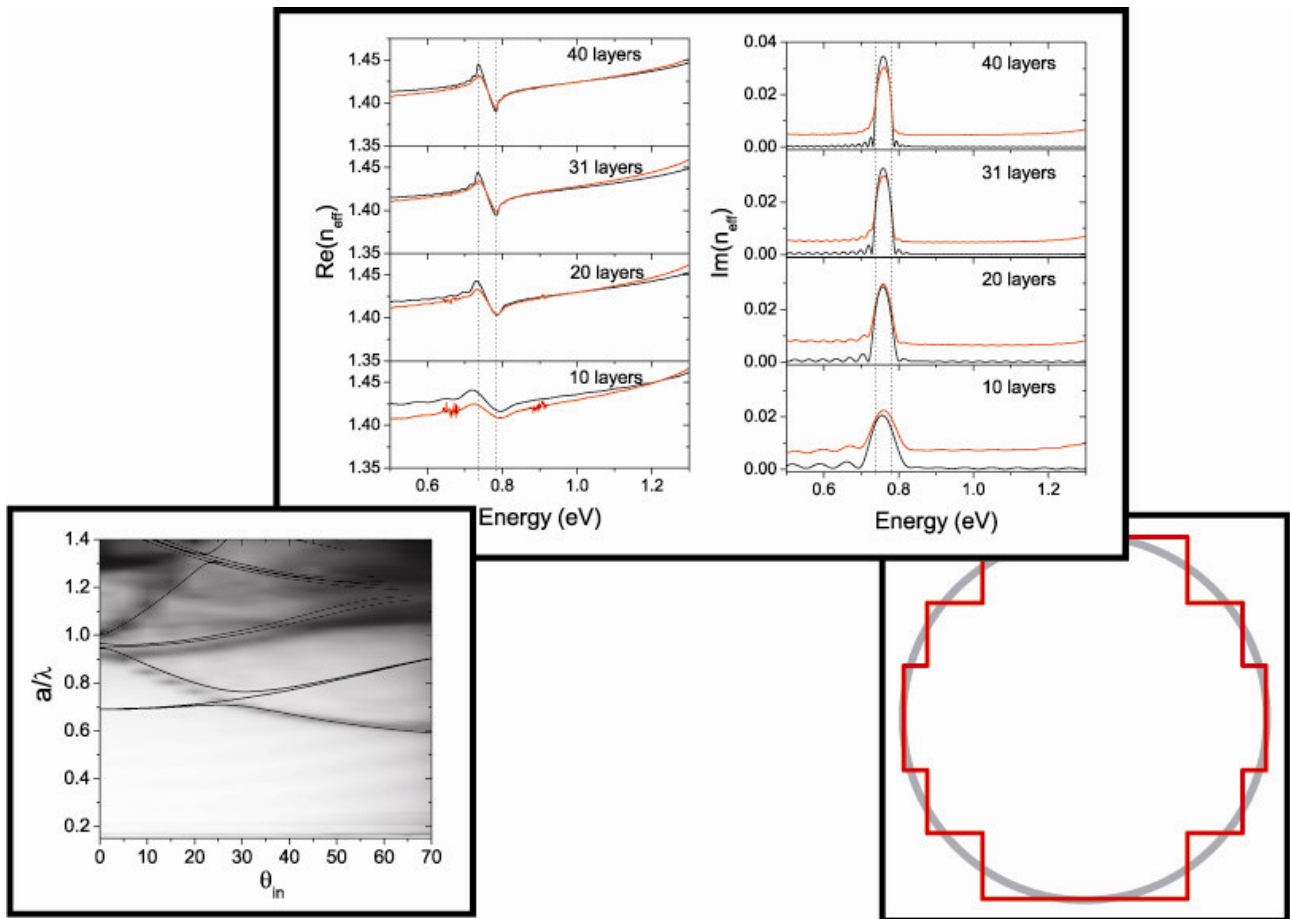## Dottorato di Ricerca in Fisica – XX Ciclo

Optical properties
of opal-based photonic crystals

Alessandra Balestreri

Supervisor: Prof. L. C. Andreani

Tesi per il conseguimento del titolo

UNIVERSITÀ DEGLI
STUDI DI PAVIA

DIPARTIMENTO DI
FISICA "A. VOLTA"

DOTTORATO DI RICERCA IN FISICA - XX CICLO

Optical properties of opal-based photonic crystals

dissertation submitted by

Alessandra Balestreri

to obtain the degree of

DOTTORE DI RICERCA IN FISICA

Supervisor: Prof. L. C. Andreani
Referee: Prof. V. N. Astratov

Cover

Top: Real and imaginary part of the effective refractive index estimated from the absolute phase delay and the transmission coefficient for polystyrene opals of different thicknesses. Experimental and theoretical data are presented. More details can be found in Fig. 3.4 of this thesis.

Bottom left: Contour plot of experimental transmittance spectra with respect to the incidence angle for a polystyrene opal whose horizontal layers are oriented along [100] direction of face centered cubic lattice. In black line band structure calculation obtained by means of plane wave expansion. More details can be found in Fig. 5.12(a) of this thesis.

Bottom right: A schematic view of the five cylinder approximation used in this thesis work to retrieve optical spectra for thin opal films by means of scattering matrix method. More details can be found in Chapt. 2.

Non chiederci la parola che squadri da ogni lato
l'animo nostro informe, e a lettere di fuoco
lo dichiari e risplenda come un croco
perduto in mezzo a un polveroso prato.

Ah l'uomo che se ne va sicuro,
agli altri ed a se stesso amico,
e l'ombra sua non cura che la canicola
stampa sopra uno scalcinato muro!

Non domandarci la formula che mondi possa aprirti
sì qualche storta sillaba e secca come un ramo.
Codesto solo oggi possiamo dirti,
ciò che non siamo, ciò che non vogliamo.

(E. Montale, *Ossi di Seppia*, 1925)

Contents

Introduction

In recent years a great deal of attention has been devoted towards photonic materials. The technology of photons, named photonics in analogy with electronics, has become the driving force for the advancement of areas such as communications and computing, information technology and even biotechnology, for sensing devices.

An answer to the many demands that arise in the previously cited resarch fields can be photonic crystals (PhCs). They are the optical analogous of ordinary crystals, since their periodicity in refractive index determines a structure of allowed and forbidden bands for the light frequency dispersion with respect to the wavevector inside the structure. When light propagation is inhibited for any polarization and any direction inside the crystal a complete photonic bandgap is achieved. Due to the analogy between PhCs and ordinary crystals, the study of these artificial materials took advantage of concepts well known in solid state physics, with the aim of investigating photonic band structure and optical spectra and of realizing functional devices.

As it has been firstly suggested in the works of Yablonovitch [1] and John [2], to obtain a complete control on light propagation, three dimensional (3D) PhCs are the most appropriate structures to deal with. Nevertheless, the realization of optical devices can be achieved even by one or two dimensional structures.

Bragg mirrors, constituted by a periodic stacking of thin dielectric layers usually of optical thickness $\lambda/4$, λ being the light wavelength, are the most common example of one dimensional PhCs. A planar defect embedded between two of these mirrors acts as an optical microcavity, leading to an enhancement of the field intensity in the cavity region. Bragg mirrors have been studied also as non-linear materials, as an example for second harmonic generation [3, 4, 5, 6]. One dimensional structures do not allow the control of light propagation on three dimensions, on the contrary light is confined just along the direction perpendicular to the stacking. Thus the effectiveness of Bragg mirrors depends strongly on incidence angle for light impinging on the layer surface: far from normal incidence the reflectivity is very low and the device behaves

as a transparent medium.

More difficult to realize, two dimensional PhCs stand out for the possibility of being applied to integrated optics and to the so-called photonic circuits. As a matter of fact these materials can be fabricated exploiting techniques well known in electronic, such as photo- or electron beam lithography, to realize optical devices [7]. Among all two dimensional structures, PhCs slabs [8] are one of the most promising devices to be employed in integrated circuits. In these systems light is confined in the plane by the photonic structure and in the perpendicular direction by total internal reflection due to the dielectric discontinuity of the slab. By inserting a line or a point defect in such a crystal, one can obtain a waveguide or an optical cavity, respectively [9, 10, 11, 12]. These can be the starting point to realize a planar integrated photonic circuit, similar to an electronic one, realized on a silicon wafer. The difficulty lies on avoiding out of plane losses, due to the fact that light is only partially confined in the vertical direction [13, 14, 15, 16]. Nevertheless these losses allow to study the photonic band structure of these systems by means of reflectivity techniques [17, 18]. Another important class of two dimensional PhCs are photonic fibers, which basically consist of a pure silica core surrounded by a silica-air PhC-like material with a two dimensional pattern [19, 20, 21]. The frequency of the guided mode lies within the band gap of the photonic structure, hence its confinement is highly enhanced.

Concerning 3D systems, the realization of a structure presenting a complete photonic band gap has attracted a large community of scientists. The first success in this field was the proposal of Yablonovitch [1] of a material presenting a face centered cubic (fcc) lattice of non-spherical objects, obtained by drilling holes in a bulk dielectric material. Afterwards, different attempts have been made in order to fabricate artificial materials presenting a three dimensional pattern. Among these, artificial opals are readily available 3D PhCs as they can be produced with easy and low cost processes based on self-assembly from colloidal solutions, such as natural sedimentation or vertical deposition.

Bare opals consist of dielectric spheres arranged in a close-packed fcc lattice oriented along the [111] crystallographic direction and they may be infiltrated with high-index materials to obtain the so-called inverse opals. The latter, provided that the index contrast is high enough, present a complete photonic band gap as it has been demonstrated both theoretically [22] and experimentally [23]. A large scientific community has investigated the optical properties of opal-based PhCs and they have been increasingly well known over the years. Many interesting issues can be studied in these structures: to name only a few, we can list superprism effects [24], superluminality [25, 26, 27, 28, 29], diffraction phenomena [27, 30, 31, 32, 33] and the control of spontaneous emission [34, 35, 36, 37].

The first works were concerned with the fundamental stop band and its evolution as a function of incidence angle, with multiple peaks related to diffrac-

2

tion appearing at high angles. The advancements in self-assembly fabrication, which lead to high-quality crystals, give the possibility to probe the optical properties in the regions around and above the second-order stop band, otherwise hidden by disorder and imperfections, where diffraction effects due to higher-order crystalline planes come into play. A theoretical description of the optical properties including diffraction in the high energy region is needed in order to understand the specific features of these systems.

The aim of the present work is to introduce a reliable theoretical model that allows to calculate optical spectra of opal-based PhCs to be compared to experimental measurements. As a matter of fact many methods, such as scalar wave approximation, Korringa-Kohn-Rostoker method, transfer matrix and Finite Difference Time Domain, have been applied to the study of these materials especially in the low energy region. Most of this methods fails in giving results in the high energy region, or, at least, result in a time-consuming code. Our approach allow retrieving the optical properties of bare opals even above diffraction threshold, when the light wavelength involved is comparable to lattice constant, without any free parameters, provided that the dielectric contrast is not to large.

The original codes used in this thesis were developed within the group of Prof. L. C. Andreani at *Dipartimento di Fisica "A. Volta"* of *Università di Pavia*. In particular the scattering matrix code is due to Dr. M. Agio. Proper modifications in order to adapt the codes to the present research subject have been introduced.

Experimental measurements presented in the thesis have been mainly realized by Dr. M. Galli, Dr. J. F. Galisteo López and Dr. M. Patrini in the Optical Spectroscopy Laboratory at *Dipartimento di Fisica "A. Volta"* of *Università di Pavia*. The samples whose measurements are presented in Chapt. 3 and Chapt. 5 have been grown at *Instituto de Ciencia de Materiales (ICMM)* in Madrid by the group of Prof. C. López.

The work has been organized in six chapters:

- In the first Chapter an overview on the fundamental concepts that characterize PhCs is presented. Their physical properties are analysed in term of photonic band dispersion. Afterwards we restrict ourselves to three dimensional structures, introducing the state of the art on opal-based PhCs.

- The theoretical approach exploited in this work is explained in Chapt. 2. Basically, after a description of the crystallographic structure of opals, we present the plane-wave expansion and the scattering matrix, the methods used to calculate the photonic band structure and the optical properties such as reflectance and transmittance, respectively. The last section is dedicated to the staircase approximation introduced to apply the scattering matrix scheme to opal-based PhCs.

- Chapter 3 deals with the optical properties of colloidal crystals in the energy region of the first pseudogap. Firstly results on transmission and optical phase delay at normal incidence, varying sample thickness, are presented. From these two quantities group velocity and effective refractive index are derived and analysed in detail. All the data derived from numerical simulations are compared with experimental measurements. In the second section, optical properties for finite incidence angle along ΓW direction are investigated, analysing also the role of mixing between TE and TM polarization with respect to ΓLW plane in the first Brillouin zone. Finally we study the threefold symmetry of the L point of the fcc lattice: this property can be verified in opals grown along [111] direction, with their hexagonal faces parallel to sample surface.

- Chapter 4 is addressed to photonic band structure calculations, obtained by means of a supercell method. This scheme gives the possibility to investigate the optical properties of a thin opal film, which can be very different from those of a bulk PhC and to analyse the frequency dispersion of an opal-based PhC wherein a planar defect has been introduced.

- Diffraction in opal PhCs is the subject of the last chapter, as this is the phenomenon that dominated the optical behaviour of opals in the high energy region. The first two sections deal with the dependence of diffraction and transmission features on sample thickness. The Pendellösung effect is a mutual interchange of energy between transmitted and diffracted beam and it take place above diffraction threshold. In the same energy region, when a dip in transmission occurs, for instance in the second order stop band, a change from slow to superluminal behaviour can be observed varying the number of layers, as explained in Sect. 5.2. Finally, the study of optical properties of a sample whose growth is oriented along [100] direction is presented: it can be seen that the spectra are strongly influenced by the presence of diffraction.

Chapter 1

Three-dimensional photonic crystals: generalities and state of the art

In this Chapter we would like to introduce the basic concepts that characterize a particular class of periodic metamaterials, called photonic crystals (PhCs). After a presentation of their physical properties we will restrict ourselves to three dimensional (3D) PhCs, and finally we will present the state of the art on self-assembled colloidal crystals, which are the subject of the present thesis work.

1.1 The photonic band structure

PhCs are a class of artificial materials in which the dielectric function undergoes a spatially periodic variation in either one, two or three directions: a simple example is shown in Fig. 1.1. The length scale of this variation determines the spectral range of interaction between the electromagnetic wave and the structure itself.

There are strong analogies between photonic and ordinary crystals. The spatial variation of dielectric function gives rise to effects on photons similar to those generated by periodic atomic potential on electrons. Reflection occurring at the interface between two different dielectric materials can create stationary waves, due to constructive interference, and, consequently, photonic band gaps (PBGs) and a photonic band structure analogous to the electronic one, well-known in solid state physics [39, 40]. In particular, we can speak of a complete PBG if a PhC can forbid light propagation in a specific range of frequencies independently of propagation direction and polarization. A three dimensional periodicity is needed in order to have a zero density of photonic states for a certain frequency range, condition that leads to a complete PBG.
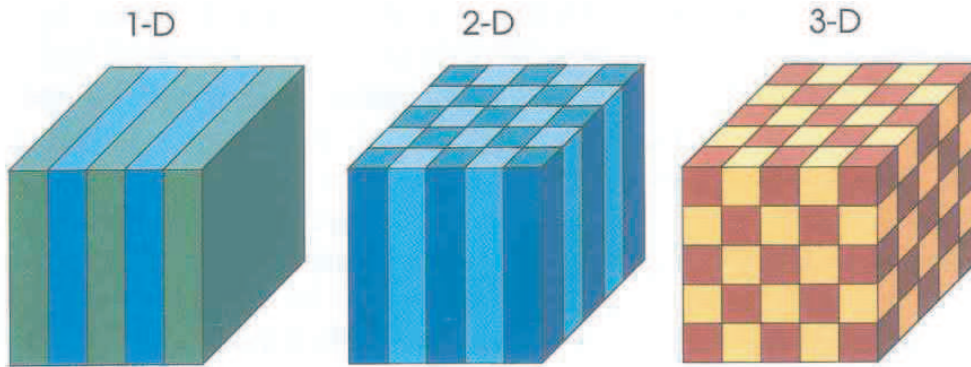
Figure 1.1: Examples of one, two and three dimensional PhCs [38].

The simplest examples of this kind of meta-materials are the so called Distributed Bragg Reflectors (DBRs), i.e. dielectric mirrors constituted by a periodic multilayer. These systems present a reflectivity very close to unity in a specific range of frequencies (determined by the lattice constants and the dielectric contrast) and incidence angles, due to constructive interference of the reflected beams at every single interface. Hence DBRs have been extensively used as dielectric mirrors since the 50s [41]. Up to here we explained the behaviour of these objects only by using geometrical optics; changing the point of view, we can examine DBRs as one-dimensional PhCs and study their frequency dispersion $\omega(\mathbf{k})$ where ω and $\mathbf{k}$ are respectively the frequency and the wavevector of light propagating inside the crystal. In particular, carrying on the comparison with solid-state physics we can trace back the problem to the Kronig-Penney model [40], remembering that the role of atomic potential has been taken by dielectric function. For certain energy ranges no purely real solutions exist and the wavevector has a non-vanishing imaginary part, meaning that the wave undergoes attenuation and does not propagate through an infinite crystal, but can only be reflected at the surface. The situation is illustrated in Fig. 1.2, where the opening of a PBG can be observed for increasing values of dielectric contrast.

PhCs were first proposed in the works of Yablonovitch [1] and John [2] at the end of the 1980s, relating their optical properties to the photonic band structure. In the first of these two works the author studies the role of a complete PBG, overlapping the electronic band gap, in suppressing spontaneous emission, while in the other paper a new mechanism for strong Anderson localization is predicted to take place in periodic structures with a specific amount of disorder. Both papers deals with a periodic spatial variation of dielectric function in three dimensions, more suitable in producing a complete PBG, as written before. Since then a large amount of work has been done in this particular research field. Besides the thousands of papers that have been published during these twenty years, there are also some books that give a complete
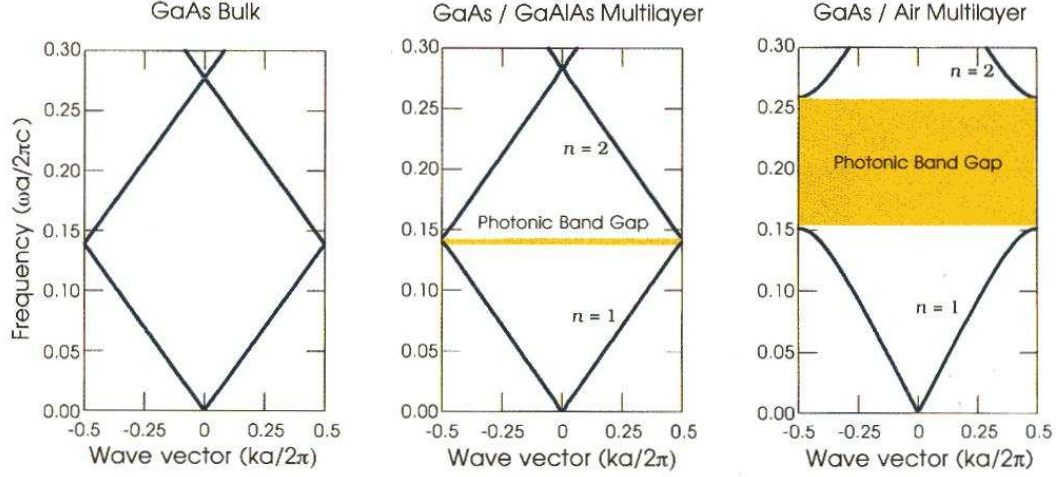
Figure 1.2: The photonic band dispersion for on-axis propagation for three different multilayer films having layers $of 0.5a$. On the left the empty lattice model with a dielectric constant $\varepsilon = 13$ is shown, in the center panel the band structure of alternate layers of dielectric functions $\varepsilon_1 = 13$ and $\varepsilon_2 = 12$ and, on the right, of dielectric functions $\varepsilon_1 = 13$ and $\varepsilon_2 = 1$ is presented [38].

overview of the problem. To name a few, we cite the two of them written by Joannopoulos's group [38, 42], the one by Sakoda [43] and some others that give a complete overview both from a theoretical and experimental point of view [44, 45, 46].

To study the optical properties of PhCs one has to start from Maxwell equations (in cgs units) in a dielectric medium, assuming that free charges and electric currents are absent:

$$\nabla \cdot \mathbf{D}(\mathbf{r}, t) = 0, \tag{1.1a}$$

$$\nabla \cdot \mathbf{B}(\mathbf{r}, t) = 0, \tag{1.1b}$$

$$\nabla \times \mathbf{E}(\mathbf{r}, t) = -\frac{1}{c}\frac{\partial}{\partial t}\mathbf{B}(\mathbf{r}, t), \tag{1.1c}$$

$$\nabla \times \mathbf{H}(\mathbf{r}, t) = \frac{1}{c}\frac{\partial}{\partial t}\mathbf{D}(\mathbf{r}, t); \tag{1.1d}$$

$\mathbf{E}$ and $\mathbf{H}$ are, respectively, the electric and magnetic field, while $\mathbf{D}$ and $\mathbf{B}$ are the displacement and magnetic induction fields. Since we do not deal with magnetic media, we can assume that the magnetic permeability μ is equal to unity, as in free space. Restricting ourselves to the linear regime and considering materials whose dielectric function is frequency independent, we can write the two following constitutive equations:

$$\mathbf{D}(\mathbf{r}, t) = \varepsilon(\mathbf{r})\mathbf{E}(\mathbf{r}, t), \tag{1.2}$$

$$\mathbf{B}(\mathbf{r}, t) = \mathbf{H}(\mathbf{r}, t). \tag{1.3}$$

Assuming a harmonic time dependence for both the magnetic and electric fields

$$
\begin{aligned}
\mathbf{H}(\mathbf{r}, t) &= \mathbf{H}(\mathbf{r})e^{-i\omega t}, \\
\mathbf{E}(\mathbf{r}, t) &= \mathbf{E}(\mathbf{r})e^{-i\omega t},
\end{aligned}
\tag{1.4}
$$

we can rewrite Maxwell equations (1.1) in the following way:

$$
\nabla \cdot \mathbf{D}(\mathbf{r}) = 0 \,,
\tag{1.5a}
$$

$$
\nabla \cdot \mathbf{H}(\mathbf{r}) = 0 \,,
\tag{1.5b}
$$

$$
\nabla \times \mathbf{E}(\mathbf{r}) = -\frac{i\omega}{c}\mathbf{H}(\mathbf{r}) \,,
\tag{1.5c}
$$

$$
\nabla \times \mathbf{H}(\mathbf{r}) = \frac{i\omega}{c}\varepsilon(\mathbf{r})\mathbf{E}(\mathbf{r}) \,.
\tag{1.5d}
$$

There are two ways to decouple this set of equations. On one hand, we can write a master equation for the electric field $\mathbf{E}$ and subsequently derive the magnetic field $\mathbf{H}$:

$$
\nabla \times \nabla \times \mathbf{E}(\mathbf{r}) = \frac{\omega^2}{c^2}\varepsilon(\mathbf{r})\mathbf{E}(\mathbf{r}) \,,
\tag{1.6a}
$$

$$
\mathbf{H}(\mathbf{r}) = -i\frac{c}{\omega}\nabla \times \mathbf{E}(\mathbf{r}).
\tag{1.6b}
$$

On the other hand, we can write an equation for the magnetic field and then obtain the electric field:

$$
\nabla \times \left[\frac{1}{\varepsilon(\mathbf{r})}\nabla \times \mathbf{H}(\mathbf{r})\right] = \frac{\omega^2}{c^2}\mathbf{H}(\mathbf{r}) \,,
\tag{1.7a}
$$

$$
\mathbf{E}(\mathbf{r}) = i\frac{c}{\omega}\frac{1}{\varepsilon(\mathbf{r})}\nabla \times \mathbf{E}(\mathbf{r}).
\tag{1.7b}
$$

It is better to solve equation (1.7a) as it is an eigenvalue equation with a hermitian operator. The exact solutions, apart from numerical approximation, can be found by means of a variety of methods, the most widely used one being plane wave expansion, described in Chapter 2.

When dealing with ordinary crystals, the electronic band structure is determined starting from Schrödinger equation with a periodic potential, due to discrete translational symmetry. The Bloch theorem, well known in solid state physics, states that the eigenvectors of such an equation can be written as a plane wave modulated by a function with the same periodicity as the potential. Also in PhCs there is a discrete translational symmetry:

$$
\varepsilon(\mathbf{r} + \mathbf{a}_i) = \varepsilon(\mathbf{r}),
\tag{1.8}
$$

where $\mathbf{a}_i$ are the elementary lattice vectors. Hence the Bloch-Floquet theorem, the optical analogous of Bloch theorem, holds for any component of the fields and we can write the solutions of master equation (1.7a) as:

$$
\Psi_{n\mathbf{k}}(\mathbf{r}) = e^{i\mathbf{k}\cdot\mathbf{r}}u_{n\mathbf{k}}(\mathbf{r}) \,,
\tag{1.9}
$$

where n is the index identifying the eigenvectors of the hermitian operator involved in the master equation for magnetic field. $u_{n\mathbf{k}}(\mathbf{r})$ is a function with the same periodicity as the lattice:

$$u_{n\mathbf{k}}(\mathbf{r} + \mathbf{R}) = u_{n\mathbf{k}}(\mathbf{r}). \tag{1.10}$$

Once again there is a strong analogy between electronic and photonic features.

An interesting characteristic of PhCs is the scale invariance. Suppose, as an example, to have an electromagnetic mode $\mathbf{H}(\mathbf{r})$ of frequency ω in a dielectric configuration $\varepsilon(\mathbf{r})$. We recall the master equation (1.7a):

$$\nabla \times \left(\frac{1}{\varepsilon(\mathbf{r})} \nabla \times \mathbf{H}(\mathbf{r}) \right) = \frac{\omega^2}{c^2} \mathbf{H}(\mathbf{r}). \tag{1.11}$$

Now we want to study the harmonic modes in a configuration that is just a compressed or expanded version of $\varepsilon(\mathbf{r})$, $\varepsilon'(\mathbf{r}) = \varepsilon(s\mathbf{r})$, for a scale parameter s. Changing the variables in a proper way, with $\mathbf{r}' = s\mathbf{r}$, we obtain:

$$s\nabla' \times \left(\frac{1}{\varepsilon(\mathbf{r}'/s)} s\nabla' \times \mathbf{H}(\mathbf{r}'/s) \right) = \frac{\omega^2}{c^2} \mathbf{H}(\mathbf{r}'/s). \tag{1.12}$$

Dividing out the scale factor s we find:

$$\nabla' \times \left(\frac{1}{\varepsilon'(\mathbf{r}')} \nabla' \times \mathbf{H}(\mathbf{r}'/s) \right) = \frac{(\omega/s)^2}{c^2} . \mathbf{H}(\mathbf{r}'/s), \tag{1.13}$$

that is, if we want to know the mode profile after changing the length scale by a factor s we just scale the old mode and its frequency by the inverse of the same factor. This property, that does not have a counterpart in ordinary crystals, allows us to plot photonic band structure in dimensionless units: the most common is $\omega a/2\pi c = a/\lambda$, where a is the lattice constant and λ the wavelength in vacuum. From an experimental point of view, one can easily build PhC samples in a millimeter range scale and test them in the microwave regime, before fabricating samples with smaller size, that are usually more difficult and expensive. Besides the scalability in space there is a scalability in the dielectric function: two systems whose dielectric functions scale by a factor $\varepsilon'(\mathbf{r}) = \varepsilon(\mathbf{r})/s^2$ have the dispersion relation scaled by the same factor: $\omega' = s\omega$.

As well as one of the greatest advantage of semiconductors in electronics is the fact that their conduction properties can be strongly modified by doping, PhCs achieve their highest functionalities once defects are introduced in a controlled manner. In particular, depending on the periodicity of the PhC, planar, linear or point defect can be defined in order to create the analogous of impurity states in semiconductors, presenting interesting physical properties.

In one dimensional PhCs a planar defect can be embedded in the periodic stacking by varying the thickness or the refractive index of a single layer. This

structure breaks the discrete translation symmetry along the stacking direction and it give rise to a photonic state that, if it is properly tuned, may have a frequency inside a stop band. The defect mode is usually localized inside the defect in real space, with an evanescent field on both sides of the layers. This state correspond to a Fabry-Pérot mode inside a dielectric microcavity, embedded in two Bragg mirrors.

Dealing with two dimensional structures, we can introduce a point or line defect. The first one corresponds to a situation similar to that analysed in the previous paragraph, with the defect acting as a cavity inside the crystal. On the other hand a line defect behaves as a waveguide for light inside the crystal, since the photonic mode have an imaginary component of the wavevector in the direction perpendicular to the defect, resulting in an evanescent field on both sides of it, and a real component that allows propagation along the defect itself.

Finally, in 3D PhCs it is possible to realize all the kinds of defects described before. In particular the case of a planar defect will be treated in detail in Chapt. 4, analysing the localization of the defect state by means of a supercell approach. Moreover a point defect tuned in order to produce an allowed state inside a complete PBG will give rise to a three dimensional optical cavity, able to trap the light inside the crystal. Placing an emitter within this cavity gives the possibility to study the modifications on radiation decay, due to a strong change of the three dimensional density of states. As we will see in next Sect. 1.3, this effect has been investigated in artificial opals.

1.2 Three-dimensional photonic crystals

Since their first proposal, a great attention has been devoted towards the fabrication of three-dimensional (3D) PhCs, since in principle they give the possibility of having a complete PBG. The task was not a trivial one, especially when dealing with samples working in the optical regime, due to reduced dimensions. Nowadays there are several examples of 3D PhCs, which can be classified in two sets, according to the fabrication method. They can be realized by means of top-down methods, such as lithography, holography and micromanipulation; otherwise they can be grown with self-assembly techniques, also known as bottom-up methods. In the following we will briefly describe some of the structures that can be built with these two techniques.

1.2.1 Top-down fabrication methods

The first realization of a crystal with a complete PBG was performed by Yablonovitch [47]. The samples were fabricated drilling three tilted holes 35.26 degrees off vertical in each position of an hexagonal lattice marked on the surface of a block of low loss dielectric material. The structure obtained is a face centered cubic (fcc) lattice with a basis of non spherical atoms and has
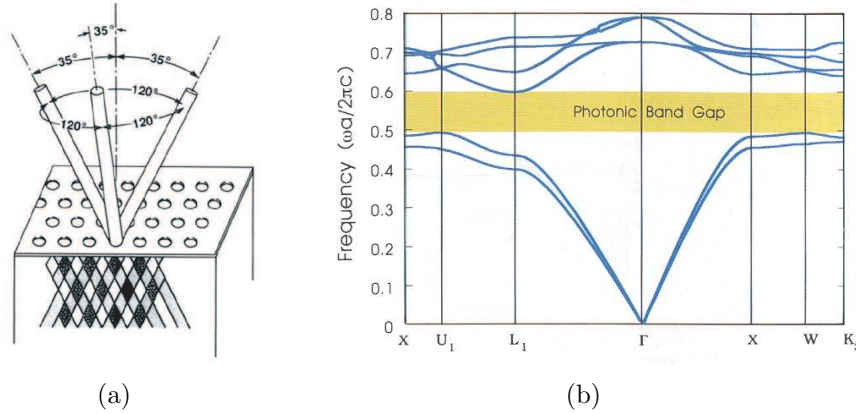
Figure 1.3: (a) Schematic view of the procedure that leads to yablonovite [47]. (b) Photonic band structure of yablonovite: the complete PBG is highlighted in yellow [38].

taken the name of Yablonovite, in its inventor's honor. A view of the drilling directions is illustrated in Fig. 1.3(a), together with the photonic band structure that presents a complete PBG, shown in Fig. 1.3(b). The first samples, with millimeter-size holes, were conceived to work in the microwave regime, more suitable for fabrication and measurements. Exploiting the scalability of photonic band structure, from then on many efforts have been devoted to realize similar structures working in the telecommunications or optical regime [48, 49, 50, 51, 52].

A way to proceed in the fabrication of 3D structures is to implement those techniques that are well-known in microelectronics, such as photolithograpy and electron beam lithography in a layer by layer approach. A famous example of this method is the woodpile structure [53, 54], shown in Fig. 1.4(a). The process consisted in defining a 1D array of bars in a thin layer of Silicon, the empty space among which is subsequently backfilled with silica and planarized. A second layer of Si is deposited and the process is repeated, drawing the bars perpendicular with respect to the previous layer. These are backfilled and planarized and the process starts over again. Finally the silica is removed with selective etching and a 3D structure is obtained. A similar technique leads to the realization of an fcc structure of cylinders [55], shown in Fig. 1.4(b): two layers (one hole layer and one rod layer) are fabricated in one process cycle, which consists of material deposition, aligned lithography, etching and planarization. As a result, seven functional layers can be achieved in four process cycles. Defects can been introduced during growth, a very important feature for technological applications.

Holographic techniques have been studied as being able to produce extended regions of PBG materials [56, 57, 58, 59, 60, 61]. In those processes several beams are made to interfere in the presence of a photosensitive resist creating a pattern, fixed by polymerization. If four non-collinear beams are
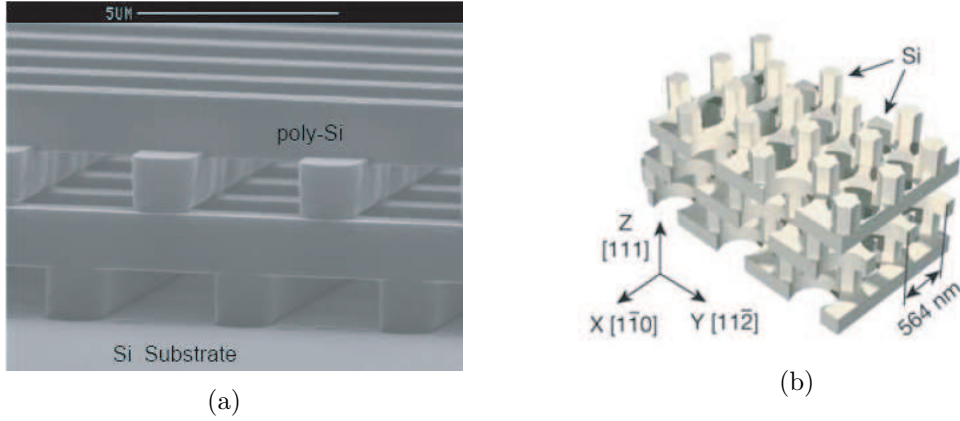
(a) (b)

Figure 1.4: Examples of woodpile structure [53] and of an fcc lattice made by cylinders [55].

considered a 3D pattern is obtained. The period and the geometrical lattice of the structure are determined by laser wavelength, relative phases and incidence directions of of the beams, while the shape of the lattice basis is the result of beam polarization.

Recently, robot manipulation allowed the realization of a diamond lattice structure made of microspheres [62]. Two sets of microspheres, made respectively of latex and silica, are arranged by means of a nano-robot in two interpenetrating diamond lattices, giving rise to a body centered cubic structure. Latex spheres, acting as a scaffold for the silica structures, are removed after growth to obtain a single diamond lattice.

1.2.2   Bottom-up fabrication methods

Self-assembly techniques are widely studied and used to fabricate 3D structures, because they are essentially inexpensive and they do not need complicated processes [63]. They are based on the natural tendency of micrometric colloidal particles of silica, polystyrene or polymethilmetacrylate to self assemble in a ordered fcc lattice. An SEM image of a bare opal made of polystyrene spheres is shown in Fig. 1.5(a). The counterpart of these methods is the unavoidable degree of disorder present in the samples: among the known causes of such a phenomena, we mention the polydispersity in size of the microspheres and the inherent stacking defects developed during the deposition process [64]. Many attempts have been made to improve the quality of the final samples and this led to a variety of growing techniques such as sedimentation [65], even on a patterned substrate [66], vertical deposition [67, 68], or confinement in special cell [69, 70].

The most widely used is vertical deposition, that basically consists in submerging a flat substrate in a diluted colloidal suspension and allowing the solvent to evaporate. The forces intervening at the meniscus allow the growth
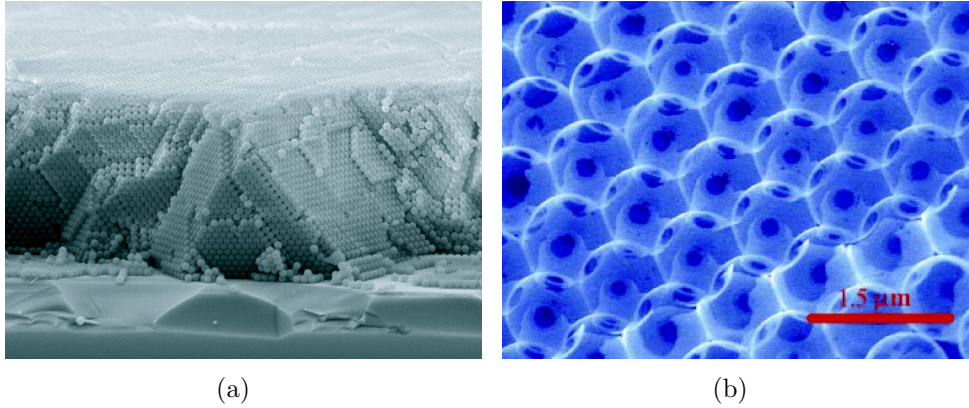
(a)   (b)

Figure 1.5: Scanning Electron Microscope (SEM) images of direct (courtesy of Dr. Galisteo-López) and inverse opals [23].

of a close packed lattice of microspheres. Spinning techniques can be applied to obtain a rapid fabrication in large scale, at the price of lowering sample quality [71]. A way to decrease the disorder in samples is to direct the natural sedimentation starting from a patterned substrate, that allows the microsphere to be placed in the correct position avoiding stacking faults, vacancies, or lattice relaxation. This process allows to grow samples oriented along directions different from [111], that is the natural tendency of sedimentation [72].

An important issue of opal fabrication is the infiltration of the bare structure by high-index materials, leading to the so-called inverse opals shown in Fig. 1.5(b). As a matter of fact, it has been demonstrated that a complete PBG can open in these crystals, on the condition that index contrast is high enough [22]: this is the situation illustrated in Fig. 1.6. Usually infiltration is done by chemical vapor deposition, a technique well suited for using semiconductors as silicon and germanium, materials with high dielectric function. In order to increase the refractive index contrast the silica or latex spheres of the template are removed by selective etching [73, 74, 75, 23, 68] . Inverse opals can be obtained also by filling a bare opal with a precursor of TiO_2 by precipitation from a liquid-phase chemical reaction and then heating the sample to form anatase Titania and to remove the latex template [76].

Another great advantage of colloidal crystals is the possibility of introducing controlled defects, leading to the formation of localized states, possibly in a forbidden energy region [77]. A number of different approaches for the fabrication of defects in colloidal crystals have been used by different groups. These can go from conventional photolithography based methods or direct laser writing and direct surface writing for point or line defects, spin coating techniques [78, 79] to Langmuir-Blodgett growth [80, 81].
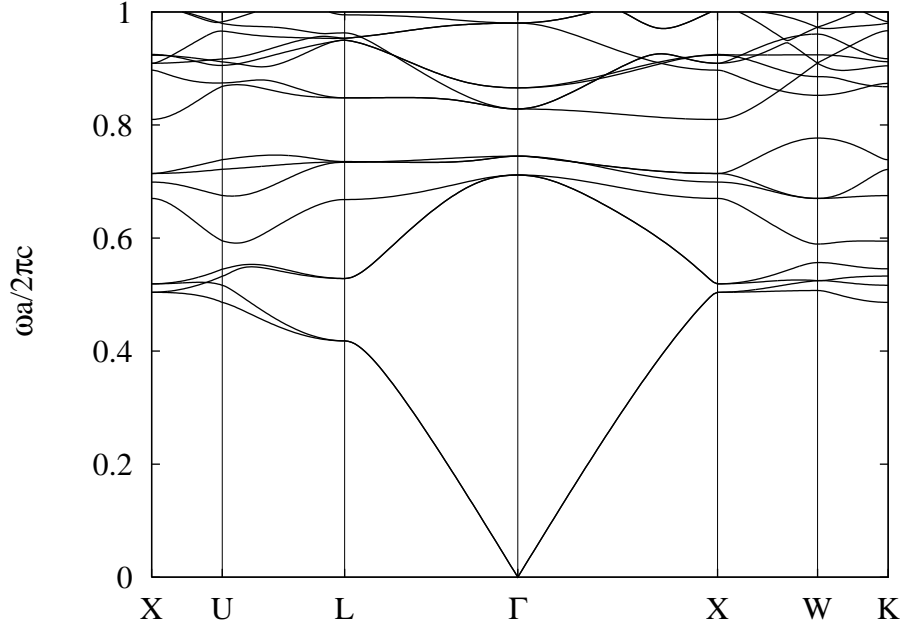
13

Figure 1.6: Band structure of a inverse opal with air voids ($\varepsilon_{air} = 1.00$) embedded in a Silicon matrix ($\varepsilon_{Si} = 12.00$). Notice the complete band gap for energies around $0.8\omega a/(2\pi c)$.

1.3 Opal-based photonic crystals: what has been done?

The discovery that the structure of natural precious opals consists of periodically packed silica spheres goes back to the beginning of 1960s, from the papers of J. V. Sanders and co-workers [82, 83]. Afterwards, synthetic opals for jewelry were developed since 1970s by Pierre Gilson and few others.

As mentioned before, colloidal crystals offer now an excellent means in controlling electromagnetic wave propagation because their fabrication is comparatively straightforward and basically inexpensive. Ref. [84] is the first work that presents artificial opals as 3D PhCs for visible light, showing that their band structure can be determined by transmission and reflection measurements. Besides it is proven that their system of interconnected pores can be infiltrated with semiconductor nanocrystals in order to study the dependence of the PBGs on the refractive index contrast [84, 73]. From then on the optical properties of opals have been intensively studied from an experimental point of view, besides a large improvement in fabrication techniques.

The photonic band structure of direct and inverse opals is well known from a variety of methods [22, 85, 86], the simplest one being 3D plane-wave expansion [87, 38, 46], examined in Chapt. 2. The difficulty in studying these systems lies in developing a good theoretical approach to model their optical properties, such as reflectance, transmittance and diffraction, in the high energy regime,

14

where the wavelength of electromagnetic waves involved is of the same order as the microsphere size and, consequently, as lattice constants. Many approaches have been used to give a theoretical analysis of optical spectra and they have been proved to give quite good results in the region of lower energy, before the onset of diffraction. In the following we will name some of them.

First, a scalar-wave approximation [88, 89, 90, 28] is frequently employed for a quick analysis of experimental results in the region of the first-order stop band, even when defects are included [79]. In this approach, the electric field in the medium is treated as a scalar rather than a vector quantity. Then it is assumed that the conditions of the experiment strongly favor scattering off of one particular set of lattice planes, and that the effects of all other lattice planes may be neglected: this is justified by the fact that the Fourier coefficient of the dielectric function expansion decreases with increasing reciprocal lattice vectors $\mathbf{G}$, i.e. only the shortest reciprocal lattice vectors contribute significantly. This approximation is clearly unsuitable to study the effects due to higher-order diffraction, dominant in the region of the second order stop band and above.

The finite-difference time domain (FDTD) method is widely used to study electrodynamic problems. Maxwell's equations (in partial differential form) are modified to central-difference equations, discretized, and implemented in software. The equations are solved in a leapfrog manner: the electric field is solved at a given instant in time, then the magnetic field is solved at the next instant in time, and the process is repeated over and over again [91]. Neglecting numerical approximation essentially due to time and space grids, the code gives exact solutions of Maxwell equation in a variety of systems, with either finite or infinite size. Finite structures are usually surrounded by Perfectly Matched Layers, i.e. a numerical material which has the property of absorbing any incoming field and hence simulate an infinite open region. Periodic and/or symmetric boundary conditions can also be implemented. This approach has been applied to study light propagation in 3D PhCs [92], however it requires heavy numerical calculations, especially for thick samples. Moreover it reproduces the optical spectra, but it gives little help in understanding the physics underneath the experiment.

Third, the transfer matrix method [93] has been used in order to study the optical properties of opals in the surroundings of the first pseudo-gap [94, 95, 96]. This approach is well known from solid state physics [39, 40], where it is usually applied to super-lattices. The transfer matrix relates the coefficients of plane waves on the left side of a dielectric layer to the waves on the right side. The method relies on a discretization of Maxwell equations and on the multiple scattering formula. It presents some difficulties when dealing with thick samples, because of numerical overflows. On the other hand, the scattering matrix method, illustrated in Chapter 2 of this thesis, has the great advantage of relating the incoming waves with the out-coming ones, thereby avoiding overflows.

Fourth, the vectorial Korringa-Kohn-Rostoker (KKR) method is an accu-

rate one for treating spherical particles in colloidal solutions [97, 98, 99, 100]. The method relies on a subdivision of the 3D structure in 2D layers of spheres and it proved to be hard to apply to close-packed opals, in which two consecutive layers along the (111) direction partially overlap. Very recently this method has given good results studying the optical response of opals introducing extinction in dielectric function of spheres to take account of intrinsic defects that determine the shape of experimental spectra [101].

The first works on optical characterization of artificial opals were concerned with the fundamental stop band (or Bragg peak) and its evolution as a function of incidence angle, with multiple peaks related to diffraction appearing at high angles [102, 30, 31, 96, 103, 104, 105]. The reason for that resides in the fact that for higher energies the optical properties depend strongly on the quality of the sample, because the wavelengths involved are of the order of lattice constant. Hence, even a small amount of disorder can return in large broadening of the peaks and a precise measurement of optical properties can became impossible. Recently, studies on high-quality opals with large single domains allowed a precise determination of optical spectra in the region around and above the second-order stop band [68, 106, 107], where diffraction effects due to higher-order crystalline planes come into play even at normal incidence.

Finally we want to name a few of the interesting issues that can be studied in opal structures. One of them is the "super-prism phenomenon", where the light path shows a drastic wide swing with a slight change of the incident light angle owing to the strong modification of group velocity. Such feature can be explained by means of equifrequency surfaces (EFS) of photonic band structure [108]. For light travelling in a homogeneous material of index n its EFS is a sphere described by the relation $\omega = ck/n$, otherwise in PhCs EFS are determined by the photonic band dispersion. When low dispersion bands, associated to multiple diffraction, are present, the EFSs assume complicated shapes, commonly defined as "monster": the group velocity, that is the gradient of the frequency $\nabla_{\mathbf{k}}\omega$ with respect to the wavevector and it is thus always perpendicular to these surfaces, can assume very different values even for close light wavelengths and yields to the "super-prism" effect. This effect has been shown by Kosaka *et al.* [109] in a 3D PhC made of alternate layers of amorphous Si and SiO_2 on a patterned Si substrate having a hexagonal array of holes that resemble graphite structure. Ochiai and Sánchez-Dehesa theoretically investigated the effect in opals [24]. The light propagation angle inside the opals is determined by the group velocity vector of the bulk eigenmodes having the strongest coupling with the incident light at the boundary of the opal. It is found that the super-prism effect takes place quite generally in the frequency range where many flat bands exist owing to the zone folding.

Another appealing phenomenon is superluminality. The implications on the violation of causality principle have attracted much attention from scientific

world and the effect has been investigated in many media [110, 111, 112]. Besides this, also slow light has been a hot topic in the last few years [113, 114, 115]. A superluminal behaviour has been proved, both theoretically and experimentally, to exist in the first stop band of opals band structure: the phenomenon is strictly related to the extinction occurring inside the pseudo gap, in agreement with causality principle. This is accompanied by a very low group velocity at the two band edges near the gap, where bands become flat [25, 26, 27, 28, 29]. In Chapter 5, instead, we show a shift from slow to superluminal and even negative group velocity in the second-order stop band region: in this case the effect is related to higher order diffraction.

Many of the phenomena that can be observed in the high energy region in bare opals are someway related to higher order diffraction and, in particular, to the flat bands near the second order stop band [27, 30, 31, 32, 33]. In Chapter 5 we will name a few of them that can be examined with the theoretical model developed in this thesis.

Finally, inverse opals are really a good system to investigate the inhibition of spontaneous emission, basically because the high dielectric contrast induces a strong modification in density of states [116]. In the works of Schriemer *et al.* [34] and Koenderink *et al.* [35] spontaneous-emission spectra from laser dye in PhCs made of inverse opals in Titania are presented. The latter demonstrates the inhibition of emission up to a factor ~ 5 over a large bandwidth of 13% of the first order Bragg resonance frequency and experimental measurement are supported by calculation of total density of states. Modification in spontaneous emission have also been studied in bare opals [36, 37].

Chapter 2

A theoretical approach to band structure and optical properties of opals

This chapter introduces the theoretical approach exploited in this work to study the optical properties of opal-based photonic crystals (PhCs). The first section is devoted to the description of the crystallographic structure of opals. Subsequently an overview of both plane-wave expansion and scattering matrix methods is given. These techniques are used to derive the photonic band structure and the optical properties such as reflectance and transmittance. Finally, the staircase approximation introduced for scattering matrix calculations is presented.

2.1   The opal structure

A direct opal is a crystal made of dielectric spheres in air, which are arranged in a face centered cubic (fcc) lattice. Usually (111) planes are parallel to the substrate on which the sample is grown, hence the opal structure can be viewed as a stacking of layers in a close-packed arrangement: each layer perpendicular to the [111] direction is a triangular lattice with periodicity equal to sphere diameter $d = a/\sqrt{2}$, where a is the fcc lattice constant, and it is shifted with respect to the previous one following a sequence of ABC, ABC. . . The situation is depicted in Fig. 2.1(a), which shows a top view of three consecutive (111) planes. Here, it is clear that each of them is shifted along the y-direction by a quantity equal to $d/\sqrt{3}$ with respect to the previous one. The equivalence between this lattice and the fcc one (Fig. 2.1(b)), as usually shown in text book, is not easily figured out. In Fig. 2.1(b) the [100] direction is taken as the vertical one and the orientation of (111) planes, i.e. cube diagonal, is identified by the same color of the spheres. Now it is easy to recognize that the fcc lattice can be viewed as a stacking sequence of triangular layers, bearing in mind that
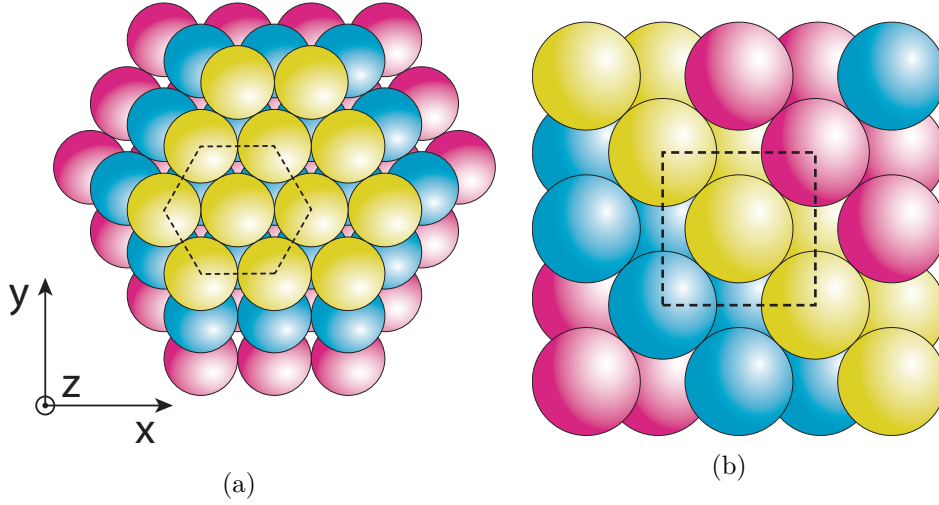
19

Figure 2.1: Sketches of a close-packed fcc lattice as viewed from two different crystallographic directions: (a) [111] direction (hexagonal face in dashed black line) and (b) [100] direction (square centered face in dashed black line). In (a) the reference frame used in the text is shown. Notice that the same colors (yellow, cyan and magenta) identifies the same lattice planes in both the two drawings.

the period along the vertical direction is made of three layers instead of two, as in the close-packed hexagonal lattice. More details about these two Bravais lattices can be found in Appendix A.

For sake of clarity it is better to fix a reference frame that will be used hereafter. Since the opal growth is usually oriented along the [111] crystallographic direction this will be taken as the vertical direction. Therefore, x and y direction will be those shown in Fig. 2.1(a).

A vertical cross section of the opal structure in the yz plane is shown in Fig. 2.2(a). It can be seen that two consecutive layers are interpenetrating, i.e. the distance between the two is smaller than the sphere diameter. In particular, the distance d_{111} between two planes of spheres along the [111] direction is given by

$$d_{111} = \sqrt{\frac{2}{3}}\, d = \frac{a}{\sqrt{3}}, \tag{2.1}$$

where, as before, d is the sphere diameter and a the fcc lattice constant. A detailed description of the region where the planes are interpenetrating, highlighted in Fig. 2.2(a) by two dot-dashed lines, is really important. In Section 2.4 we will see that modelling this region is essential in order to reproduce diffraction effects. A starting point in giving a picture of the interpenetration can be the calculation of the characteristic length of this region: the height H_{cap} of the sphere caps and their radius R_{cap} at the contact point. We obtained the
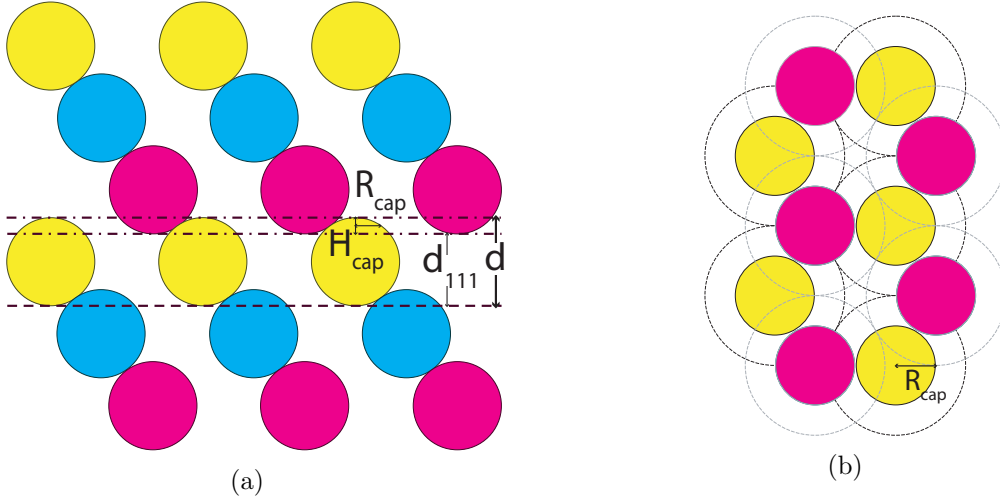
20

Figure 2.2: (a) Cross-sectional view of an fcc-lattice oriented along [111] direction. Similar colors refers to the same lattice planes shown in Fig. 2.1(a). The region where two consecutive planes are interpenetrating is defined by two dashed-dotted lines. The quantities R_{cap} and H_{cap} are also defined. (b) Cross section at the contact point between spheres belonging to different planes. In dotted line sphere diameters of two consecutive layers are presented.

following values:

$$
H_{cap} = \left(1 - \sqrt{\frac{2}{3}} \right) d \,, \quad R_{cap} = \frac{d}{2\sqrt{3}} \,. \tag{2.2}
$$

Figure 2.2(b) shows the particular arrangement of sphere caps in the plane where contact points lie, i.e. halfway between the two dash-dotted line in Fig. 2.2(a). This is the so-called graphite lattice, i.e. a triangular lattice with a basis of two atoms per unit cell [39, 40].

The geometrical description presented in this section is essential in order to understand the structure we have to model, especially when we need to slice the spheres to exploit the scattering matrix formalism.

2.2 The plane-wave expansion

The plane-wave expansion [38, 46, 87] is the natural way to implement the master equation (1.7a). Firstly, the periodic dielectric function $\varepsilon(\mathbf{r})$ can be expanded in a Fourier series involving plane waves. Moreover, as seen in Sect. 1.1, the Bloch theorem states that the electric and magnetic fields can be expressed as a plane wave modulated by a function with the same periodicity as the lattice, which can also be expanded in plane waves.

The method can be applied both to two and three dimensional PhCs. In the following we will analyse the latter example, since it is the case of the

opal arrangement. Due to its nature, the method allows to obtain photonic band dispersion and field profile of an infinite PhCs. Finite size effects and/or defects states can be studied by means of super-cell, as will be explained in Chapt. 4. The convergence of the method can be quite convenient, especially if the index contrast of the structure is not too high.

We recall here for convenience the master equation for the magnetic field **H** (1.7a):

$$\nabla \times [\eta(\mathbf{r})\nabla \times \mathbf{H}(\mathbf{r})] = \frac{\omega^2}{c^2}\mathbf{H}(\mathbf{r}), \tag{2.3}$$

$\eta(\mathbf{r})$ being the inverse of the dielectric function. This change will turn useful in the following, as the way η is calculated is crucial for the method's convergence.

Now the **H** field is rewritten in the way suggested by the Bloch-Floquet theorem:

$$\mathbf{H}(\mathbf{r}) = \sum_{\mathbf{G}} \mathbf{H}(\mathbf{k} + \mathbf{G})e^{i(\mathbf{k}+\mathbf{G})\cdot\mathbf{r}}. \tag{2.4}$$

Maxwell equations impose the magnetic field **H** to be transverse with respect to the propagation direction. This means that one can project every vector **H(G)** of the Fourier expansion on two orthogonal versors $\hat{\mathbf{e}}_{1,\mathbf{k}+\mathbf{G}}$ and $\hat{\mathbf{e}}_{2,\mathbf{k}+\mathbf{G}}$ chosen in such a way to constitute an orthonormal tern with the vector $\mathbf{k}+\mathbf{G}$. The magnetic field can now be expressed as follows:

$$\mathbf{H}(\mathbf{r}) = \sum_{\mathbf{G}'} \left(h_{1,\mathbf{k}+\mathbf{G}'}\hat{\mathbf{e}}_{1,\mathbf{k}+\mathbf{G}'} + h_{2,\mathbf{k}+\mathbf{G}'}\hat{\mathbf{e}}_{2,\mathbf{k}+\mathbf{G}'} \right) e^{i(\mathbf{k}+\mathbf{G}')\cdot\mathbf{r}}, \tag{2.5}$$

where $h_{1,\mathbf{k}+\mathbf{G}}$ and $h_{2,\mathbf{k}+\mathbf{G}}$ are the components of **H(G)** projected on the two versors previously defined.

The periodicity of the dielectric function and, consequently, of its inverse $\eta(\mathbf{r})$ allows us to write:

$$\eta(\mathbf{r}) = \sum_{\mathbf{G}} \hat{\eta}(\mathbf{G})e^{i\mathbf{G}\cdot\mathbf{r}}. \tag{2.6}$$

The two previous expressions, (2.5) and (2.6), substituted into the master equation (2.3), lead to the following equation:

$$\sum_{\mathbf{G}} \hat{\eta}(\mathbf{G} - \mathbf{G}')|\mathbf{k} + \mathbf{G}'||\mathbf{k} + \mathbf{G}|$$

$$\begin{bmatrix} \hat{\mathbf{e}}_{2,\mathbf{k}+\mathbf{G}} \cdot \hat{\mathbf{e}}'_{2,\mathbf{k}+\mathbf{G}'} & -\hat{\mathbf{e}}_{2,\mathbf{k}+\mathbf{G}} \cdot \hat{\mathbf{e}}'_{1,\mathbf{k}+\mathbf{G}'} \\ -\hat{\mathbf{e}}_{1,\mathbf{k}+\mathbf{G}} \cdot \hat{\mathbf{e}}'_{2,\mathbf{k}+\mathbf{G}'} & \hat{\mathbf{e}}_{1,\mathbf{k}+\mathbf{G}} \cdot \hat{\mathbf{e}}'_{1,\mathbf{k}+\mathbf{G}'} \end{bmatrix} \begin{bmatrix} h_{1,\mathbf{k}+\mathbf{G}'} \\ h_{2,\mathbf{k}+\mathbf{G}'} \end{bmatrix} = \frac{\omega^2}{c^2} \begin{bmatrix} h_{1,\mathbf{k}+\mathbf{G}} \\ h_{2,\mathbf{k}+\mathbf{G}} \end{bmatrix}, \tag{2.7}$$

where $\mathbf{G} = \mathbf{G}' - \mathbf{G}''$. This is an eigenvalue equation that can be solved with standard routines for matrix diagonalization.

The dimension of the matrices involved depends on the number of reciprocal lattice vectors at which the field and dielectric function expansion are truncated. If we take a number N of vectors **G**, linear combination of reciprocal lattice vectors, the problem dimensions become $2N \times 2N$. Moreover, reciprocal lattice vector truncation gives rise to unavoidable numerical error.
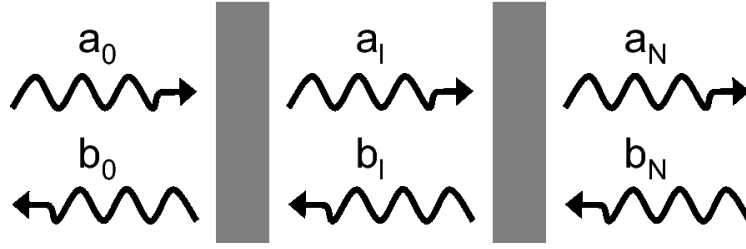
Figure 2.3: Schematic diagram for forward and backward propagating waves in different layers of the structure. $l = 0$ label the surface, $l = N$ the substrate of the multilayer.

In our code the number of plane waves is usually chosen accordingly to the symmetry of the lattice, i.e. taking into account a closed shell of n-order neighbours in reciprocal lattice, represented by vectors with the same length: this gives a reasonably small error close to the Γ point, where symmetry conditions are fully respected.

The convergence of the method depends strongly on the way the inverse of the dielectric function $\eta(\mathbf{r})$ is calculated. In our code we follow the one developed by Ho *et al.* [87] that guarantees a faster convergence. It consists in calculating the Fourier transform of the dielectric function $\varepsilon(\mathbf{r})$ and then obtain his inverse $\eta(\mathbf{r})$ imposing the condition that

$$\eta(\mathbf{G}'' - \mathbf{G}) = \varepsilon^{-1}(\mathbf{G}'' - \mathbf{G}) \,. \tag{2.8}$$

If the number of reciprocal lattice vectors taken into account was infinite, then it would be equivalent to calculate $\eta(\mathbf{r})$ as $\varepsilon^{-1}(\mathbf{r})$ and then derive its Fourier transform. This is no more true when a truncation on the number of plane-waves is needed and in this case the numerical procedure embodied in Eq. (2.8) yields better convergence properties.

The Fourier transforms of the dielectric function $\varepsilon(\mathbf{r})$ are obtained analytically and then implemented in the code. In Appendix B the basic calculations to obtain the Fourier transform of the dielectric function of the main lattices used in this thesis are reported.

2.3 The scattering matrix method

In this section we would like to report the basic concepts of the scattering matrix formalism and, in particular, of the Fourier modal expansion as it has been developed by Whittaker and Culshaw [117]. This particular formulation allows to deal with multilayered structures with an in-plane patterning, hence it is suitable to study the optical properties of opals, even if some approximations are needed. It is worth mentioning that there are other formulations of the scattering matrix method, developed in Refs. [118] and [119].

The scattering matrix method is well known in solid state physics when dealing with multilayered structures such as superlattices, quantum wells, etc.

The formalism is somehow similar to the transfer matrix one [40] as it is based on a matrix built layer by layer which relates forward and backward states on the two sides of a system, but it has the advantage of overcoming the possible overflow problems occurring with exponentially growing components. Both formalisms can be applied to optical systems, where the incoming and outgoing states are represented by the electromagnetic waves.

For a finite N-layer structure, as the one shown in Fig. 2.3, we call $\mathbf{a}_l$ and $\mathbf{b}_l$ the coefficients of the "forward" and "backward" states, respectively, with the former ones defined as those which propagate or exponentially decay in the positive-z direction, from left to right in the figure, and the latter as those which propagate or exponentially decay in the negative-z direction. Labelling $l = 0$ the semi-infinite medium at the left side of the structure and $l = N$ the one at the right side, the scattering matrix $\mathbf{S}(0, N)$ relates the coefficients of outgoing states, namely a_N and b_0, with those of incoming states, a_0 and b_N:

$$\left(\begin{array}{c} \mathbf{a}_N \\ \mathbf{b}_0 \end{array} \right) = \mathbf{S}(0, N) \left(\begin{array}{c} \mathbf{a}_0 \\ \mathbf{b}_N \end{array} \right) . \tag{2.9}$$

To figure out the main difference between the two matrix methods, we report the definition of the transfer matrix:

$$\left(\begin{array}{c} \mathbf{a}_0 \\ \mathbf{b}_0 \end{array} \right) = \mathbf{T}(0, N) \left(\begin{array}{c} \mathbf{a}_N \\ \mathbf{b}_N \end{array} \right) . \tag{2.10}$$

It can be observed that this matrix relates the coefficients of the forward and the backward states on one side of the systems to those at the opposite side. When evanescent states are present this formalism can result in an exponential increase of the transfer matrix elements, that is difficult to treat in numerical calculation, resulting in overflow errors.

As in the transfer matrix scheme, one has to build the scattering matrix of the total system layer by layer. For the subsystem between the lth and the l'th layer, we define:

$$\left(\begin{array}{c} \mathbf{a}_l \\ \mathbf{b}_{l'} \end{array} \right) = \mathbf{S}(l', l) \left(\begin{array}{c} \mathbf{a}_{l'} \\ \mathbf{b}_l \end{array} \right) = \left(\begin{array}{cc} \mathbf{S}_{11} & \mathbf{S}_{12} \\ \mathbf{S}_{21} & \mathbf{S}_{22} \end{array} \right) \left(\begin{array}{c} \mathbf{a}_{l'} \\ \mathbf{b}_l \end{array} \right) . \tag{2.11}$$

The boundary conditions, that require continuity of the in-plane components of electric and magnetic field E_x, E_y, H_x and H_y can be expressed in a matrix relationship to give:

$$\left(\begin{array}{c} \mathbf{a}_l \\ \mathbf{b}_l \end{array} \right) = \mathbf{I}(l + 1) \left(\begin{array}{c} \mathbf{a}_{l+1} \\ \mathbf{b}_{l+1} \end{array} \right) = \left(\begin{array}{cc} \mathbf{I}_{11} & \mathbf{I}_{12} \\ \mathbf{I}_{21} & \mathbf{I}_{22} \end{array} \right) \left(\begin{array}{c} \mathbf{a}_{l+1} \\ \mathbf{b}_{l+1} \end{array} \right) , \tag{2.12}$$

where $\mathbf{I}(l + 1)$ is the interface matrix representing the coupling at the $(l + 1)$ interface.

The expressions of the fields in each layer of the structure are needed in order to define the interface matrix. The procedure developed by Whittaker

and Culshaw [117], that we will analyse in the following, gives us the possibility to treat a patterned multilayer, i.e. a structure where each layer is characterized by a dielectric function $\varepsilon(\mathbf{r})$ which is periodic in the plane perpendicular to the stacking.

Exploiting this periodicity, the magnetic and electric fields can be expanded as a sum over reciprocal lattice vectors $\mathbf{G}$ for a given two-dimensional Bloch wavevector $\mathbf{k}$:

$$\mathbf{H}(\mathbf{r}, z) = \sum_{\mathbf{G}} \tilde{\mathbf{H}}(\mathbf{G}, z) e^{i(\mathbf{k}+\mathbf{G})\cdot\mathbf{r}} \,, \tag{2.13a}$$

$$\mathbf{E}(\mathbf{r}, z) = \sum_{\mathbf{G}} \tilde{\mathbf{E}}(\mathbf{G}, z) e^{i(\mathbf{k}+\mathbf{G})\cdot\mathbf{r}} \,. \tag{2.13b}$$

Due to the same reasons, the dielectric function of each layer can be Fourier transformed as follows:

$$\tilde{\varepsilon}(\mathbf{G}) = \frac{1}{\Omega} \int_{\Omega} d\mathbf{r}\, \varepsilon(\mathbf{r}) e^{-i\mathbf{G}\cdot\mathbf{r}} \,, \tag{2.14}$$

where Ω is the area of the in-plane unit cell. It is useful to define a matrix $\hat{\varepsilon}$, such that each element $\hat{\varepsilon}_{GG'} = \tilde{\varepsilon}(\mathbf{G} - \mathbf{G}')$. Also the inverse of the dielectric function $\eta(\mathbf{r}) = \varepsilon^{-1}(\mathbf{r})$ can be expressed as a Fourier expansion $\tilde{\eta}(\mathbf{G})$ and a similar matrix representation $\hat{\eta}$ can be defined.

At this point it is worth stressing the two main conditions that are needed in order to study the optical properties by means of this formalism. First of all the same reciprocal lattice vectors must be defined in all the layers of the structure; this means that the lattice must be the same except for the basis vectors and/or a shift between one layer and another, since this would not result in a change of reciprocal lattice. Second, layers must be homogeneous along the z direction, since it is supposed that the dielectric function is periodic only in the xy plane. While the former condition is automatically satisfied in opal PhCs, an approximation is needed to treat the sphere, as they are obviously non-homogeneous along the vertical direction.

Now the field expansion (2.13) must be introduced in Maxwell equations. According to Ref. [117], we assume a harmonic time dependence for the fields, we rescale them such that $\omega\varepsilon_0\mathbf{E} \to \mathbf{E}$ and $\omega/c \to \omega$, and we write the two Maxwell curl equations as follows:

$$\nabla \times \mathbf{H} = -i\varepsilon\mathbf{E} \,, \tag{2.15}$$

$$\nabla \times \mathbf{E} = -i\omega^2\mathbf{H} \,. \tag{2.16}$$

Using the Fourier vector notation of Eqs. (2.13) and (2.14), the three components of equation (2.15) can be expressed as:

$$i\hat{k}_y h_z(z) - h'_y = -i\hat{\varepsilon}e_x(z) \,, \tag{2.17a}$$

$$h'_x(z) - i\hat{k}_x h_z = -i\hat{\varepsilon}e_y(z) \,, \tag{2.17b}$$

$$i\hat{k}_x h_y(z) - i\hat{k}_y h_z(z) = -i\hat{\varepsilon}e_z(z) \,, \tag{2.17c}$$

where $\mathbf{h}(z) = [\tilde{\mathbf{H}}(\mathbf{G}_1, z), \tilde{\mathbf{H}}(\mathbf{G}_2, z), \ldots]$. A similar expression holds also for $\hat{\mathbf{e}}(z)$:

$$i\hat{k}_y e_z(z) - e'_y = -i\omega^2 h_x(z)\,, \tag{2.18a}$$

$$e'_x(z) - i\hat{k}_x e_z = -i\omega^2 h_y(z)\,, \tag{2.18b}$$

$$i\hat{k}_x e_y(z) - i\hat{k}_y e_z(z) = -i\omega^2 h_z(z)\,. \tag{2.18c}$$

$\hat{k}_x$ and $\hat{k}_y$ are diagonal matrices with $(\hat{k}_i)_{\mathbf{GG}} = (k_i + G_i)$ $(i = x, y)$ and the primes denotes differentiation with respect to z.

To solve the equation system in each single layer, the $\mathbf{H}$ field is expanded in basis states with zero divergence:

$$\mathbf{H}(\mathbf{r}, z) = \sum_{\mathbf{G}} \left(\phi_x(\mathbf{G}) \left[\hat{\mathbf{x}} - \frac{1}{q}(k_x + G_x)\hat{\mathbf{z}} \right] \right. \\ \left. + \phi_y(\mathbf{G}) \left[\hat{\mathbf{y}} - \frac{1}{q}(k_y + G_y)\hat{\mathbf{z}} \right] \right) e^{i(\mathbf{k}+\mathbf{G})\cdot(\mathbf{r})+iqz}\,, \tag{2.19}$$

where $\hat{\mathbf{x}}$, $\hat{\mathbf{y}}$ and $\hat{\mathbf{z}}$ are the conventional unit vectors and $\phi_x(\mathbf{G})$, $\phi_y(\mathbf{G})$ are expansion coefficients. A shift of the lattice origin that may occur between two different layers will result in a phase factor that multiplies the field expansion:

$$\mathbf{H}(\mathbf{r} + \mathbf{r}', z) = \sum_{\mathbf{G}} \tilde{\mathbf{H}}(\mathbf{G}, z) e^{i(\mathbf{k}+\mathbf{G})\cdot\mathbf{r}'} e^{i(\mathbf{k}+\mathbf{G})\cdot\mathbf{r}}\,. \tag{2.20}$$

Practically speaking, the fields inside the layer are exactly the same, apart from a translation of the reference frame, but the phase factor has to be multiplied by the coefficients $\phi(\mathbf{G})$ of the expansion when the interface matrix is built up. A change in the basis vectors of the lattice will result simply in a change of the dielectric function $\varepsilon(\mathbf{r})$ and in its Fourier transform $\tilde{\varepsilon}(\mathbf{G})$ in a given layer.

Defining the two vectors $\phi_i = [\phi_i(\mathbf{G}_1), \phi_i(\mathbf{G}_2), \ldots]^T$, where the subscript i refers to x and y, we can translate Eq. (2.19) in the momentum representation

$$\mathbf{h}(z) = e^{iqz} \left\{ \phi_x \hat{\mathbf{x}} + \phi_y \hat{\mathbf{y}} - \frac{1}{q}(\hat{k}_x \phi_x + \hat{k}_y \phi_y \hat{\mathbf{z}}) \right\}\,. \tag{2.21}$$

Using Maxwell equations defined in (2.17), we can write an analogous equation for $\hat{\mathbf{e}}(z)$

$$\hat{\mathbf{e}}(z) = \frac{1}{q} e^{iqz} \hat{\eta} \left\{ [\hat{k}_y \hat{k}_x \phi_x + (q^2 + \hat{k}_y \hat{k}_y)\phi_y]\hat{\mathbf{x}} \right. \\ \left. - [\hat{k}_x \hat{k}_y \phi_y + (q^2 + \hat{k}_x \hat{k}_x)\phi_y]\hat{\mathbf{y}} + q[\hat{k}_y \phi_x - \hat{k}_x \phi_y]\hat{\mathbf{z}} \right\}\,. \tag{2.22}$$

From the second set of Maxwell equations, namely Eq. (1.1), three identities are obtained, the third of them being linearly dependent from the first two. Writing the two linearly independent ones in a matrix notation the following equation is given:

26

$$\left\{ \begin{pmatrix} \hat{\eta} & 0 \\ 0 & \hat{\eta} \end{pmatrix} \left[q^2 + \begin{pmatrix} \hat{k}_x\hat{k}_x & \hat{k}_x\hat{k}_y \\ \hat{k}_y\hat{k}_x & \hat{k}_y\hat{k}_y \end{pmatrix} \right] + \begin{pmatrix} \hat{k}_y\hat{\eta}\hat{k}_y & -\hat{k}_y\hat{\eta}\hat{k}_x \\ \hat{k}_x\hat{\eta}\hat{k}_y & -\hat{k}_x\hat{\eta}\hat{k}_x \end{pmatrix} \right\}$$

$$\times \begin{pmatrix} \phi_x \\ \phi_y \end{pmatrix} = \omega^2 \begin{pmatrix} \phi_x \\ \phi_y \end{pmatrix}. \quad (2.23)$$

This is an eigenvalue equation for ω, that can be rewritten in a more compact form, naming as $\mathcal{H}$, K and $\mathcal{K}$ the three 2×2 matrices appearing in the equation:

$$\left[\mathcal{H}(q^2 + K) + \mathcal{K} \right] \phi = \omega^2 \phi. \quad (2.24)$$

Multiplying the latter by the matrix $\mathcal{E}$, i.e. the inverse of $\mathcal{H}$ with block diagonals $\hat{\varepsilon}$, an eigenvalue equation for q is obtained:

$$\left[\mathcal{E}(\omega^2 - \mathcal{K}) - K \right] \phi = q^2 \phi. \quad (2.25)$$

This is an asymmetric matrix eigenvalue problem, but a symmetric one can be found by multiplying by $\omega^2 - \mathcal{K}$ and exploiting the fact that $\mathcal{K}K = 0$:

$$\left[(\omega^2 - \mathcal{K})\mathcal{E}(\omega^2 - \mathcal{K}) - \omega^2 K \right] \phi = q^2(\omega^2 - \mathcal{K})\phi. \quad (2.26)$$

By solving this equation we obtain a set of eigenvalues q_n and eigenvectors ϕ_n that can be used as basis states to expand the field in each layer of the structure. The orthogonality relation for these eigenvectors is given by:

$$\phi_n^T(\omega^2 - \mathcal{K})\phi_{n'} = \delta_{nn'}. \quad (2.27)$$

The next step towards the scattering matrix formalism is to expand the fields into the basis set obtained a few lines earlier, from Eqs. (2.26) and (2.27), and to express them as a combination of forward and backward propagating waves with wave numbers q_n, and complex amplitudes a_n and b_n. Then, boundary conditions at the interfaces give rise to the interface matrix and, subsequently, to the scattering matrix of the whole system.

From Eq. (2.21) we can write

$$\begin{pmatrix} h_x(z) \\ h_y(z) \end{pmatrix} = \sum_n \begin{pmatrix} \phi_{x_n} \\ \phi_{y_n} \end{pmatrix} \left(e^{iq_n z} a_n + e^{iq_n(d-z)} b_n \right), \quad (2.28)$$

where d is the thickness of the layer. Notice that a_n is the coefficient of the forward wave at $z = 0$, i.e. at the left end, and b_n of the backward going wave at $z = d$, i.e. at the right end. Similarly, for the electric field component we can write:

$$\begin{pmatrix} -e_y(z) \\ e_x(z) \end{pmatrix} = \sum_n t \begin{pmatrix} \hat{\eta} & 0 \\ 0 & \hat{\eta} \end{pmatrix} \left[q_n^2 + \begin{pmatrix} \hat{k}_x\hat{k}_x & \hat{k}_x\hat{k}_y \\ \hat{k}_y\hat{k}_x & \hat{k}_y\hat{k}_y \end{pmatrix} \right] \quad (2.29)$$

$$\times \begin{pmatrix} \phi_{x_n} \\ \phi_{y_n} \end{pmatrix} \frac{1}{q_n} \left(e^{iq_n z} a_n + e^{iq_n(d-z)} b_n \right). \quad (2.30)$$

Finally, combining these two equation we get:

$$\begin{pmatrix} e_\parallel(z) \\ h_\parallel(z) \end{pmatrix} = \begin{pmatrix} (\omega^2 - \parallel)\Phi\hat{q}^{-1} & -(\omega^2 - \parallel)\Phi\hat{q}^{-1} \\ \Phi & \Phi \end{pmatrix} \begin{pmatrix} \hat{f}(z)a \\ \hat{f}(d-z)b \end{pmatrix}, \qquad (2.31)$$

where Φ is a matrix whose columns are the vectors ϕ_n, and $\hat{q}$ and $\hat{f}$ are diagonal matrices such that $\hat{q}_{nn} = q_n$ and $\hat{f}_{nn}(z) = e^{iq_n z}$, respectively.

The scattering matrix is now built starting from the matrix definition given in Eqs. (2.11) and (2.12), with a little change in interface matrix definition:

$$\begin{pmatrix} \hat{f}_l(d_l)\mathbf{a}_l \\ \mathbf{b}_l \end{pmatrix} = \mathbf{I}(l+1) \begin{pmatrix} \mathbf{a}_{l+1} \\ \hat{f}_l(d_l)\mathbf{b}_{l+1} \end{pmatrix} = \begin{pmatrix} \mathbf{I}_{11} & \mathbf{I}_{12} \\ \mathbf{I}_{21} & \mathbf{I}_{22} \end{pmatrix} \begin{pmatrix} \mathbf{a}_{l+1} \\ \hat{f}_l(d_l)\mathbf{b}_{l+1} \end{pmatrix}. \qquad (2.32)$$

Imposing continuity of the in-plane components E_x, E_y, H_x and H_y the interface matrix is derived as follows:

$$\begin{aligned} \mathbf{I}(l, l+1) =& \frac{1}{2}\hat{q}_l\Phi_l^T(\omega^2 - \mathcal{K}_{l+1})\Phi_{l+1}\hat{q}_{l+1}^{-1}\begin{pmatrix} 1 & -1 \\ -1 & 1 \end{pmatrix} \\ & \frac{1}{2}\Phi_l^T\omega^2 - \mathcal{K}_{l+1}\Phi_{l+1}\begin{pmatrix} 1 & 1 \\ 1 & 1 \end{pmatrix}. \end{aligned} \qquad (2.33)$$

In the case of a shift between two different plane this is the point in which the phase factor has to be taken into account and, specifically, it has to be multiplied to Φ_l and/or Φ_{l+1}. We mention here that this shift is needed since we are assuming the preservation of inversion symmetry in each layer of the structure under study. The following scattering matrix elements result:

$$\begin{aligned} \mathbf{S}_{11}(l', l+1) &= (\mathbf{I}_{11} - \hat{f}_l\mathbf{S}_{12}(l', l)\mathbf{I}_{21})^{-1}\hat{f}_l\mathbf{S}_{11}(l', l), \\ \mathbf{S}_{12}(l', l+1) &= (\mathbf{I}_{11} - \hat{f}_l\mathbf{S}_{12}(l', l)\mathbf{I}_{21})^{-1}(\hat{f}_l\mathbf{S}_{12}(l', l)\mathbf{I}_{22} - \mathbf{I}_{12})\hat{f}_{l+1}, \\ \mathbf{S}_{21}(l', l+1) &= \mathbf{S}_{22}(l', l)\mathbf{I}_{21}\mathbf{S}_{11}(l', l+1) + \mathbf{S}_{21}(l', l), \\ \mathbf{S}_{22}(l', l+1) &= \mathbf{S}_{22}(l', l)\mathbf{I}_{21}\mathbf{S}_{12}(l', l+1) + \mathbf{S}_{22}(l', l)\mathbf{I}_{22}\hat{f}_{l+1}, \end{aligned} \qquad (2.34)$$

starting from S(l',l')=1.

Reflectance and transmittance coefficients of the multilayered structure are obtained from the total scattering matrix $\mathbf{S}(0, N)$. If light is impinging from the left side of the medium, then a_0 is obtained by the incidence geometry and b_n is equal to zero: $b_0 = S_{21}(0, N)a_0$ represents the amplitude of the reflected beam and $a_N = S_{11}(0, N)a_0$ that of the transmitted beam.

From Eq. (2.31) the amplitude coefficients can be related to the in-plane component of the field and, thus, to the incidence angle and to the polarization of the incoming and outgoing fields. The phase delay φ_{out} of the outcoming wave can be derived by means of the following relationship:

$$\varphi_{out} = \Im(\ln\frac{a_n}{a_0}). \qquad (2.35)$$

This quantity can give information on group velocity and effective index of the structure under examination.

If the lattice period is short enough with respect to the wavelength of the incident electromagnetic field, then the transmitted and reflected amplitudes correspond to the $\mathbf{G} = 0$ components of the amplitude a_0, while the $\mathbf{G} \neq 0$ components vanish. The transmitted and reflected beams are obtained by taking the components corresponding to $\mathbf{G} = 0$ of the coefficients a_N and b_0. The situation is more complicated when diffraction occurs, i.e. when the lattice period is large enough to give rise to scattering states. In that case reflectance and transmittance amplitudes are derived from the components of a_N and b_0, corresponding to the proper $\mathbf{G}$ vector. All the other components corresponding to non evanescent waves contribute to diffraction. If all the media are lossless then $D = 1 - R - T$: this is the definition for diffraction used in the rest of the work. In a more refined treatment, diffraction channels corresponding to different $\mathbf{G}$ vectors could be explicitly separated.

2.4 Five-cylinders approximation

The scattering matrix codes gives us the possibility to calculate optical properties of a system constituted by one or more dielectric layers with the two following conditions: firstly each layer must be homogeneous along the vertical direction; secondly the reciprocal lattice vectors must be the same in each layer to exploit the Fourier modal expansion. Nevertheless this approach is very convenient as it allows distinguish zero-order Bragg reflection and transmission from higher-order processes, corresponding to diffraction in directions other than those of the transmitted and reflected beams.

A way to overcome the first of the two conditions named above is to use a staircase approach, and to subdivide each sphere in a set of cylindrical slices in xy plane. Luckily, the second of the two limitations is easily satisfied, since in each layer the spheres are arranged in a triangular lattice, even in the interpenetration region, as we have seen in Sect. 2.1.

By means of plane wave expansion code one can calculate the photonic band dispersion of an infinite crystal whether the lattice basis is made by spheres or by cylinders. Hence, a comparison between the two band structure can be used to optimize cylinder parameters or to test the validity of the approach, since it is proved that the optical properties of PhCs are strongly dependent on band dispersion. Once it is demonstrated that the approximation is good enough for our purposes, the cylinder parameters are implemented in scattering matrix code to get optical spectra, such as transmission and reflection [120]. Results obtained in this way are subsequently compared with experimental measurements.

In the following we will analyse in detail the way the cylinders parameters have been chosen. To give a true comparison between the different degrees
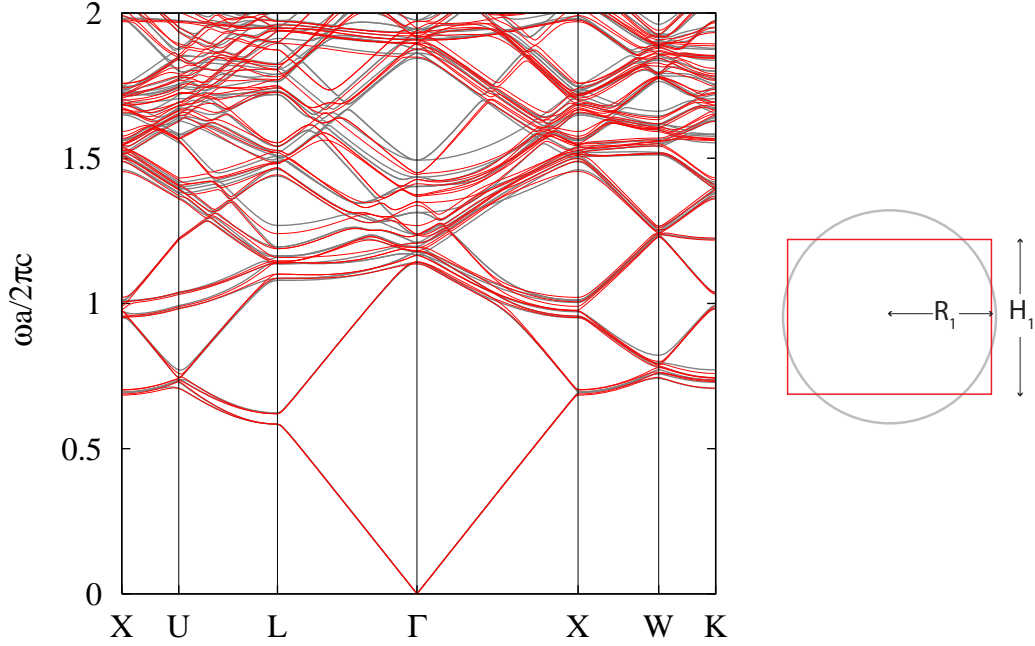
Figure 2.4: Photonic band structure of a bare opal made of polystyrene spheres in thick grey line. In thin red line the photonic band dispersion calculated with one-cylinder approximation. Besides a schematic view of the main dimensions of the cylinder used in calculation. The lengths R_1 and H_1 are proportional to the value given in Eq. (2.36).

of approximation introduced, we take as a reference sample a bare opal made of polystyrene spheres ($\varepsilon_{poly} = 2.4964$) in air ($\varepsilon_{air} = 1.00$). Thanks to scale invariance (see Sect. 1.1) the photonic band structure can be plotted in dimensionless units, so the sphere diameter does not need to be specified.

The simplest way to implement such an approach is to substitute each sphere constituting the actual structure with a single cylinder. In this way we obtained a layout that is similar to the layered dielectric structure described in Refs. [42, 121, 55]. In Fig. 2.4 results for photonic band structure are presented; in the same figure height and radius of the cylinder are also defined. In particular, the parameters used in calculations are:

$$H_1 = 0.7261d \, , \quad R_1 = 0.4791d, \tag{2.36}$$

where d is the sphere diameter. These particular values have been chosen keeping constant the volume to preserve the filling fraction of the actual structure, and varying the radius in order to fit the position of the first pseudo-gap. They are sensitive to the dielectric function and may change corresponding to the variation of dielectric contrast. As we can see from Figure 2.4, this approximation reproduces fairly well the photonic band structure near the first order stop band. Practically speaking, to reproduce the band dispersion in the low
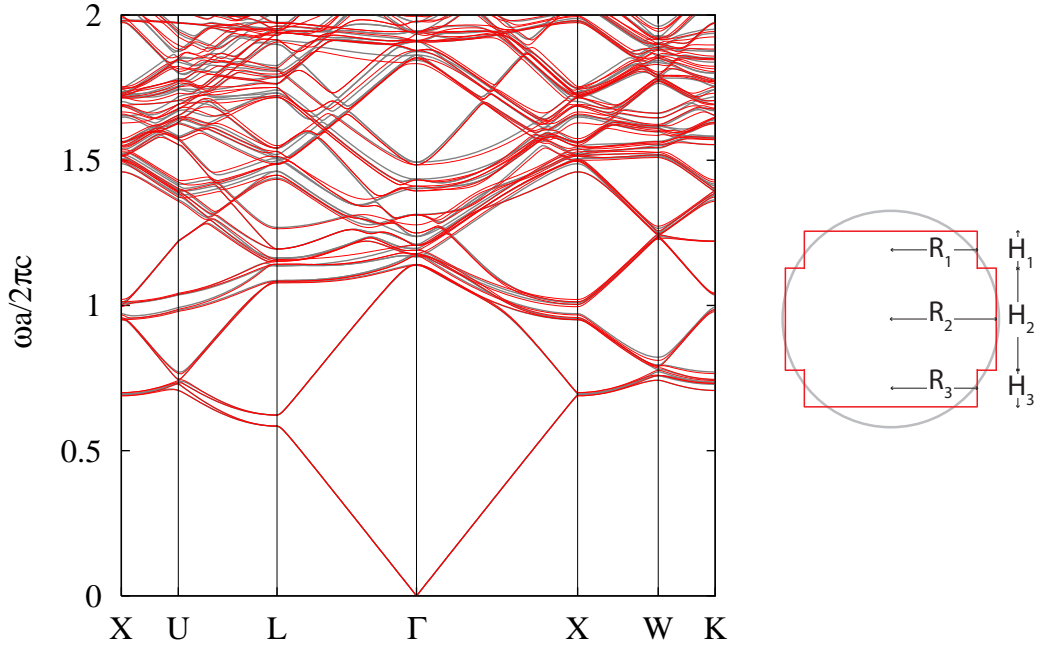
Figure 2.5: Three-cylinders approximation. In thick grey line the photonic band dispersion for the sphere layout is presented; in thin red line the dispersion obtained substituting each sphere with three cylinders. Cylinders parameters are also defined.

energy range along ΓL direction two conditions are needed. The first one is to preserve the mean effective index of the medium in order to have the same dispersion of the bands; this is fulfilled as the filling fraction is exactly the same in both the sphere and the cylinder layout, i.e. $f = \pi/(3\sqrt{2}) = 0.7405$; the second one is to introduce a proper periodicity in dielectric function to open a small gap in the L point, but this can be given also by the cylinder lattice as the wavelengths involved in the low energy region are larger than the sphere radius and they do not perceive, at least in first approximation, the change in geometry.

An interesting feature to notice is the narrow gap that splits up at the X point for the cylinders structure, while in the case of spheres the first two bands (four, if we consider also polarization) are degenerate. A reason for this can be the fact that the cylinder structure breaks the symmetry along [100] direction, as the cylinder axes are tilted with respect to this direction. Furthermore even the connection between the spheres can influence band gaps openings: as a matter of fact in this model there are no contact points between cylinders in the xy plane and, above all, the interpenetration region is absent. This two aspects must be taken into account if one wants to improve the approximation.

Given that the one-cylinder approximation works quite well in low energy region, it is worth to study the case of subdividing each sphere in a set of three cylinders in order to extend the study of optical properties in a higher

energy range. Once again cylinder parameters have been chosen in order to better reproduce the first order stop band. The superimposed conditions are the following: firstly the two outer cylinders have been chosen to be equal in order to maximize the symmetry of the object substituting the sphere; secondly the volume has been kept constant to maintain filling fraction, as in the one cylinders approach; finally the total height of the cylinders has been fixed equal to the distance d_{111}, to avoid a possible overlap between cylinders. The results are presented in Fig. 2.5 as well as the definition of the relevant dimension of cylinders. The values used in the calculation have been taken as follow:

$$
\begin{aligned}
H_1 = H_3 &= 0.1724\,d\,, \quad R_1 = R_3 = 0.3995\,d\,, \\
H_2 &= 0.4716\,d\,, \qquad\;\; R_2 = 0.4872\,d\,.
\end{aligned}
\tag{2.37}
$$

It can be seen that the radius of the inner cylinder is closer to sphere radius than the one-cylinder case, and the two outermost cylinders are smaller than the inner one. The band structure in low energy region is once again fairly well reproduced. Even at higher energies the model seems to better mimic flat bands related to diffraction. Once again, it has to be noticed that at X point a little gap, smaller than the one-cylinder case, opens up. The reason are probably the same as described in the previous paragraph. Usually optical properties of opals are probed along ΓL direction, as this is the natural growth orientation, and even at finite incidence angle the ΓX direction cannot be probed, so this feature in X point it is not particularly relevant. However the optical properties along this direction can be probed in some particular samples, as will be shown in Section 5.3, so it may become important to improve this approximation.

In the two previous examples the total height of the object substituting the sphere is at most equal to the distance d_{111}. This means that the region highlighted in Fig. 2.2(a) is not properly introduced in the optical spectra calculation. The problem is overcome if each sphere will be subdivided into five slices, whose total height is made equal to sphere diameter. The two outermost cylinders must be displaced following the graphite lattice shown in Fig. 2.2(b).

Figure 2.6 presents results for band structure obtained with this approach; in the same figure the relevant dimensions (cylinder radii and heights) are defined. Following the procedure adopted for the three-cylinders case, cylinders 1 and 5 are equal, as well as cylinders 2 and 4, to preserve symmetry with respect to the horizontal plane. The total height of the five cylinders is equal to the sphere diameter d. The outermost cylinders (no. 1 and 5) have the same height H_{cap} as the overlapping layers and the same radius R_{cap} as the sphere caps at the contact point. These cylinders are arranged in a graphite lattice shifted by $R_{\mathrm{cap}} = d/(2\sqrt{3})$ with respect to the previous layer (see Fig. 2.2(b)), while the three inner cylinders (2 to 4) are arranged according to the usual triangular lattice in their respective planes. Again, the total dielectric filling fraction is fixed to that of the spheres.
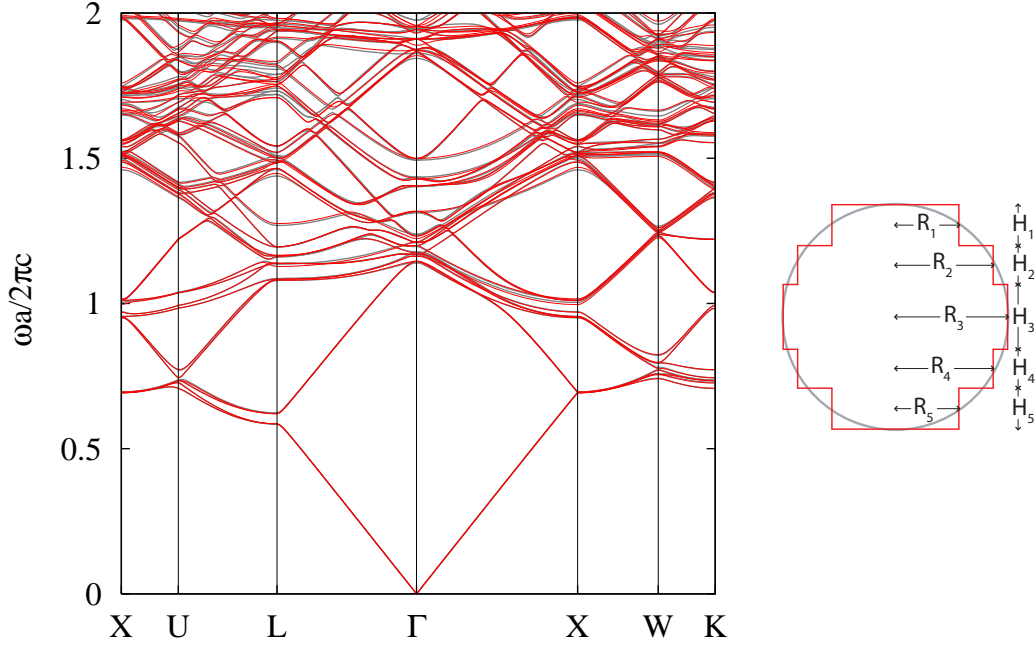
Figure 2.6: Five-cylinder approximation. In thick grey line the photonic band dispersion for the sphere layout is presented; in thin red line the dispersion obtained substituting each sphere with three cylinders. Cylinders parameters are also defined.

Once all the previous conditions are satisfied, only two degrees of freedom for cylinder parameters are left. A fine loop on these two lengths allow to optimize the approximation. The best parameters are chosen by minimizing the difference between the true energy values (i.e. the one obtained with spheres) and the approximate ones at the Γ point in a range of dimensionless frequencies up to $\omega a/(2\pi c) \leq 2$. This procedure is justified by the fact that in this particular point of the Brillouin zone the energy values are less affected by truncation of reciprocal lattice vectors in the plane-wave expansion, as pointed out in Sect. 2.2.

The best choice for the cylinder parameters is as follows:

$$
\begin{aligned}
H_1 &= H_5 = 0.1835\,d\,, & R_1 &= R_5 = 0.2886\,d\,, \\
H_2 &= H_4 = 0.1721\,d\,, & R_2 &= R_4 = 0.4309\,d\,, \\
H_3 &= 0.2888\,d\,, & R_3 &= 0.5000\,d\,.
\end{aligned}
\tag{2.38}
$$

The radii and heights are those defined in Fig. 2.6, where results for photonic band dispersion are given. The radius of cylinder no. 3 turns out to be the same as the radius of the sphere. The condition that the total height is equal to sphere diameter is essential in order to give a good representation of light coupling at the interfaces for an opal of finite size. In this case the interface between air and opal (or substrate and opal) has a corrugated profile due to sphere caps, that is reproduced, at least roughly, by the outermost cylinders. This is certainly not the case of the one or three cylinders approximation,

where there is no interpenetration region.

In Fig. 2.6 the band dispersion for the fcc structure with both spheres and cylinders is shown. The agreement of the photonic bands is amazingly good, even in the high-energy region (where the folding of free-photon bands corresponds to the occurrence of diffraction) and also along directions different from ΓL, i.e. for non-normal incidence. The overall error between the two band dispersions does not exceed 2%: this means that the approximation error lies within the the polydispersity of the spheres in real samples and, subsequently within the possible experimental error.

A pretty good feature to notice is that the gap in X point is no more noticeable: this is an effect of the improvement in modelling the sphere geometry by a consistent number of cylindrical slices. Furthermore, the increased number of sphere slice yields a better geometrical approximation of the sphere, hence the cylinder parameters are less dependent on dielectric contrast between the air and the dielectric. Due to this robustness, these are the parameters that have been used for all the optical spectra calculations presented in this thesis.

Chapter 3

Low-energy region: band structure and optical spectra

In this chapter the optical properties of opal-based photonic crystals (PhCs) in the energy region of the first pseudogap are studied. First of all results for transmission and optical phase delay at normal incidence, varying the sample thickness, are presented: the calculated spectra will be compared with experimental measurements. Subsequently, from these two quantities the concepts of group velocity and effective refractive index will be derived and analysed in detail. In the second section, the optical properties for finite incidence angle along ΓW direction will be investigated. The role of mixing between TE and TM polarization with respect to ΓLW plane in the first Brillouin zone will also be analysed. Finally, theoretical calculation will prove that there is a threefold symmetry axis perpendicular to sample surface, in opals grown along [111] direction and that LU and LK direction, albeit indistinguishable in reflection, are clearly not equivalent.

3.1   Optical properties in the first pseudogap region

By means of the scattering matrix method, involving the five-cylinder approximation, described in Chapt. 2, we calculate the transmittance $T(\omega)$ and the absolute phase delay $\varphi(\omega)$ of the light beam transmitted through the crystal. Such quantities have been obtained for opal films having different number of layers in order to investigate their dependence on crystal thickness. From the absolute phase delay it is possible to derive the group velocity v_g or, better, the group index c/v_g that gives information on the dynamics of light propagation inside the crystal. Besides, the real and imaginary parts of the effective refractive index n_{eff} of the structure can be retrieved from the above mentioned quantities, allowing to analyse thoroughly the interaction between light and crystal and, most of all, the role of structural disorder, present in real samples.
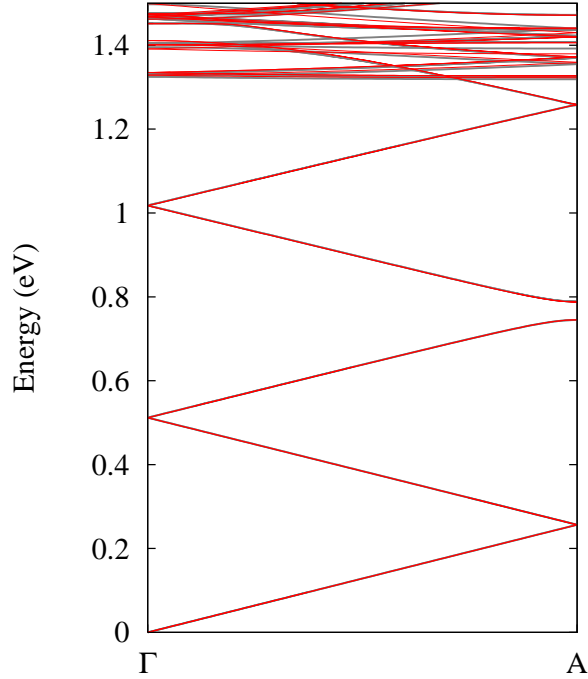
Figure 3.1: Photonic band structure of the relaxed lattice described in the text for a polystyrene opal ($\varepsilon_{\mathrm{poly}} = 2.455$): plotted in thick grey line is the dispersion calculated for the sphere layout, while in thin red line are the bands obtained by means of the five-cylinder approach. The in-plane lattice constant is assumed equal to 730 nm, the sphere diameter d is 705 nm and the cylinder parameters are equal to those introduced in Sect. 2.4.

These theoretical results have been compared to experimental measurements presented in Ref. [29]. Employing a white light interferometry set-up [122] in the time domain, phase delay and transmittance were recorded for samples having an increasing number of layers in a large spectral range (from visible to near infra-red). The samples measured consisted of artificial opals made of polystyrene spheres, having a diameter equal to 705 nm within 3% of polydispersity and a controlled thickness, grown on glass substrate [104].

In order to model more realistically the optical response of opal PhCs, in the theoretical calculations the dispersion of the dielectric function $\varepsilon_{\mathrm{poly}}(\omega)$ of polystyrene has been taken into account by using published data [123]. The Bragg peak in experimental measurements is located at higher frequency with respect to theoretical calculations performed with a face centered cubic (fcc) lattice. This discrepancy could be reduced by assuming a smaller diameter for the spheres, due to the scalability of the band structure, but this would lead a value of 685 nm, at the lower limit of polydispersity. Otherwise, a slight relaxation of the in-plane lattice, that decreases the mean refractive index, can be considered to match the spectral position of the Bragg peak. The latter is justified from the fact that according to diffraction measurements, the lattice

parameter b of in-plane triangular arrangement has been observed to be equal to 725-730 nm. These values are quite different from the sphere diameter of 705 nm, but they still remain within the limits of polydispersity. The best agreement with experimental results is obtained leaving unchanged the distance between two consecutive layers, namely $a/\sqrt{3}$, a being the fcc constant, along the vertical direction. Thus we believe that the sphere arrangement in the sample measured presents a small deviation from a truly fcc one, probably due to the difference in size of the spheres. While the in-plane arrangement is dominated by larger spheres resulting in a relaxed triangular lattice, the vertical stacking depends on the mean diameter value without any variation from the actual value of $a/\sqrt{3}$. In order to prove the validity of the five cylinder approximation even for this relaxed lattice, in Fig. 3.1 a comparison between the photonic band structure calculated both for the sphere and cylinder layout is presented. This relaxed lattice has to be described by an hexagonal lattice similar to that introduced in App. A.2, hence bands are plotted along ΓA line in the Brillouin zone: this is the direction explored in normal incidence experiments and it corresponds to the ΓL direction in the fcc reciprocal lattice. Since the hexagonal unit cell is three times larger than the fcc one, the bands are folded three times in the figure. It should be remembered that in the plane wave expansion method the frequency dispersion of the dielectric function cannot be taken into account, hence we assumed a dielectric constant $\varepsilon_{\text{poly}} = 2.455$ for polystyrene, close to the phenomenological value in the surroundings of the first pseudogap. The agreement between the actual band structure and the approximated one is certainly satisfactory, even in the high-energy region, proving the validity of our optical spectra calculations, as can be deduced from Fig. 3.1.

3.1.1 Transmission and phase delay

From the scattering matrix code we retrieved transmittance and phase delay for unpolarized light impinging on the sample normally to the surface. Figure 3.2 presents a comparison between the calculated and measured quantities, for samples with an increasing number of layers, from 10 up to 40, as indicated in the panels.

In transmittance spectra, a dip can be observed in Fig. 3.2(a) associated to the stop band opening in the dispersion relation, at the edge of the first Brillouin zone at the L point. The dip becomes more pronounced for thicker samples, reaching very small values close to zero for 31 and 40 layer opal films. The pseudogap that opens in L point is related to Bragg diffraction by the [111] planes, parallel to sample surface: the efficiency of Bragg diffraction increases with the number of layers. Eventually, in the limit of infinite crystal, transmission vanishes because in this frequency region only wavevectors with an imaginary component are allowed: inside the crystal there would be only an evanescent field near the surface and light would be totally reflected. Outside the stop band secondary oscillations appear, clearly visible in calculated
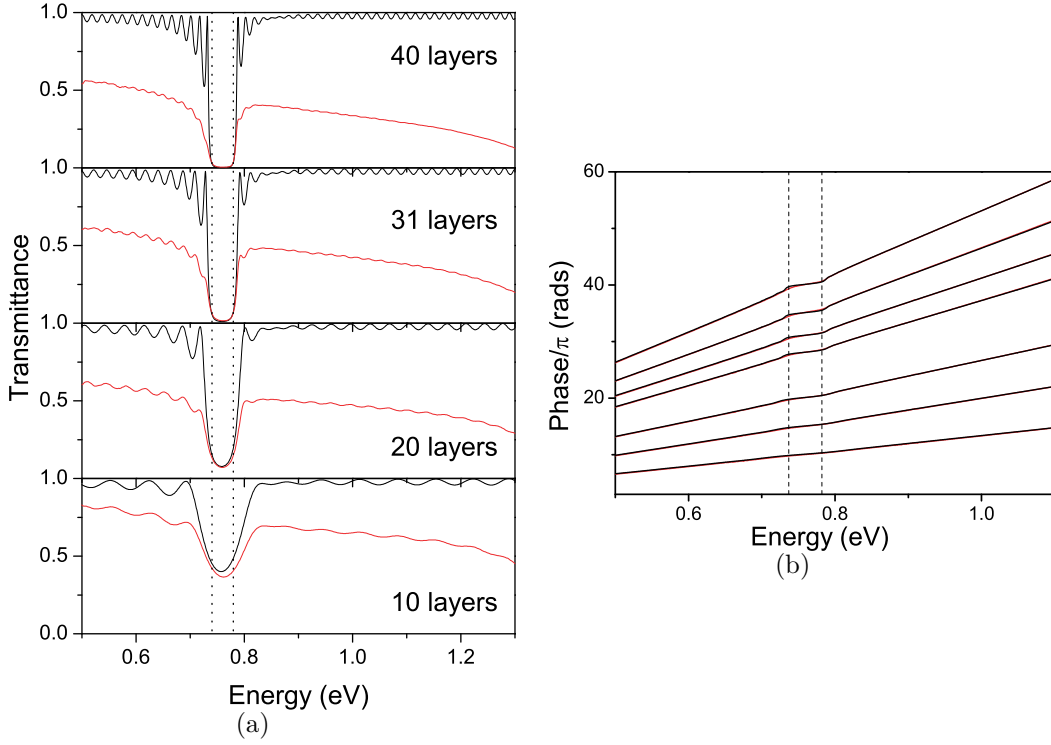
Figure 3.2: (a) Transmission spectra and (b) absolute phase delay for polystyrene opals, having an increasing thickness. In red line the experimental data are shown, while in black line theoretical data obtained by means of scattering matrix calculations are presented. The opal thickness whose phase data are presented are, from bottom to top, 10, 15, 20, 28, 31, 35 and 40 layers, respectively; transmission data are shown only for 10, 20, 31 and 40 layer samples, as indicated. Vertical dashed lines indicate the edges of the stop band as extracted from band calculations.

spectra, but also present in experimental measurements: they are due to the finite size of the samples, representing interference fringes between the light beams reflected at the air and glass interfaces of the sample, and they are usually known as Fabry-Pérot oscillations. The decreasing background present in measured transmittance spectra, which is absent in theoretical ones, is mainly related to structural disorder, causing light diffusion in the sample [26, 64]. The role of the unavoidable disorder present in real samples, partly due to the dispersion in size of the spheres and partly due to the self-assembly process, will be explored later, when dealing with the imaginary part of effective refractive index.

Regarding Fig. 3.2(b), it can be noticed that phase delay shows a linear behaviour, with a slope change in the region of the stop-band. For the thinner samples the change in slope is rather small, while the phase delay becomes flatter in this region increasing sample thickness. A similar jump is known to occur in one dimensional PhCs [124], being a signature of Bragg diffraction in the forbidden stop bands. In analogy to what has been said for transmittance

38

spectra, the change in slope of the phase delay accounts for the evolution towards the infinite crystal behaviour, where a phase change of π across the pseudogap is predicted [41]. Here we have to describe separately the theoretical data and the experimental ones. In the former the phase delay is derived from the coefficients of the light states for the incoming and outgoing waves. If the light undergoes to a strong extinction inside the crystal the phase delay of the outgoing states can be retrieved even if it is an evanescent state. On the other hand in the experimental measurements phase delay is obtained from the transmitted beam: in our case, experimental transmittance reaches very small, but finite values, hence phase delay can be determined without losing its meaning even in the stop band. We would like to point out here that the calculated phase is an absolute one: it is calculated starting from $\omega = 0$ and then is unwrapped by adding a proper multiple of 2π in order to obtain a continuous quantity, as the values coming out of the code are contained between $-\pi$ and π. The curves obtained in this manner help in retrieving the absolute phase measured by the interferometer, as in this case measurements start from a finite value of frequency different from zero. Once again the agreement between theory and experiment is excellent: only slight deviations in the low-energy side of the pseudogap are present. These discrepancies become more evident when dealing with group index or effective index, hence they will be explained extensively in next subsection.

3.1.2 Group velocity and effective refractive index

From the transmittance coefficient and the absolute phase delay, either obtained from numerical computation or experimentally measured, one can derive other physical quantities, such as group velocity or effective refractive index, which play an important role in order to clarify the dynamics of interaction between the propagating light beam and the PhC.

The group velocity is usually defined as the speed at which the peak amplitude of a light pulse propagates through a medium. For an infinite PhC, group velocity can be extracted from band dispersion considering that it is the derivative of $\omega(\mathbf{k})$ with respect to $\mathbf{k}$, hence it is related to the slope of the bands [43]. On the other hand, for a finite-size PhC, the group velocity of light travelling along the ΓL direction, that is the direction involved with normal incidence measurements, can also be extracted from the phase delay, as $\varphi(\omega) = Dk$, D being the crystal thickness. In our case we derive the group index n_g, i.e. the inverse of v_g, normalized to the speed of light c, as expressed in the following relationship:

$$n_g = \frac{c}{v_g} = \frac{c}{D}\frac{d\varphi}{d\omega}. \tag{3.1}$$

In an infinite PhC, when extinction is absent v_g equals the energy velocity, i.e. the speed at which electromagnetic energy propagates [41]. When no
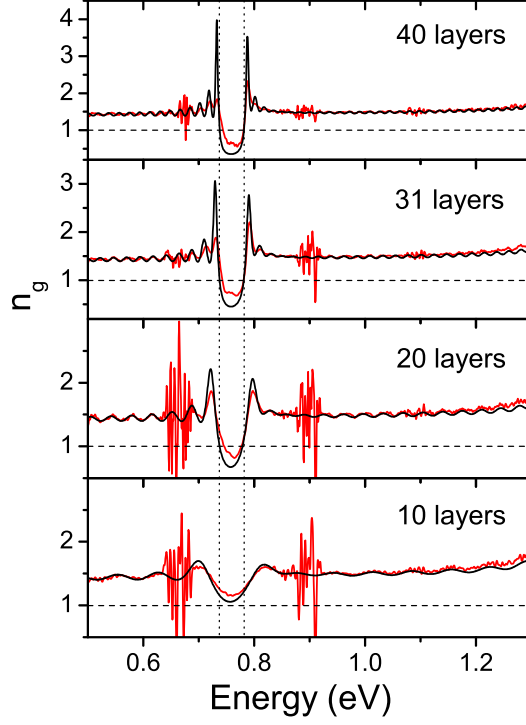
Figure 3.3: Group index for samples having an increasing number of layers, indicated in the panels. Horizontal dashed lines indicate the limit of superluminal velocity $v_g = c$. Vertical dotted lines indicate the pseudogap edges predicted by calculated bands. Experimental data appear in red line, while theoretical calculation are presented in black.

electromagnetic state is allowed inside the crystal, neither the group velocity nor the energy velocity can be defined. Otherwise for a finite crystal, such as the opal films currently investigated, light is exponentially attenuated but it may still be transmitted through the crystal, as shown in Fig. 3.2(a), hence v_g can still be obtained from the phase delay even if it does not equal the energy velocity [5]. Fig. 3.3 shows the frequency dispersion of n_g for samples having a different number of layers. The theoretical calculations, plotted in black line, reproduce very well the experimental curves in the whole spectral range. The small oscillations due to the finite thickness of the sample and related to Fabry-Pérot fringes in reflectance and transmittance spectra, are perfectly matched in position and intensity, besides small deviations at higher frequencies. The main discrepancy is observed at the lower edge of the pseudogap: here the predicted value is bigger than the measured one and contrarily to experiment it reaches a greater value with respect to the high-energy edge peak [1]. A possible

---

[1]Spectral region where n_g changes rapidly are present at both sides of the pseudogap region in the experiment and correspond to water absorption [29]

3.1. Optical properties in the first pseudogap region

explanation for this behaviour is the fact that when the group velocity is small the time of interaction between the light and the crystal increases, hence the possibility for light being scattered by defects inside the crystal increases. The difference between the high-energy edge and low-energy one may be related to the fact that the in the lower band the field is mainly confined in dielectric medium, nevertheless it may be due also to the particular relaxed model we assumed for the structure.

For thin opals n_g has small variations, even if the Bragg peak is clearly visible. Increasing the number of layers, two narrow peaks appear at energies corresponding to those of the stop band edges. As mentioned before the bands become flat in this region, consequently the group velocity slows down to very small values: in the limit of an infinite crystal v_g vanishes at the two stop band edges. The thicker the sample, the smaller these values become: this is another evidence supporting the evolution towards the infinite crystal behaviour.

For frequencies within the pseudogap, n_g assumes values smaller than unity, at least if the sample is thick enough. This means that group velocity is greater than c, the speed of light in vacuum, when travelling through the crystal. As we have seen from transmission spectra and band dispersion, in this region the light beam undergoes a strong extinction, hence the energy values remains below c for all frequencies, not violating the causality principle.

In order to better understand the role of disorder and the dynamics of light interaction within the crystal we analyse the effective refractive index of the structure, in its real and imaginary part. The complex transmission coefficient $t(\omega)$ of a system is defined as:

$$t(\omega) = [T(\omega)]^{1/2} e^{i\varphi(\omega)}, \tag{3.2}$$

where $T(\omega) = |t(\omega)|^2$. Starting from the absolute phase delay $\varphi(\omega)$ and the transmission intensity $T(\omega)$, the effective refractive index n_{eff} is given by the following relationship:

$$
\begin{aligned}
n_{\text{eff}} &= \Re(n_{\text{eff}}) + \Im(n_{\text{eff}}) \\
&= \frac{c}{\omega D}\varphi(\omega) - i\frac{c}{2\omega D}\ln[T(\omega)],
\end{aligned}
\tag{3.3}
$$

where D is the thickness of the sample and it has been taken equal to the number of layers times $d_{111} = a/\sqrt{3}$, i.e. the distance between two consecutive planes in vertical direction. The present definition for n_{eff} has been firstly introduced by Centini and co-workers [4] to describe the optical properties of one dimensional PhCs and it has been applied to investigate the conditions that enhance second harmonic generation in such crystals. In this low-energy region the optical properties of thin opal films are dominated by the vertical periodicity, i.e. by diffraction from [111] planes, therefore the definition given for one dimensional PhCs is a valuable tool to study the dispersive properties of these structures. We would like to stress the fact that, unlike the definition
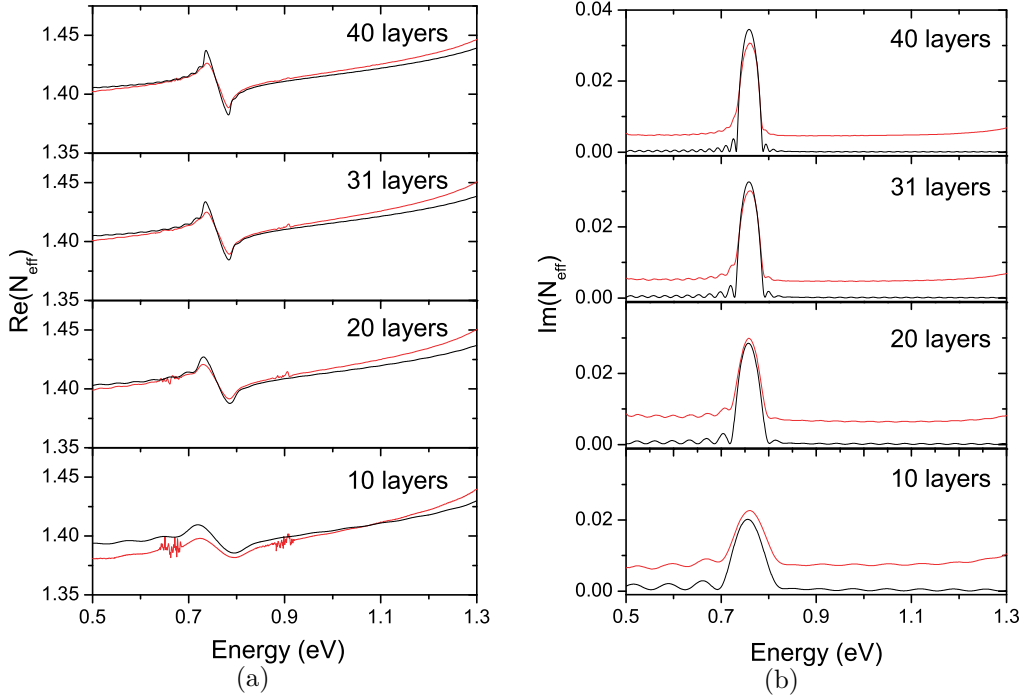
Figure 3.4: (a) Real and (b) imaginary part of the effective refractive index estimated from the absolute phase delay and the transmission coefficient for different sample thicknesses: from bottom to up, 10, 20, 31 and 40 layers. Vertical dashed lines indicate the edges of the stop band as extracted from band calculations. Experimental data appear in red line, while theoretical calculation are presented in black.

given by Notomi [108], where the refractive index is derived from equifrequency surfaces and it is a property of an infinite PhC, the present definition for effective index accounts for dispersive properties of these *finite* samples along a given direction for light propagation, normal incidence in our case.

Fig. 3.4(a) shows the real part of n_{eff}, derived both from theoretical and from experimental absolute phase. The agreement between the two seems to increase for thicker samples. First of all we notice that for lower frequencies the refractive index tends to

$$\bar{n} = \sqrt{\bar{\varepsilon}} = \sqrt{f\varepsilon_{\text{poly}} + (1-f)\varepsilon_{\text{air}}}\,. \tag{3.4}$$

where f is the filling fraction of the dielectric material, with respect to air. For the relaxed lattice we took into consideration in theoretical calculation the filling factor is 0.69, clearly smaller than that of a fcc lattice ($f_{fcc} = 0.74$).

Then, small fringes related to Fabry-Pérot oscillations are observed in all the spectral range, apart from the stop band. Here the slope of n_{eff} changes its sign, revealing a region of anomalous dispersion that becomes narrower with increasing thickness, in perfect agreement with the narrowing of Bragg peak in transmittance spectra. A systematic discrepancy between theory and
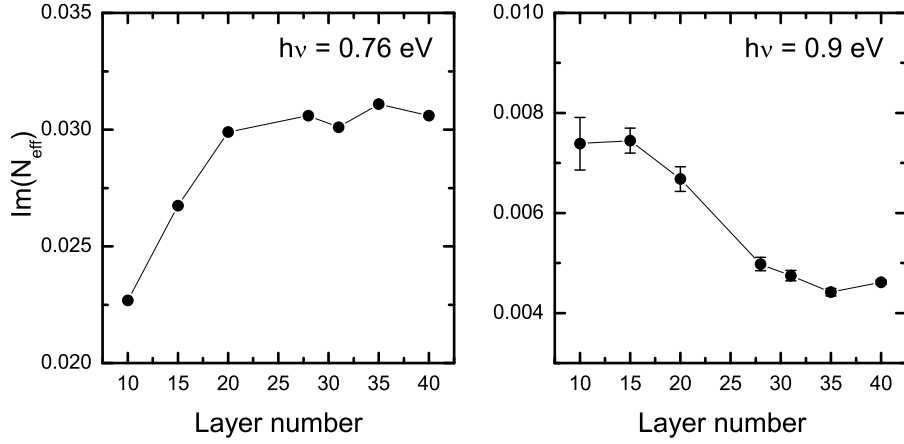
42

Figure 3.5: Evolution of the imaginary part of the effective index as a function of the number of layers, determined from experiments: in the left panel for a frequency inside the stop band and on the right for a frequency outside of it. The error bar in right panel take into account the presence of Fabry-Pérot fringes.

experiment appears at the low edge of stop band, ascribable to an increased interaction of light with the PhC which boost the effect of disorder: increasing incoherent scattering, which does not contribute to the measured phase. Moreover the values derived from experimental data are smaller than the theoretical ones for lower frequencies while the opposite happens for higher frequencies. This difference is more evident for thinner samples. The phenomenon is probably due to the relaxation that occurs in these self-assembled crystals, as mentioned before: thinner samples presents a filling fraction that is smaller from that assumed in numerical simulations.

The effective index is defined as a complex quantity: its imaginary part, derived from transmission coefficient has been plotted in Fig. 3.4(b), for the same sample thickness as Fig. 3.4(a). Theoretical calculations well reproduce the spectral behaviour of $\Im(n_{\text{eff}})$, showing a pronounced peak for frequencies within the L-pseudogap, due to extinction in the form of Bragg diffraction. Fabry-Pérot fringes are clearly visible outside the stop band: here the background is equal to zero for theoretical data, while it takes a finite value for experimental ones. This behaviour is clearly due to unavoidable light diffusion that causes a reduction of absolute transmittance. The background is absent in the simulation as the structure presents neither defects, nor absorption.

Finally it is worth pointing out the evolution of $\Im(n_{\text{eff}})$ with respect to the number of layers for a frequency inside the stop band and one outside. With this purpose, in Fig. 3.5 a comparison between the two situations is shown. It is quite evident that the trend is opposite in the two cases. Inside the pseudogap the imaginary part increases when the opal film becomes thicker, according to the fact that the dip in transmission evolves towards the infinite crystal model. Outside the gap the values decrease with increasing thickness,
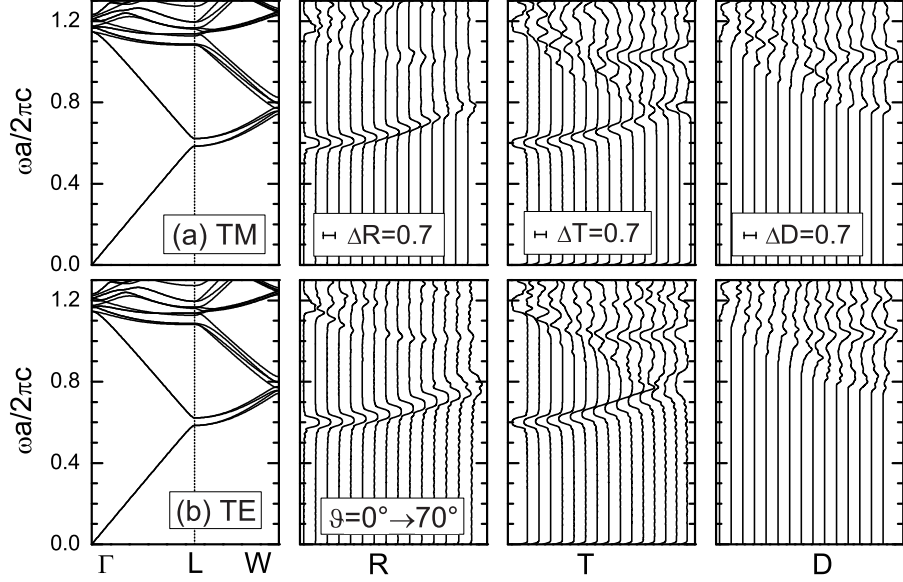
Figure 3.6: Band structure along the LW direction in reciprocal lattice and optical spectra at finite incidence angle in the ΓLW plane for a polystyrene opal made of 21 layers: incident light has (a) TM polarization and (b) TE polarization. The incidence angle θ in air increases in steps of 5 degrees. The spectra are convoluted with a Gaussian lineshape of variance $\sigma a/(2\pi c) = 0.005$.

proving that thicker samples are less affected by disorder. Presumably thin opal films made of a few sphere layers are less stable and hence presents a larger density of intrinsic defects, than thick colloidal crystals where the high number of layers leads to a bulk fcc lattice. Moreover this decreased efficiency of the thinner sample growth may be another reason for the relaxation of the in-plane lattice, that would account for the discrepancy between the theoretical and experimental value of $\Re(n_{\text{eff}})$ for the 10 layer sample.

3.2 Reflectance and transmittance at finite incidence angles

After a detailed analysis of the optical properties for light impinging at normal incidence on the samples, it is worth to study, at least from a theoretical point of view, what happens if the incidence angle is different from zero. Hence we studied the optical properties along the ΓLW direction in Brillouin zone. This orientation should present polarization mixing effects due to the fact that the ΓLW is not a symmetry plane.

3.2. Reflectance and transmittance at finite incidence angles

Hereafter we present the optical spectra in the low-energy region for a polystyrene opal constituted by 21 layers (i.e., by 7 periods along the [111] direction). Since we do not compare the results with experimental data, we assumed an fcc lattice, avoiding any kind of relaxation, and we neglected frequency dispersion for the polystyrene dielectric function, considering the value $\varepsilon_{\text{poly}} = 2.4964$[2], in such a way that optical spectra are consistent with band structure calculations.

In Fig. 3.6 we compare the photonic band structure, calculated by means of the five cylinder approach, along the ΓLW segment in the first Brillouin zone with zero-order reflectance (R) and transmittance (T), as well as diffraction (D) spectra. This quantity has been calculated as

$$D = 1 - R - T, \tag{3.5}$$

representing the intensity of light diffracted in all directions, with the exception of those of the reflected and transmitted beams. The spectra are calculated for transverse magnetic (TM) and transverse electric (TE) polarizations of the incident beam and they are taken for an incidence angle in air that increases from 0 to 70 degrees in steps of 5 degrees. All the curves are convoluted with a Gaussian lineshape of variance $\sigma a/(2\pi c) = 0.005$ in order to approach experimental conditions wherein some broadening is inevitably present. We can clearly see the Bragg peak and its frequency dispersion for different incidence angles, in close agreement with the band structure, for both TM and TE incident light. In the same figure we can also notice a peak in reflection that crosses the pseudo-gap for incidence angles greater than 50 degrees: this feature arises from band coupling occurring near the W-point of the Brillouin zone, related to multiple diffraction from {111} and {200} Bragg planes, as previously observed and discussed [96, 30, 104, 105]. This is confirmed by the examination of diffraction spectra. Between $\omega a/(2\pi c) = 1.0$ and 1.2 we can see many diffraction structures, related to flat bands in that energy region. These structures are more visible in transmittance than in reflectance. Although the diffracted beam subtracts intensity both to the transmitted and reflected beams, the effect on R spectra is a minor one since reflectance is small anyway.

It has to be noticed that the labels TE and TM can be referred only to the incident light beam: in fact, since the ΓLW plane is not a symmetry plane of the fcc structure, there is a mixing between the two polarizations for the outgoing light. The intensity of TM-polarized outgoing light for TE incoming light in transmission and reflection is shown in Fig. 3.7. The incidence angles are the same as in the previous figure and all the curves are convoluted with the same Gaussian lineshape. It can be noticed that there is no mixing at normal incidence, in agreement with group-theoretical considerations in

---

[2]This value for dielectric function is slightly different from that assumed in the previous section. This is due to the fact that the polystyrene function presents a small frequency dispersion, therefore we have chosen the value closer to that of the frequency range we are studying.
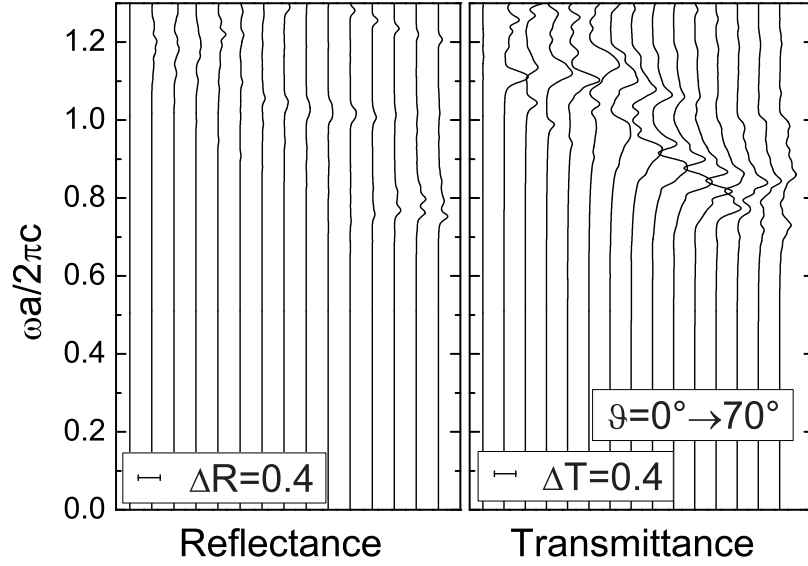
Figure 3.7: Mixing TE-TM, or TM-polarized outgoing light for TE-polarized incoming light, for a polystyrene opal made of 21 layers. The incidence angle θ increases in steps of 5 degrees.

the presence of a three-fold rotation axis. The TE-TM mixing is greater in transmittance than in reflectance and it grows considerably in the same range of angles and energies for which the diffracted intensity becomes appreciable: thus, polarization mixing and diffraction are related to each other. Up to date, the only experimental data available for this sample orientation [104] are not polarization resolved, hence it would be interesting to further extend that work in order to experimentally verify this polarization mixing.

3.3 Evidence of a threefold symmetry axis in [111] oriented opals

In the previous section we investigated the optical properties at finite incidence angle in the ΓLW plane of the first Brillouin zone, i.e. for light impinging on a plane oriented as a hexagon diagonal on the sample surface. Now we want to study the optical behaviour of an opal grown, as usual, along the [111] direction when the plane of incidence is parallel to a hexagon apothem, as shown in Fig. 3.8. In this case, the light wavevector lies in the ΓLU or ΓLK plane, depending on incidence angle.

When looking at the sample surface, one may think that the six incidence planes described by the six apothems are perfectly equivalent, or, better, con-
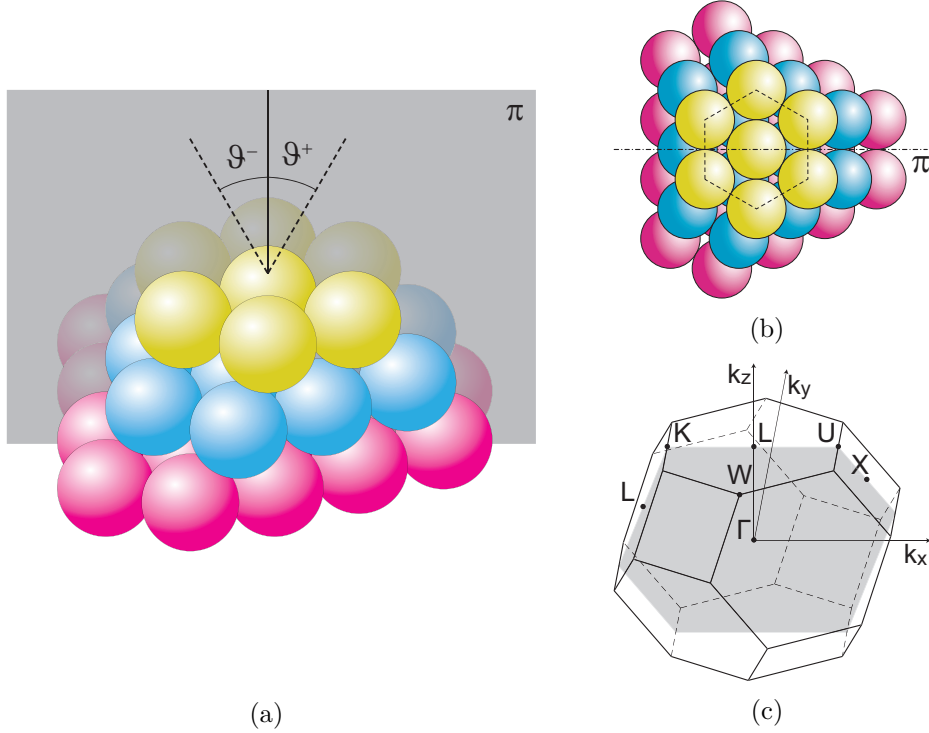
Figure 3.8: (a) Schematic view of the plane of incidence employed for the calculations shown in this section. (b) Top view of the opal structure, the incidence plane π is depicted in dot-dashed line. (c) The Brillouin zone of the fcc lattice: high-symmetry points used in the text are indicated. The grayed area represents the plane of the zone corresponding to the incidence plane.

sidering the incidence plane shown in Fig. 3.8(a), that it is equivalent to impinge from positive or negative incidence angle. Hereafter we will prove that this is not true, due to symmetry features of the fcc lattice: as a matter of fact, it is well known from group theory [43, 125], that at the L point the symmetry point group of the Brillouin zone of an fcc lattice is D_{3d}, hence the cell is invariant with respect to rotations of $2\pi/3$ angles. Moreover, the K and U points are clearly not equivalent: this can be easily seen looking at the Brillouin zone, shown in Fig. 3.8(c), since the former is located on the edge between two hexagonal faces and the latter between a square and a hexagonal one.

In Fig. 3.9 the band structure of an infinite opal made of Silica spheres[3] ($\varepsilon_{SiO_2} = 2.1$) calculated along the $\Gamma L U \Gamma$ line in the reciprocal lattice, highlighted by the red line in the picture on the right side of the figure, is presented. Since the $\Gamma L U$ plane represents a symmetry plane for the first Brillouin zone, it

---

[3]Silica opals are taken into account in this section since these results have been thought to be compared to experimental measurements done on this particular kind of samples. We mention here that we employed the same cylinder parameters as for polystyrene opals (see Chapt. 2), evidencing the robustness of the approximation.
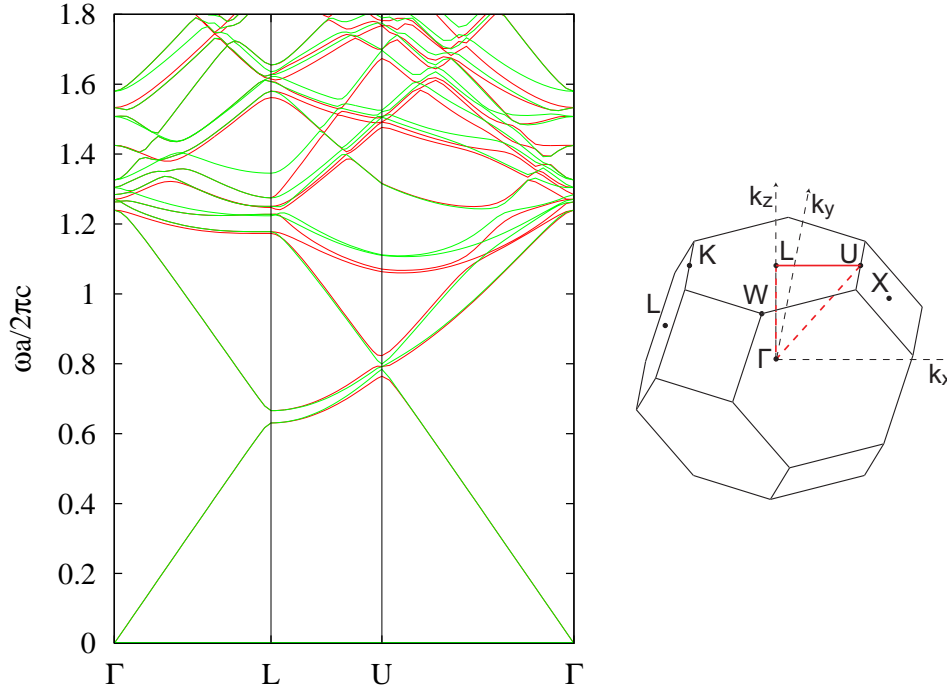
Figure 3.9: Band structure calculated along the ΓLUΓ line in the first Brillouin Zone, indicated on the right side. In red (green) line the modes that are even (odd) for the mirror reflection operator with respect to the ΓLU plane.

is possible to classify the modes in the photonic band dispersion by parity with respect to a mirror reflection operator, hence we plot the even and odd modes by a red and a green line, respectively. Similarly in Fig. 3.10 the photonic band dispersion has been calculated along ΓLKΓ line. It can be noticed that the band structures are identical on the surface of the Brillouin zone (LU and LK segments), while they are rather different when calculated inside the zone (ΓU and Γk), especially for the flat bands in the high-energy region, which are related to diffraction.

The difference between the two directions in reciprocal space can be detected even in optical spectra, but only for transmitted light. When light of a specific frequency propagates through the crystal it assumes a wavevector **k** that is allowed from the photonic dispersion $\omega(\mathbf{k})$. By varying the incidence angle different directions in reciprocal space are probed. The fact that the component $\mathbf{k}_\parallel$ parallel to sample surface is left unchanged when crossing the interface between the air and the opal guarantees that the light wavevector **k** lies always in a well-defined plane of the reciprocal lattice, strictly related to the plane on incidence while only its vertical component, in the present case the projection along the ΓL direction $\mathbf{k}_{\Gamma L}$, changes according to frequency and incidence angle. Hence the optical behaviour for light propagating in the ΓLU or ΓLK plane can be investigated by impinging in a plane as that shown in Fig. 3.8 by changing from positive to negative incidence angle or by rotating
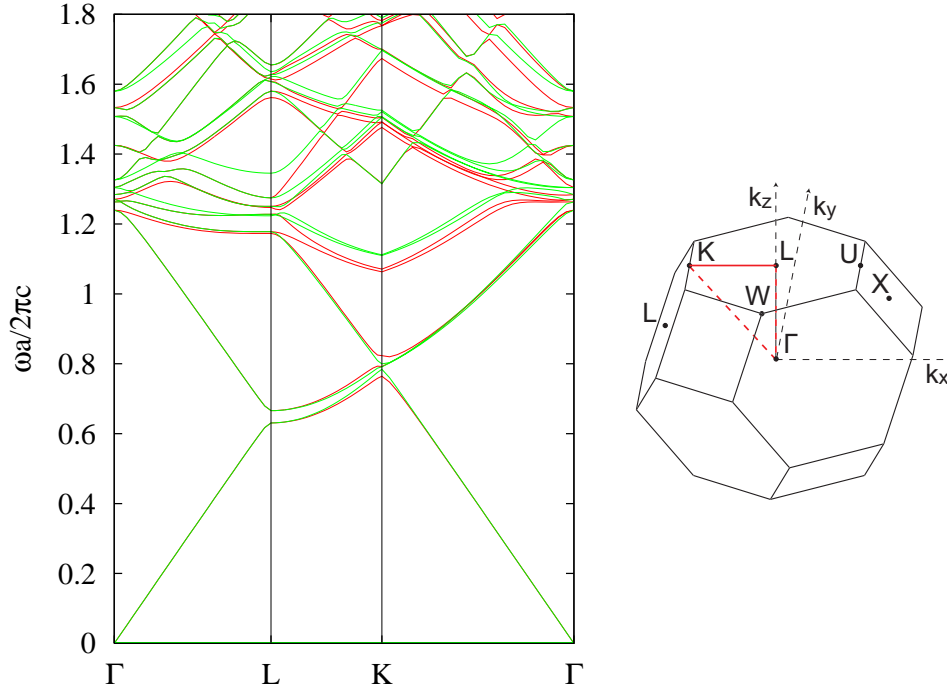
48

Figure 3.10: Band structure calculated along the ΓLKΓ line in the first Brillouin Zone, indicated on the right side. In red (green) line the modes that are even (odd) for the mirror reflection operator with respect to the ΓLK plane.

the sample by 180 degrees. It is not so trivial to understand which of the two planes are probed with positive or negative angles, respectively: basically it depends on the stacking sequence of the sample and on the vertical component of the incoming light wavevector. An intuitive way to identify the reciprocal lattice direction probed by a particular incidence angle is to compare Fig. 3.8(b), that shows a top view of an opal, to Fig. 3.8(c). Assuming the [111] direction as the vertical one, there are six sets of crystallographic planes, each of them related to a hexagon edge on the surface: three sets of planes having the spheres arranged in a square lattice, namely (200), (020) and (002) ones, corresponding to square faces of the Brillouin zone and three sets of hexagonal planes, namely ($\bar{1}$11), (1$\bar{1}$1) and (11$\bar{1}$) ones, corresponding to the hexagonal faces. In our case we are impinging on the top of the sample, hence the vertical component of the wavevector $\mathbf{k}_{\Gamma L}$ is negative. Remembering that U and K are exchanged on the lower face of the Brillouin zone, referring to Fig. 3.8(c), we are probing the ΓLK (ΓLU) plane for positive (negative) incidence angle, according to the reference frame introduced in Fig. 3.8(a). The transmitted beam crosses the sample only in the forward direction hence it probes only one direction in the reciprocal space, but the reflected beam propagates also in the backward direction hence it probes the two orientations and no difference is perceived by measuring reflection with positive or negative incidence angle. Thus if one want to observe the difference between the two directions,
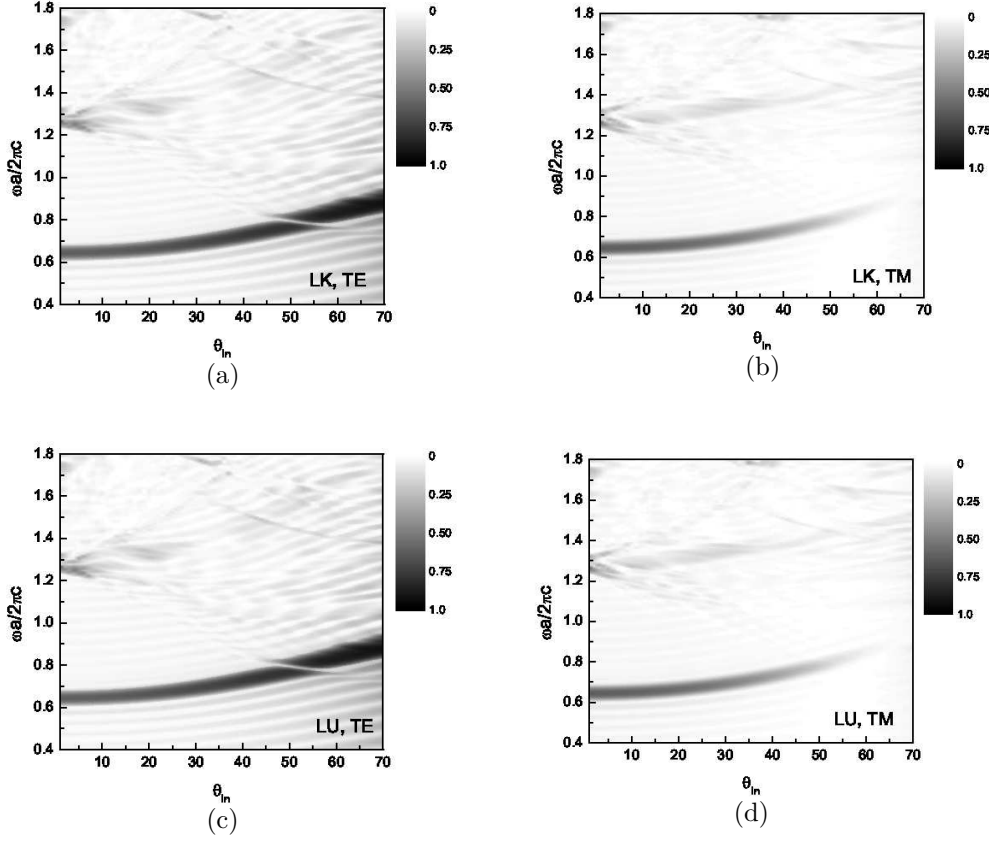
Figure 3.11: Contour plot of reflection intensity with respect to the incidence angle (on x-axis) and to the frequency (on the y-axis). Results are presented for LU and LK direction in the first Brillouin Zone and for the two light polarization, as indicated in the insets.

transmission measurements are needed.

In Fig. 3.11 we show results for reflectance spectra in a contour plot form, for both TE and TM polarized light and for the two sample orientations, calculated for a 12-layer silica opal grown on a glass substrate. The Bragg peak is clearly noticeable at normal incidence for reduced frequencies of about $0.65\omega a/(2\pi c)$ and its frequency dispersion with respect to incidence angle is plainly pointed out. At higher energies a number of peaks related to diffraction bands are present: we will analyse these features later, since they are more evident in transmittance spectra. In the whole spectral range one can notice the presence of Fabry-Perót fringes, due to the finite size of the sample. Nevertheless these spectra do not give any information about the two orientations: as discussed before, the reflected beam probes the whole Brillouin zone and, as a result, it does not display any difference between LU and LK directions.

On the other hand, in Fig. 3.12 contour plots of transmission intensity are presented for TE and TM polarization and for light having a wavevector in
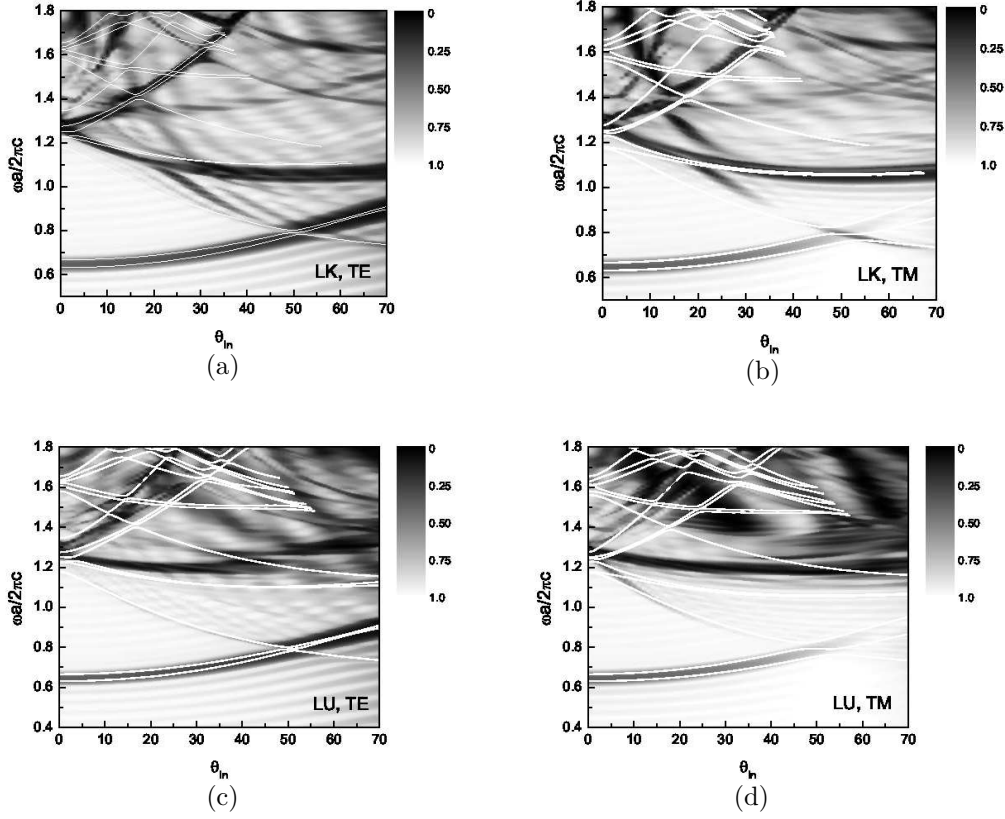
Figure 3.12: Contour plot of transmission intensity with respect to the incidence angle (on x-axis) and to the frequency (on the y-axis). Results are presented for LU and LK direction in the first Brillouin Zone and for the two light polarization, as indicated in the insets. Superimposed in white line photonic band dispersion with respect to incidence angle are plotted in order to highlight the agreement with optical spectra.

ΓLU or ΓLK plane. Superimposed on the transmittance spectra the photonic band structures calculated along a specific line of the reciprocal lattice are plotted with respect to the incidence angle, to show that the peak dispersion in optical spectra is strictly related to photonic band dispersion.

For Fig. 3.12(c) and Fig. 3.12(d), the reciprocal lattice line is described by the following points:

$$\begin{aligned}
\text{L} &= \frac{2\pi}{a}(1/2, 1/2, 1/2)\,, \\
\text{U} &= \frac{2\pi}{a}(1/4, 1/4, 1)\,, \\
\text{U}' &= \frac{2\pi}{a}(0, 0, 3/2)\,,
\end{aligned} \tag{3.6}$$

where the U' point is chosen in such a way that it lies on LU line and the distance $\overline{\text{UU}'}$ is double with respect to $\overline{\text{LU}}$. The modes have been classified by parity, hence for TE (TM) polarization we show only the odd (even) modes. It has to be mentioned that, due to the fact that light couples to a mode with

a well-defined parity, there is no polarization mixing for incoming light having a wavevector in this plane.

Regarding Figs. 3.12(a) and 3.12(b), band structure has been calculated along a line joining the following points:

$$
\begin{aligned}
\text{L} &= \tfrac{2\pi}{a}(1/2, 1/2, 1/2)\,, \\
\text{K} &= \tfrac{2\pi}{a}(3/4, 3/4, 0)\,, \\
\text{K}' &= \tfrac{2\pi}{a}(1, 1, -1/2)\,,
\end{aligned}
\tag{3.7}
$$

where the K point is not the one defined in App. A.1, but a more convenient one, arranged along LU line. The K' point is chosen in such a way that it lies on LK line and the distance $\overline{\text{KK}'}$ is double with respect to $\overline{\text{LK}}$.

The incidence angle has been retrieved from the wavevector $\mathbf{k}$ in reciprocal space, remembering that the in-plane momentum $\mathbf{k}_\parallel$ is preserved at the interface between air and sample:

$$
\theta_{in} = \arcsin\left[\frac{c}{\omega}|\mathbf{k} - \mathbf{k}_{\Gamma L}|\right]\,,
\tag{3.8}
$$

where c is the speed of light in vacuum, ω the frequency of incident light and $k_{\Gamma L}$ the component of the wavevector $\mathbf{k}$ inside the crystal along the vertical direction.

The comparison between bands and spectra is fairly good, especially in the low-energy region. The discrepancies can be ascribed partly to the finite size of the sample that has not be taken into account in band structure calculation and partly to the fact that we show only the band structure on a plane of Brillouin zone, while the light propagation is affected by the bands of the whole cell, as explained before. Nevertheless the comparison gives an intuitive picture of the origin of the transmission peaks: the Bragg peak shows a really good match with the pseudogap at L point, while high-energy peak are related to diffraction band presenting a low dispersion. The Fabry-Perót fringes, noticeable in the whole spectral range of transmission plots, are related to the finite size of the structure implemented in the scattering matrix code and hence do not correspond to any feature of the band structure of the bulk system.

A pretty good feature to notice, that helps in distinguishing LU and LK spectra, is indeed the Bragg peak dispersion. In particular for LK spectra we can clearly notice the presence of an anticrossing between the Bragg peak and a diffracted mode at about 50 degrees. For higher angles the Bragg peaks dispersion is negative. Contrarily there is no evidence of Bragg peak for higher angles in the LU direction spectra. As mentioned before, the U point is located on the edge belonging to a square and a hexagonal face of the Brillouin zone, hence if the incidence angle is high enough we are retrieving the optical behaviour in the surroundings of a X point, where no pseudogap opens up. On the other hand the K point lies between two hexagonal faces and for high incidence angle we are once again close to an L point, hence we still observe a dip in transmittance spectra.

In conclusion, we have shown that in opal-based PhCs it is possible to prove the non-equivalence between the U and K points of fcc Brillouin zone, evidencing a threefold symmetry axis perpendicular to sample surface. This property is clearly noticeable in transmittance spectra and in photonic band structure when calculated for points inside the Brillouin zone.

Chapter 4

Supercell calculations

In this Chapter photonic band structure calculations, performed by means of a supercell method, will be presented. This particular procedure allows us to study, in the first section, the photonic modes of a thin opal film, which can be very different from those of a bulk photonic crystal (PhC). Finally we will analyse the band dispersion of an opal-based PhC wherein a planar defect has been introduced.

4.1 Finite-size effects

Some of the optical properties of thin opal PhCs, especially in the high-energy region, are strongly affected by the finite and small number of layers along vertical direction, as we will see in Chapt. 5. As reflectance and transmittance are closely related to photonic band structure, it would be useful to determine the band dispersion of a system presenting a finite number of layers, instead of a bulk PhC.

Supercell schemes are well known in solid state physics, when dealing with surface states that cannot be evaluated using standard expansion methods with real wavevectors. In these approaches the relevant equations are solved in the primitive unit cell and the periodicity is reckoned with Bloch theorem. When dealing with a finite-size system, or a structure presenting an intentional defect, the periodicity is somehow broken, at least in one dimension, and Bloch theorem does not hold anymore: to solve the problem by means of a Fourier expansion method, such as plane wave one, we have to introduce a fictitious periodicity repeating the whole finite structure.

In our case opal films present a small number of layers along [111] direction, i.e. normal to the surface, but they preserve the in-plane periodicity of dielectric function. Hence we need to introduce a supercell with an in-plane triangular lattice and including in the basis a number of spheres, stacked in the vertical direction, equal to the number of opal layers and a proper air thickness on both sides of the crystal. Moreover, as samples are usually grown on a substrate and
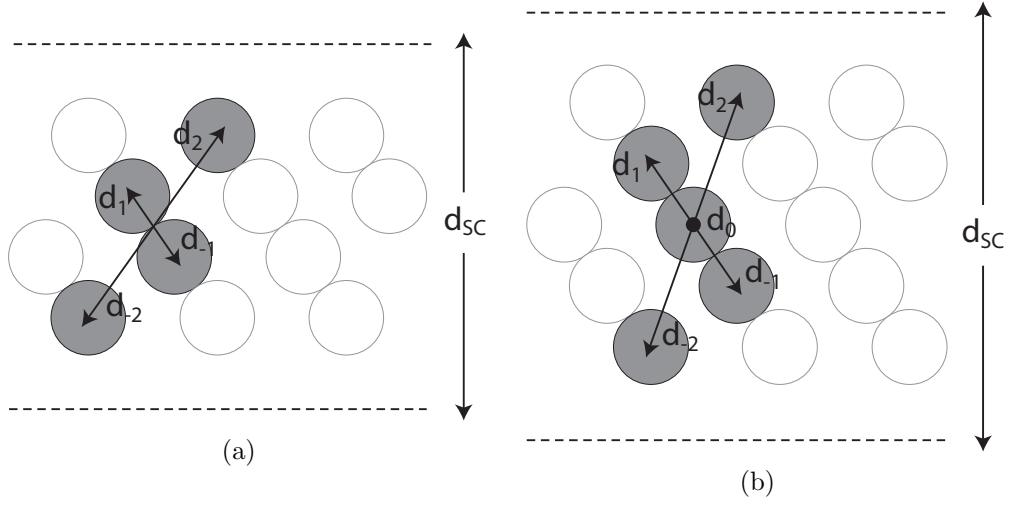
Figure 4.1: Front view of the supercell representing a thin opal film embedded in air and constituted by (a) an even number and (b) an odd number of layers. Characteristic lengths are indicated in the two drawings.

this has to be taken into account when comparing theoretical calculations to experimental measurements, we will also analyse the example of an asymmetric supercell, where the crystal is sandwiched between air and a dielectric medium constituting the substrate.

Symmetric supercell. If the opal film is simply embedded in air, its photonic band structure can be investigated by means of a symmetric supercell containing n_1 spheres, which correspond to the n_1 layers of the sample, enclosed between two air layers high enough to make negligible the interaction between two adjacent cells. The situation is depicted in Fig. 4.1(a), for a thin opal with an even number of layer, and in Fig. 4.1(b), for the case of an odd number of layers. Considering opals grown along [111] crystallographic direction, the lattice cell takes the form of a sequence of hexagonal planes along vertical direction, similar to the one presented in App. A.2, described by the following vectors:

$$\mathbf{b}_1 = b\,(1,0,0)\,, \quad \mathbf{b}_2 = b\left(\frac{1}{2}, \frac{\sqrt{3}}{2}, 0\right)\,, \quad \mathbf{b}_3 = h_{\mathrm{SC}}\,(0,0,1)\,, \qquad (4.1)$$

where b is the lattice constant of triangular lattice and it is equal to sphere diameter. For convenience, the two air thicknesses on both side of the crystal has been expressed by an integer multiple, namely n_2, of d_{111} length, in such a way that the total height of the supercell results:

$$h_{\mathrm{SC}} = (n_1 + 2n_2)d_{111}\,. \qquad (4.2)$$

Strictly speaking the true opal and air thicknesses in the supercell are:

$$h_{\mathrm{op}} = n_1 d_{111} + H_{\mathrm{cap}} \quad \text{and} \quad h_{\mathrm{air}} = 2n_2 d_{111} - H_{\mathrm{cap}}, \qquad (4.3)$$

where H_{cap} is the height of sphere caps defined in Sect. 2.1. Defining the air thickness as a multiple of the vertical lattice constant has the advantage of giving an intuitive picture of the characteristic lengths of the supercell.

Maintaining the cell symmetric implies real components of Fourier transform and, consequently, a less time-consuming code, as it has to deal with real matrices. Hence it is desirable to define the basis vectors in the two different examples presented in Fig. 4.1 preserving inversion symmetry. As a matter of fact, in the case illustrated in Fig. 4.1(a), where n_1 is an even number, the origin has to be chosen at the contact point between two spheres belonging to consecutive layers. The basis vectors are thus defined as:

$$
\begin{aligned}
\mathbf{d}_\nu &= b\left(0, \frac{\nu - 1/2}{\sqrt{3}}, (\nu - 1/2)\sqrt{\frac{2}{3}}\right) \\
&= a\left(0, \frac{\nu - 1/2}{\sqrt{6}}, \frac{\nu - 1/2}{\sqrt{3}}\right),
\end{aligned}
\tag{4.4}
$$

where $a = b\sqrt{2}$ is the lattice constant of the related face centered cubic (fcc) lattice and $\nu = \pm 1, \pm 2, \ldots, \pm n_1/2$.

Otherwise, if the layers are in an odd number, the origin has to be taken at the center of the sphere in the middle of the cell and the basis vectors are given by:

$$
\begin{aligned}
\mathbf{d}_\nu &= b\left(0, \frac{\nu}{\sqrt{3}}, \nu\sqrt{\frac{2}{3}}\right) \\
&= a\left(0, \frac{\nu}{\sqrt{6}}, \frac{\nu}{\sqrt{3}}\right),
\end{aligned}
\tag{4.5}
$$

where ν assumes all the integer numbers in the range $[-(n_1 - 1)/2; (n_1 - 1)/2]$.

Asymmetric supercell. Let us now consider a thin opal grown on a substrate. This is the situation more commonly explored in experimental measurements and it has to be taken into consideration if one wants to improve the comparison between theory and experiment.

A scheme of this supercell, for both even and odd number of layers is shown in Fig. 4.2. The lattice and basis vectors denoting sphere positions inside the cell are defined by Eqs. (4.1), (4.4) and (4.5), as in the previous example of a symmetric cell. Then we have to consider two layers of the same thickness, one on the top characterized by a dielectric function ε_{air}, the same of the medium embedding the spheres usually represented by air, and one at the bottom with dielectric function ε_{sub}, representing the substrate. The heights of these two layers and of the opal sample are the following:

$$
\begin{aligned}
h_{\text{sub}} &= h_{\text{air}} = n_2 d_{111} - \frac{H_{\text{cap}}}{2}, \\
h_{\text{op}} &= n_1 d_{111} + H_{\text{cap}},
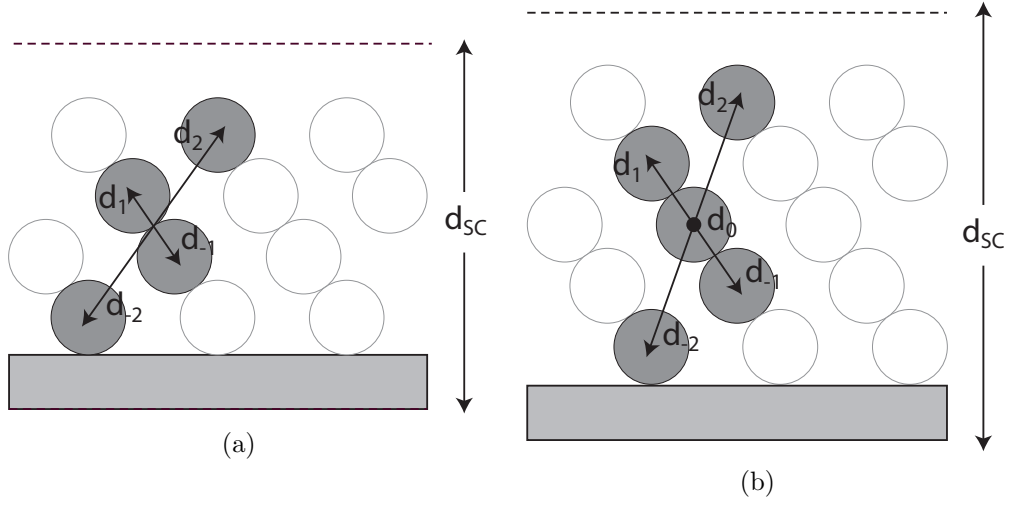\end{aligned}
\tag{4.6}
$$

Figure 4.2: Front view of the asymmetric supercell representing a thin opal film growth on a dielectric substrate and constituted by (a) an even number and (b) an odd number of layers. Characteristic lengths are indicated in the two drawings.

defined in such a way that, similarly to the previous case, the total height of the cell is:

$$h_{SC} = (n_1 + 2n_2)d_{111} \,. \tag{4.7}$$

A comparison between the band structure calculated by means of the two previously described supercells is shown in Fig. 4.3. In the two examples the thin opal film is constituted by ten layers of polystyrene spheres in air: in Fig. 4.3(a) the band dispersion plotted in black line has been obtained sandwiching the crystal in $n_2 = 4$ air layers, while in Fig. 4.3(b) the bottom air thickness has been replaced by $n_2 = 4$ glass layers. The value chosen for n_2 guarantees that the interaction between two consecutive crystal films are small enough to allow the observation of the effects related to an isolated opal film, as we will prove later on. In green line the band structure of an infinite opal is plotted.

The bands have been calculated along ΓA direction in Brillouin zone, corresponding to ΓL direction for fcc lattice. Supercell data are folded $(n_1 + 2n_2)/3$ times in the reduced zone of a bulk opal since the supercell is larger than the primitive unit cell along vertical direction. To reduce convergence errors due to plane wave truncation in the numerical code, in all the calculations the number of waves is chosen in such a way that all the reciprocal lattice vectors having a modulus smaller than a specific value are taken into account. In general, increasing the number of layers in the supercell implies a larger number of plane waves in the expansion in order to reach the convergence, resulting in a more time-consuming code. Nevertheless the supercell method is an effective way to study the photonic band dispersion of a finite structure.

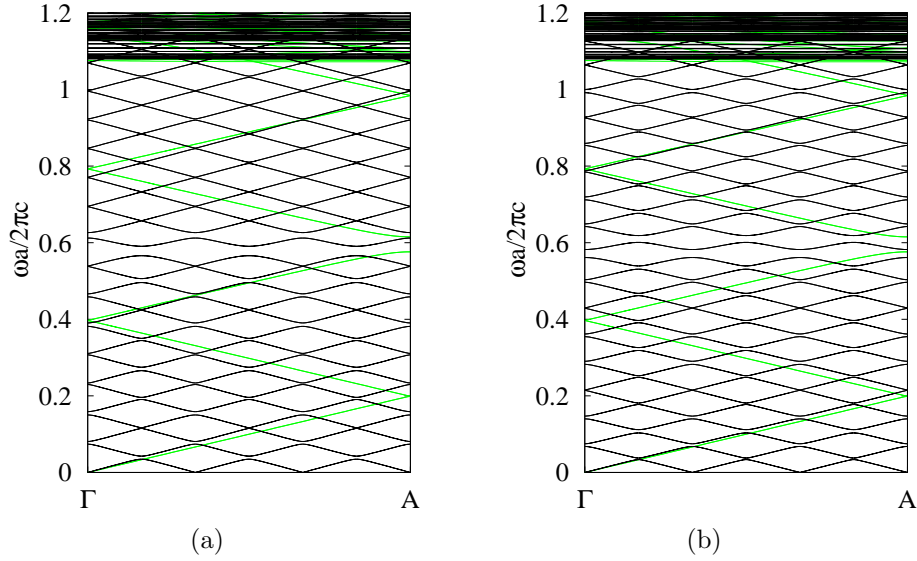In the low energy region the photonic band dispersion presents the usual

Figure 4.3: Band structure along ΓA obtained by plane-wave expansion method using a supercell representing a 5-layer opal (black line): (a) totally embedded in air and (b) lying on a glass substrate ($\varepsilon_{\mathrm{glass}} = 2.1$). The opal film is made of polystyrene spheres ($\varepsilon_{\mathrm{poly}} = 2.4964$) in air ($\varepsilon_{\mathrm{air}} = 1.0$). In green line band structure for the bulk structure are shown.

linear behaviour, proving that the interaction between the light and the crystal can be described by an effective medium approach. Small gaps, ascribable to the fictitious periodicity, open up at the edge of the Brillouin zone of the supercell lattice. The slope of the bands is different from those of the bulk PhC, because the average refractive index of the cell is smaller due to the presence of air: when the dielectric substrate is present the refractive index is closer to that of a bulk opal and the difference is reduced. Moreover it has to be noticed that for supercell data there is a photonic mode having a frequency within the stop band of the bulk opal: this state is a spurious effect closely related to the fictitious periodicity introduced by the supercell. In Chapt. 3 we already analysed the fact that in this low-energy region the increase in the number of layers leads the optical properties towards the infinite crystal behaviour. Therefore the main interest of the supercell method lies in the study of the optical features in the high-energy region, where out-of-plane diffraction plays a crucial role.

It is now necessary to establish how many air and glass layers are needed in order to really see finite-size effects in the photonic band structure. In Fig. 4.4 we present the calculations obtained by means of the asymmetric supercell varying the thickness of the air and of the substrate. As these results will be compared, in Chapt. 5, with optical spectra obtained with scattering matrix method and five-cylinders approximation, we use the same approximation in plane wave expansion. From the figure one can observe that the band corre-
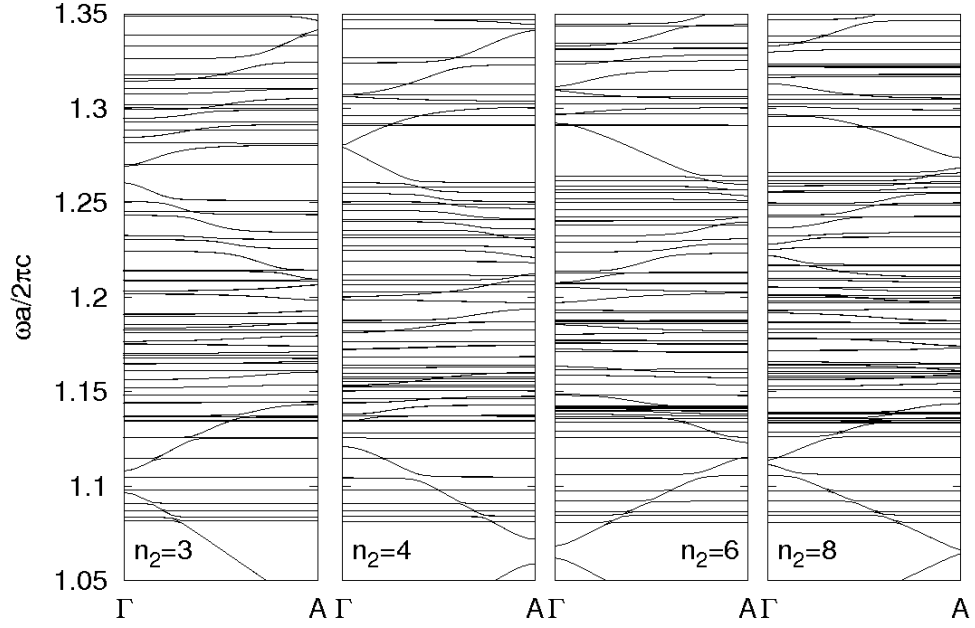
Figure 4.4: Photonic band structure calculations performed by means of an asymmetric supercell by varying the air and substrate thickness: from left to right n_2 assumes the values of 3, 4, 6, 8, respectively

sponding to transmitted beam is not really affected by the change of n_2, the number of air and substrate layers, apart from the fact that the filling fraction varies and thus also the average refractive index, resulting in a slight change of slope. This dispersive band couples in different ways with flat modes, so this can create some changes in crossing and anticrossing positions. The lower-energy states do not change very much from panel to panel, while the difference is remarkable at higher energies. In particular, when passing from 3 to 4 there is a sensitive change in position and dispersion of the modes at about 1.25 and 1.3 $\omega a/(2\pi c)$. When n_2 is greater than 4, the number of flat states seems to increase, but this is due only to a denser folding of the bands, as the Brillouin zone is smaller. Hence, for our purpose, we can conclude that at n_2 has to take at least the value of 4.

Let now discuss the features of band structure in this high-energy region, i.e. above the diffraction threshold. Above the reduced frequency of $\omega a/(2\pi c) = 1.0$, flat bands arise, responsible of diffraction states. This bands couples with the dispersive mode associated to transmission inside the crystal resulting in a number of crossings and anticrossings that strongly affect phase delay measurements in this high-energy region for thin film opal. In Sect. 5.2 we will analyse this particular phenomenon and we will present in detail a comparison between supercell calculation and phase delay results obtained by

scattering matrix method in the high-energy region.

4.2 Defect modes in direct opals

Just like doping in electronic semiconductors, designed defects in PhCs offer functionalities that are useful for integrated optics. Point defects can act as light traps or 3D cavities for low-threshold lasers. Line defects can potentially serve as optical waveguides, the basic building blocks of any planar integrated optical system. Finally planar defects can give rise to allowed photon states within the forbidden frequency range, similar to Fabry-Pérot microcavities.

The interesting role of intentional extrinsic defects in PhCs was known since the first works in this research field [1, 2], however only in the last few years this issue have been investigated also in self-assembled PhCs. The main reason for this delay is the high density of intrinsic defects, which are present in this kind of samples. Thus, before introducing new designed imperfections, the intrinsic disorder has to be eliminated or at least strongly reduced.

Fortunately, the development of the vertical deposition method, together with its subsequent improvements, gives the possibility to fabricate planar colloidal crystals with high optical quality, allowing control even on the crystal size. Thanks to this advantage, different techniques with the aim of introducing intentional defects in opals have been developed. Polymer defect lines in silica opals were first achieved using a multiphoton confocal laser [126]. Then different motives have been drawn or built within colloidal crystals by a wide variety of techniques including direct laser writing, electron beam lithography and photolithography [127, 128, 129, 130]. Planar defects can be included in opal PhCs employing different processes. A monolayer of spheres sandwiched between two opal films made of spheres of different diameter can be prepared by means of Langmuir-Blodgett technique [81, 80, 131]. Spheres and nanocrystal aggregates can be incorporated by spin-coating [78]. Furhermore, planar defects have been embedded in colloidal crystals by chemical vapor deposition [132, 133].

Facing all these experimental advances, from a theoretical point of view it would be useful to determine optical spectra and photonic band structure of 3D PhCs presenting controlled defects. Reliable calculations may allow the design of extrinsic defects, helping in guiding technological efforts. So far, optical spectra of opal films embedding a planar defect has been calculated by means of scalar wave method [77, 79].

The supercell scheme can be exploited to study the photonic band structure of an opal presenting point, line or planar defects. In this Section we present a method to determine band dispersion of a bulk opal embedding a layer of a dielectric medium.

The unit cell used to define the system in plane-wave expansion code is depicted in Fig. 4.2. The lattice vectors describing the system are exactly the
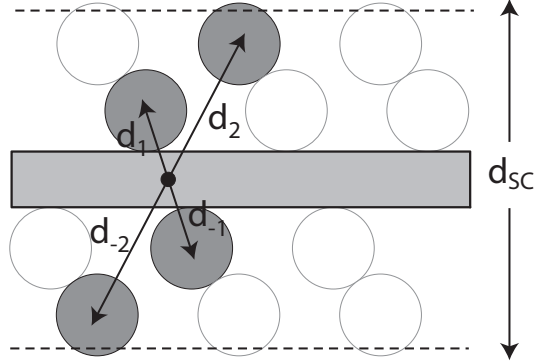
Figure 4.5: Supercell of a opal with a planar defect embedded. Characteristic lengths are indicated.

same of Eq. (4.1), as the in-plane pattern maintains its triangular periodicity. The structure can be described preserving inversion symmetry, if the origin of the unit cell is taken at the center of the defect. Hence an equal number of spheres n_1 is placed on both sides of a defect, having height h_{def}, according to the following definitions for the basis vectors:

$$\mathbf{d}_\nu = b \left(0, \frac{\pm\nu - 1/2}{\sqrt{3}}, (\pm\nu - 1/2)\sqrt{\frac{2}{3}} + (1 - \sqrt{\frac{2}{3}}) + \frac{h_{\text{def}}}{2b} \right) , \qquad (4.8)$$

where ν goes from 1 to N_1. The total height of the cell is thus:

$$h_{\text{SC}} = h_{\text{def}} + 2n_1 d_{111} + H_{\text{cap}} . \qquad (4.9)$$

Once again we recall that each sphere can be easily substituted by a proper number of cylindrical slices in case that the photonic results has to be strictly compared to spectra obtained by means of scattering matrix method, where the cylinder approximation is needed.

In order to prove the validity of our approach to study the photonic band dispersion of a bulk opal presenting a controlled planar defect, we studied the evolution of a defect state when the number of sphere layers in the supercell is increased. As an example we consider a defect of height $h_{\text{def}} = 0.3 d_{111}$ and having a dielectric function $\varepsilon_{\text{def}} = 2.56$. The thickness of the defect has been chosen in order to have a defect state inside the first pseudogap. Planar defects made of Titania nanocrystals, which presents a refractive index similar to that used in this example, have been recently embedded into polystyrene opals by spin-coating techniques [78] and their optical properties have been investigated by means of white light interferometry and a scalar wave approach [79].

In Fig. 4.6 we show the photonic band structure calculated by means of the supercell method varying the number of sphere layers n_1: from top left to bottom right, we consider $n_1 = 5, 10, 15, 20$, respectively. As in the previous
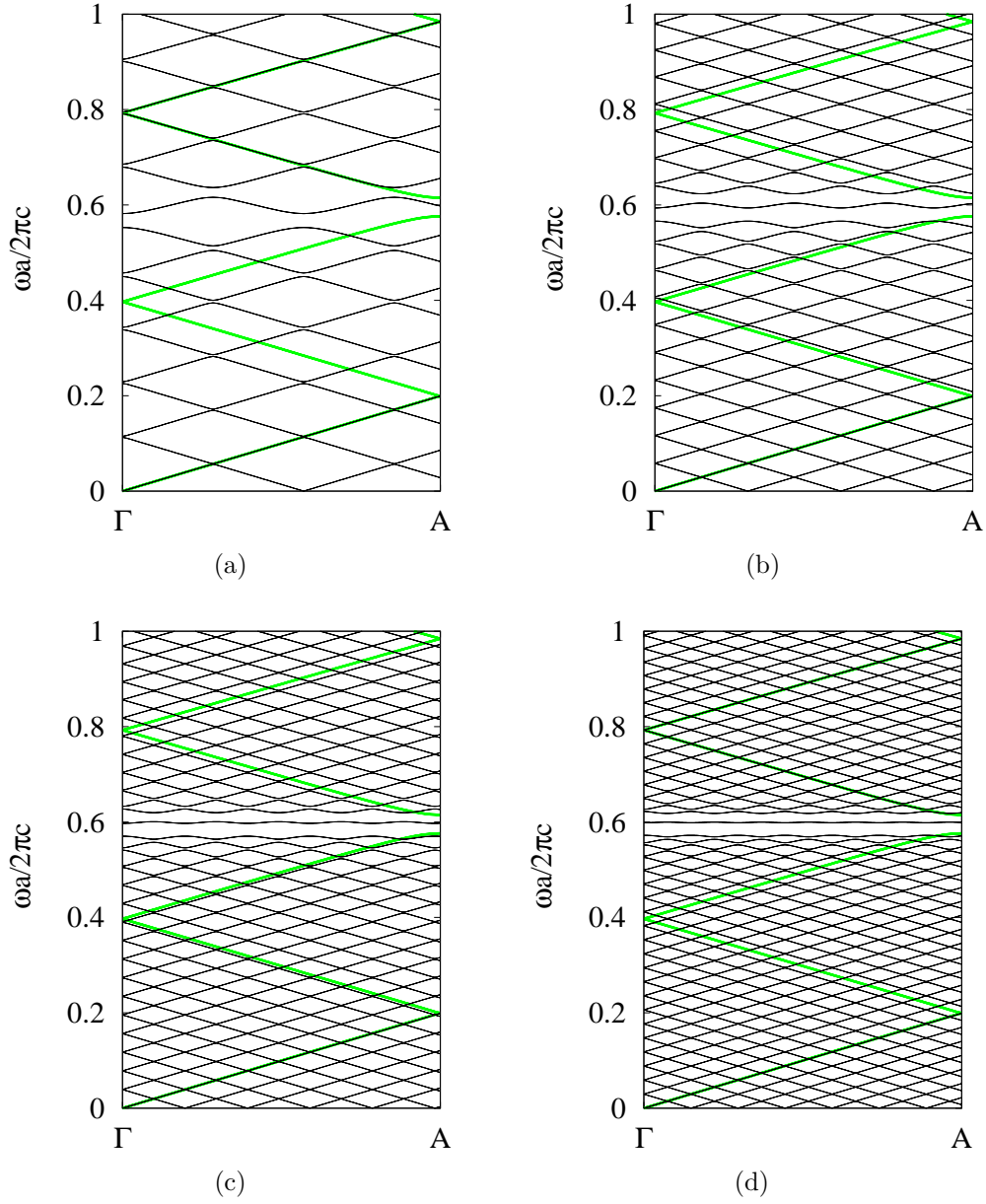
Figure 4.6: Photonic band structure along ΓA in the hexagonal Brillouin zone for an opal containing a planar defect of thickness $d = 0.3\, a/\sqrt{3}$ with (a) 10, (b) 20, (c) 30 and (d) 40 layers of spheres between two defects.

section we plot the dispersion in a extended cell scheme, along the ΓA direction of the Brillouin zone for the hexagonal lattice. The band structure of a bulk opal made of polystyrene spheres is plotted in green line for comparison. Once again, we remember that the supercell bands are folded six times due to the fact that the reciprocal lattice length along [100] direction of the hexagonal lattice becomes smaller for increasing number of layer.

In the first case, shown in Fig. 4.6(a), there are ten sphere layers between

two consecutive defects. In the photonic band dispersion we notice the presence of two dispersive bands, folded many times in these extended zone representation, that have the same slope as the dielectric and air bands of the bulk opal dispersion relation. Moreover, the position of the first pseudogap of the bare opal is closely matched by the band structure of the opal embedding a defect. The main difference is represented by the presence of a photonic mode inside the stop band for the latter band dispersion, that can be associated to the presence of the planar defect. On one hand the dispersion of the air an dielectric bands do not change significantly by varying the number of sphere layers n_1 of the supercell, at least resulting in a variation of the band edge position towards a perfect matching with bulk stop band. On the other hand, the photonic state associated to the planar defect becomes flatter and flatter with the increasing of the sphere number n_1. This means that in the situation depicted in Fig. 4.6(a) n_1 is too small to prevent interaction between two consecutive defects in the supercell lattice and a spurious effect due to delocalization of the mode is present. At the same time, the flat band in Fig. 4.6(d) prove that the defect state is perfectly localized inside the crystal, avoiding any spurious effect. This evolution shown in the four panels of the figure guarantees the validity of this supercell approach, provided a proper choice of the supercell parameters is made.

Chapter 5

Diffraction in opals

In this chapter we will analyse the role of diffraction in opal-based photonic crystals (PhCs). The first two sections deal with the dependence of diffraction and transmission features on sample thickness. The Pendellösung effect is a mutual interchange of energy between transmitted and diffracted beam and it takes place above the diffraction threshold. In the same energy region, when a dip in transmission occurs, for instance in the second order stop band, a change from slow to superluminal behaviour can be observed varying the number of layers. This will be the subject of Sect. 5.2. Finally, the study of optical properties of a sample whose growth is oriented along [100] direction will be presented: it can be seen that the spectra are strongly influenced by the presence of diffraction.

5.1   Pendellösung Effect

When the wavelength of the light impinging on the medium is nearly the same as the lattice constant, diffraction effects may occur. In the band structure this is viewed by low dispersive bands. This high-energy region has been scarcely studied because it is very difficult to grow samples with a high enough quality to measure these effects. As we saw in Chapt. 3, a low dispersive band is related to a slow group velocity and hence to a pronounced light-matter interaction which boosts the effect of disorder. Nevertheless the phenomena related to diffraction are very appealing, and up to now not completely understood.

A starting point to analyse diffraction effects in opal PhCs is to study the dependence of diffraction intensity as a function of sample thickness, i.e. of the layer number N. In Fig. 5.1(a) the diffraction intensity in the high-energy region is shown as a contour plot for N ranging from 1 to 40. These results have been obtained by means of the scattering matrix method, exploiting the five-cylinder approximation: as we did not deal with absorbing media, we consider diffraction as $D = 1 - R - T$, where R and T are, respectively, reflectance and transmittance. Nearly periodic oscillations can be noticed at
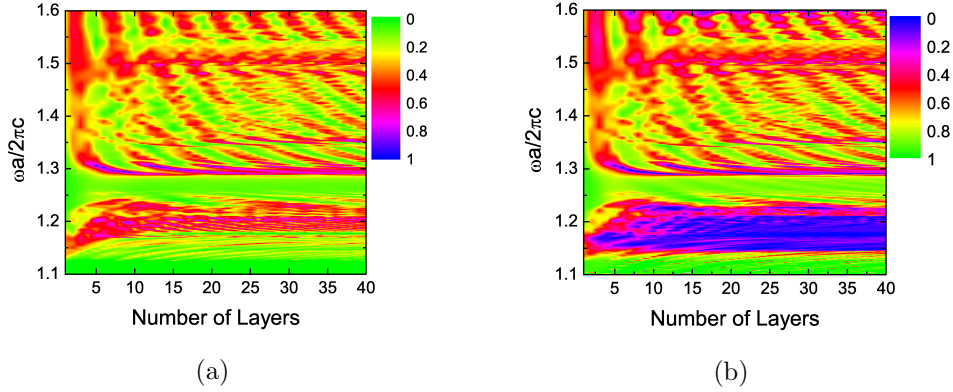
Figure 5.1: (a) Diffraction and (b) transmission intensity in the high-energy region for a polystyrene opal as a function of frequency and number of layers.

specific frequencies: they are an evidence of a mutual exchange of energy between two or more beams inside the crystals. This effect is analogous to the well known "Pendellösung" phenomenon, that has been extensively studied for X-ray or neutron diffraction in ordinary crystals [134, 135, 136]. The same phenomenon has been recently studied in 2D PhCs [137] as an effect related to negative refraction. Figure 5.1(a) shows that the Pendellösung effect is also present for 3D PhCs in the energy region above the diffraction cutoff, which, for the sample under consideration grown on a glass substrate, takes place at about $1.1\omega a/(2\pi c)$). As written in Chapt. 3, transmission measurements are very sensitive to diffraction features, so in Fig. 5.1(b) we show a contour plot of transmission intensity, reversing the color scale with respect to Fig. 5.1(a). The behaviour is basically the same, apart from some differences that should be present, as reflection does not vanish in this region.

From the two contour plots shown in Fig. 5.1 it can be noticed that the oscillation period varies with respect to the frequency. In order to understand this feature more clearly, we plot in Fig. 5.2(a) the diffracted intensity as a function of N for two specific reduced frequencies. Considering N as a continuous variable, the period of oscillations is close to $\Delta N = 6.6$ for $\omega a/(2\pi c) = 1.33$ and $\Delta N = 8.7$ for $\omega a/(2\pi c) = 1.30$. Furthermore, it can be noticed that the Pendellösung oscillations for $\omega a/(2\pi c) = 1.30$ are damped. It is interesting to relate these features to the photonic band structure. Figure 5.2(b) shows the photonic bands that are allowed or forbidden for light coupling, due to symmetry reasons [125]. Only coupled bands are responsible for light propagation and for diffraction effects along this specific direction. In order to give a quantitative description of the Pendellösung phenomenon, we notice that for $\omega a/(2\pi c) = 1.33$ and $\omega a/(2\pi c) = 1.30$ only two photonic modes are allowed in the crystal. In this case the period Λ_{Pend} of the oscillation of the diffraction intensity is inversely proportional to the difference between the two relevant
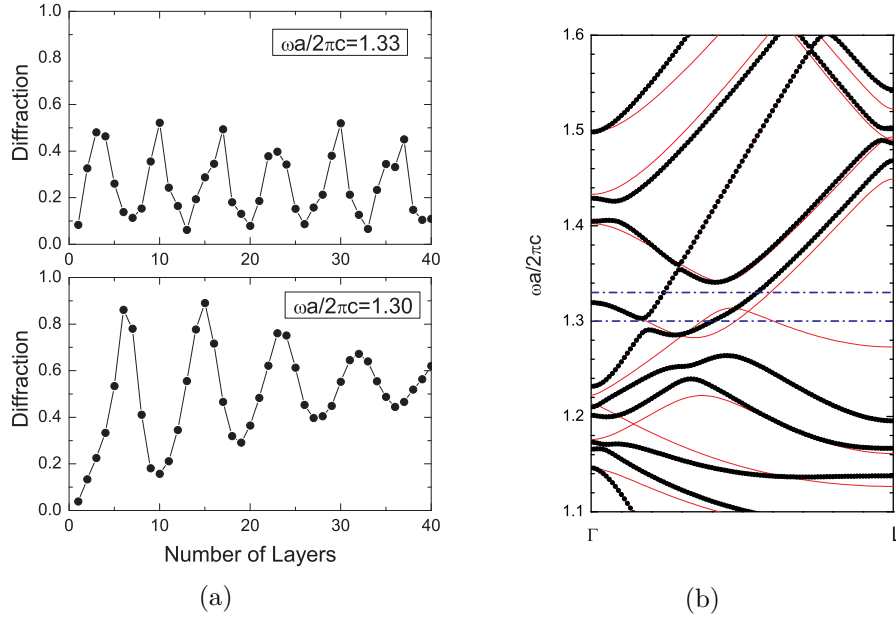
66

Figure 5.2: (a) Diffraction intensity as a function of the number of layers for two different frequencies: $\omega a/(2\pi c) = 1.33$ and $\omega a/(2\pi c) = 1.30$, indicated in the inset. (b) Photonic band structure along ΓL. Dots: bands that couple to incident light and are responsible for periodicity of the diffracted intensity; thin solid lines: uncoupled bands. The horizontal dashed-dotted lines indicate the frequencies indicated in the left panel.

wavevectors:

$$\Lambda_{\text{Pend}} = \frac{2\pi}{\Delta k}, \tag{5.1}$$

where $\Delta k = k_2 - k_1$. For the case of $\omega a/(2\pi c) = 1.33$, shown in the upper panel of Fig. 5.2(a), we get $\Delta k = 0.31 \cdot \sqrt{3}\pi/a = 0.97 d_{111}$ which gives $\Lambda_{\text{Pend}} = 6.5 d_{111}$, in agreement with the above value of ΔN. For the case illustrated in the lower panel of Fig. 5.2(a), namely $\omega a/(2\pi c) = 1.30$, we get $\Delta k = 0.24 \cdot \sqrt{3}\pi/a = 0.75 d_{111}$, whence $\Lambda_{\text{Pend}} = 8.4 d_{111}$ which also agrees with the period ΔN determined from the figure. Thus we conclude that the Pendellösung oscillations originate from spatial beatings between the fundamental propagating mode along the [111] direction and a diffracted mode.

It is interesting to notice that the frequency $\omega a/(2\pi c) = 1.30$ is slightly below a minimum of the allowed mode at $k = 0.17\sqrt{3}\pi/a$ in Fig. 5.2(b). Thus a single mode at $k = 0.17\sqrt{3}\pi/a$ is excited, but with a small imaginary part of the wavevector, leading to a damping of the Pendellösung oscillations as observed in the bottom panel of Fig. 5.2(a). Moreover, when more than two wavevectors are allowed for light coupling the situation is much more complicated. In this case the exchange of energy is among three or more states and it may not result in periodic oscillations when the beating periods are incommensurate. Examples of this situation can also be recognized in Fig. 5.1.
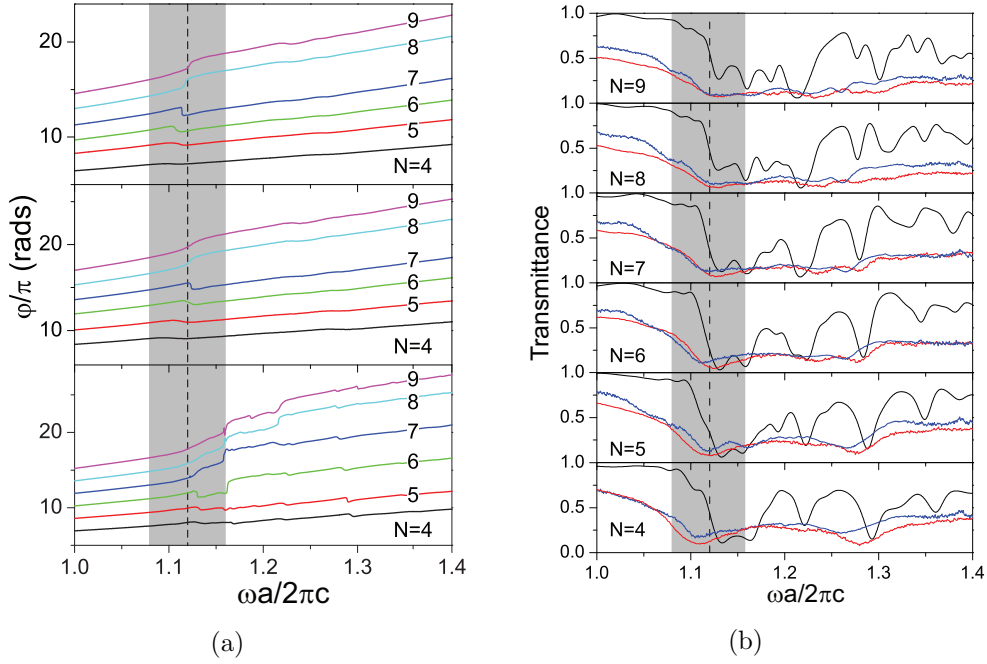
Figure 5.3: (a) Phase delay dependence on reduced frequency (from top panel to bottom panel) measured for the $505nm$ sphere sample, for the $705nm$ sphere sample, and calculated by means of scattering matrix method. The region wherein the phase flip take place is highlighted with a grey box. (b) Transmission spectra: in blue line those measured for sample B, in red line measured for sample A and in black line the theoretical results. In both figures results for increasing layer number, indicated by N are presented.

5.2 Slow to superluminal behaviour

The subject of slow and superluminal propagation of light in a medium obtained a growing interest in the last century. After the theoretical prediction, a number of experimental measurements of group velocity lying either below or well above the causal limit of c, the light velocity in vacuum, have been performed. An impressive issue of superluminal propagation occurs when the group velocity of light in a medium is negative, appearing as if the pulse exits the medium before even entering it. As a matter of fact, before the peak of the incoming pulse enters the medium, the peak of the outgoing pulse is already exiting it and a third pulse propagates effectively with a negative group velocity inside the medium. All these features originate in a rephrasing process caused by the negative refraction present inside the medium [138].

The two samples that have been measured for the present work and named hereafter as sample A and B are made of polystyrene spheres with diameters equal to, respectively, 705nm and 505 nm [139]. Samples have been grown on a glass substrate and present (111) planes parallel to the surface with control over the layer number [104]. The experimental set-up allows to retrieve the
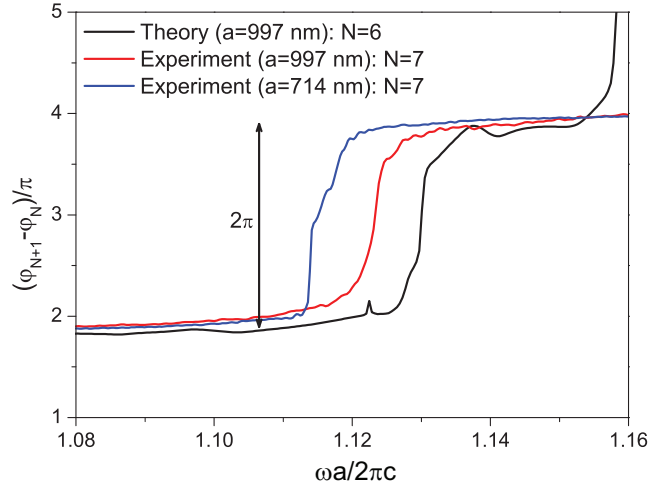
Figure 5.4: Difference between the absolute phase delay for two sample thickness, before and after the phase flip has taken place.

intensity of both the phase delay and the transmitted beam, by means of white light interferometry [122]. The absolute phase was obtained theoretically with the method explained in Chapt. 3.

In Fig. 5.3(a) measured and calculated phase delay curves are shown with respect to the reduced frequency $\omega a/(2\pi c)$, to point out the scalability of the phenomenon. The two upper panels present results for samples A and B, measured for increasing thickness, going from 4 up to 9 layers. The calculated spectra, shown in the bottom panel, are obtained by means of the scattering matrix method, for the same thickness as in the experiment. In Fig. 5.3(b) transmission spectra obtained with the same parameters of Fig. 5.3(a) are shown. In order to better fit the experimental results, we introduced a dispersive dielectric function, derived from phenomenological data, and we took into account a small relaxation. The model is similar to that used in Sect. 3.1: we consider an in-plane lattice constant $b = 730nm$, while along the vertical direction the distance between two consecutive layer is still $d_{111} = d\sqrt{(2/3)}$ where d is the sphere diameter, as in the face centered cubic (fcc) case. As written before, this is consistent with the polydispersity in sphere diameters. In normalizing the results shown in Fig. 5.3(a) we take a equal to $d\sqrt{2}$, skipping the difference of the in-plane lattice constant. The good correspondence between theory and experiment further corroborates the approximation employed in Chapt. 3 to fit the data in the low-energy region. Introducing an in-plane relaxation strongly influences diffraction spectra as the onset of diffraction is dictated by the 2D periodicity present in the (111) planes.

The theoretical results are in good agreement with experimental measurements. From Fig. 5.4 it can be seen that the phase delay grows linearly, apart from a jump at about $1.12\omega a/(2\pi c)$. This jump becomes better defined with increasing number of layers, it changes its sign and eventually becomes again
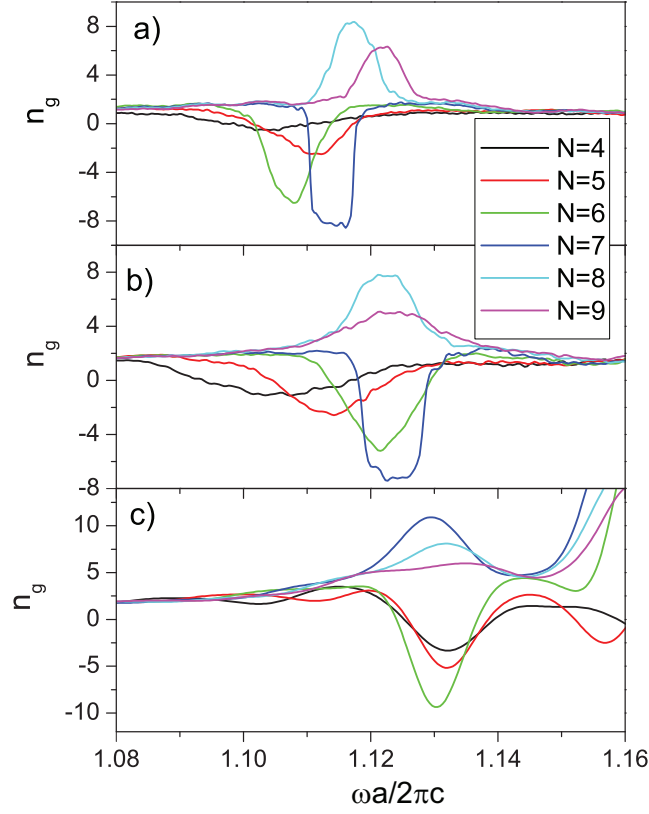
Figure 5.5: Group index derived by phase delay according to Eq. (5.2). Results are presented for samples A and B and for scattering matrix calculations assuming a dispersive dielectric function for polystyrene and an in-plane relaxation.

less defined. Figure 5.4 shows the difference between the phase delay of the two consecutive opal thickness for which the flip in sign takes place: the latter is clearly equal to 2π.

Results for the group velocity are presented in Fig. 5.5. The group index n_g has been derived from measurements on sample A and B, from 4 up to 9 sphere layers and from the theoretical phase delay shown in Fig. 5.3(a), with in-plane relaxation and dispersive dielectric function, according to the following relationship:

$$n_g = \frac{c}{v_g} = \frac{c}{D}\frac{d\varphi}{d\omega}. \tag{5.2}$$

The effect of the small jump in phase delay is now clearly visible. The group index has a peak, corresponding to the phase jump at about $1.12\omega a/(2\pi c)$. For the smallest number of layers there is a small dip that assumes negative values. Increasing the layer number the peak becomes narrower, according to the more defined jump in phase delay, and reaches a negative maximum. For the specific number of layers at which the sign flip occurs in the phase, the group index also changes its sign, becoming large and positive in the surroundings of $1.12\omega a/(2\pi c)$. Increasing once again the number of layer the peak remains
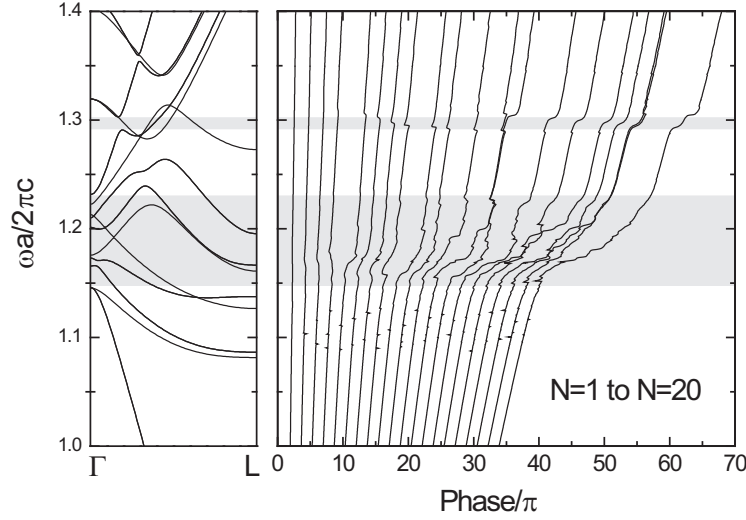
70

Figure 5.6: Left panel: photonic band dispersion of a bulk opal made of polystyrene spheres (refractive index $n = 1.59$), calculated along ΓL direction. Right panel show the calculated phase delay for samples having from 1 up to 20 layers. Gray boxes highlights the spectral region where only diffraction bands are present in band structure.

positive, but becomes less defined, in accordance with phase delay curves. This behaviour corresponds to a transition from negative values, indicating a strong superluminal propagation, to small but positive values, i.e. the so-called slow-light phenomenon (when the group velocity lies below c), and finally to large and positive values, i.e. reaching superluminal values, only by varying sample thickness. The superluminal and even negative propagation does not violate causality principle because it occurs in a region of strong extinction where the transmission is highly reduced in the sample, as can be seen in Fig. 5.3(b). Moreover the fact that light is transmitted through the opal, due to the finite size, ensures that the definition of phase delay and group index are fully valid.

A small discrepancy between theory and experiment is now evident: on the one hand in the measured phase the flip occurs when passing from 7 and 8 layers in both samples; on the other hand in the theoretical results it takes place between 6 and 7 layers. This can be ascribed partly to the five-cylinder approximation, that can miss some points in representing the actual symmetry of the sample, but may be also due to the unavoidable degree of disorder present in real samples. The latter may lead to a smoothening in the experimental curves, but can also lead to a slight relaxation that can modify finite size effects. This hypothesis is supported by the fact that in calculating the phase delay for the structure without relaxation and assuming a dielectric constant for polystyrene $\varepsilon_{\mathrm{poly}} = 2.4964$, results shown in Fig. 5.6 together with band dispersion for the infinite system, the flip is still present but it occurs between 4 and 5 layers and its energy is blue-shifted. In both experiments the flip
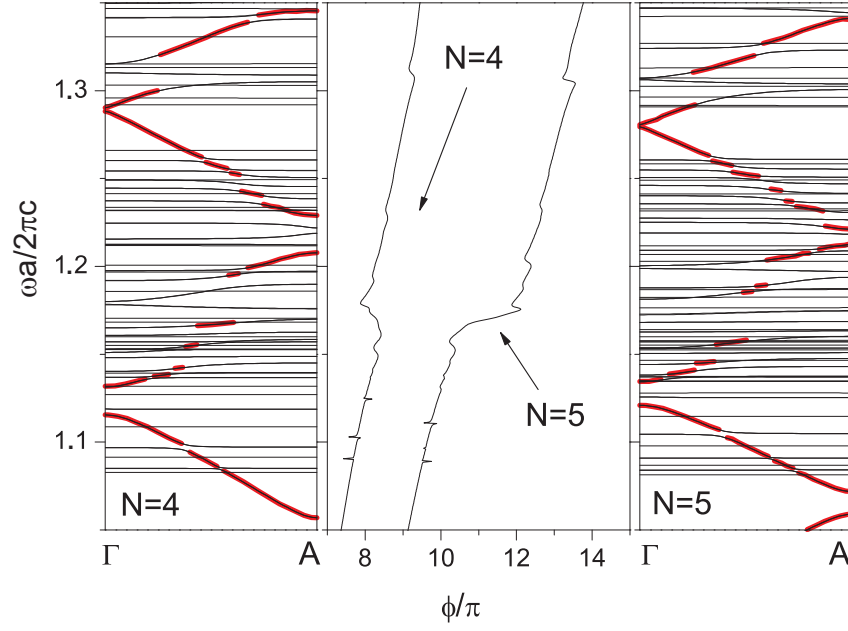
Figure 5.7: In the left and right panels supercell calculations performed for samples having 4 and 5 layers are shown. In the middle panel calculated phase delay for samples of the same thickness.

shows a perfect scalability, hence one can guess that a systematic structural modification of the fcc lattice, due to the growth process, occurs. Furthermore in theoretical results many of these flips are observed. In particular, in Fig. 5.6 we highlighted in grey boxes two regions wherein the transmitted beam is absent in the bulk sample: the first one corresponds to the second order band, while the second one to an anticrossing between the dispersive band associated to transmission and a flat band arising from out-of-plane diffraction. In these frequency ranges there are several anomalous features in phase curves, supporting the hypothesis that the superluminal or slow light behaviour of the system is definitely due to higher order diffraction.

The phenomenon can be ascribed to the finite-size in the vertical direction of the samples. To prove this we calculated the band structure of a finite size system by implementing a supercell in plane-wave expansion method, as described in Chapt. 4. It is well known that supercell calculations take into account surface states, as proved in the previous chapter, so this method is the most suitable to study the band structure of the finite systems. The supercell is asymmetric, as the opal is surrounded by 4 equivalent layers of air on one side and the same thickness of glass on the other side. Results for these calculations are presented in the left and right panels of Fig. 5.7, while in the middle a close view of the phase delay shown in Fig. 5.6 for 4 and 5 layer samples is shown. It is now evident that phase anomalies, leading to superluminal values of group velocity, are associated with region wherein only diffraction, indicated by the flat bands in the frequency dispersion, is present and it is clearly ascribed to

the 3D periodicity. Besides the 2π flip between the two phase curves, other phase jumps appear whenever an anticrossing or a stop band occurs in the photonic band structure.

It is worth mentioning here that this anomalous propagation behaviour with phase flips and the Pendellösung effect do not occur simultaneously. The latter, in fact, is closely related to the presence of the transmitted beam inside the sample, while the former is related only to out of plane diffraction and it occurs in the region of the second order stop band or in correspondence to anticrossings.

5.3 Optical properties along ΓX direction

We have hitherto analysed the optical properties along ΓL direction and its surroundings, as these are the directions commonly investigated in experiments such as reflectance and transmittance measurements. This is due to the fact that opals grow preferably with (111) lattice planes parallel to the surface and even at high-incidence angle it is impossible to probe directions such as the $\langle 100 \rangle$. Studying the optical properties along directions other than those commonly investigated may be interesting for basic knowledge, but it may also be useful for practical purposes, such as optical device realization.

Samples oriented along different crystallographic directions may be difficult or expensive to produce, nevertheless they can be obtained by a variety of techniques. Firstly they can be grown on an suitably patterned substrate [69, 140, 141], resulting in high-quality but rather costly samples. Furthermore they can be obtained by cleaving already grown opals [142] or employing spin coating techniques [71]. Even when developing samples by vertical deposition method, small regions presenting square faces parallel to the surface, and consequently oriented along [100] direction, can be found.

This optical study has been done on a sample grown by vertical deposition presenting a hundred of microns wide area where the [100] lattice planes are parallel to the surface, as shown in Fig. 5.8. The region under study was made by 7 layer of polystyrene spheres in air, lying on glass substrate, with a diameter of about 505 nm. The optical measurements were collected by means of a micro-reflectometer in a wide spectral range, from 0.4 up to 3.1eV.

Reflectance and transmission measurements have been done for two different sample orientations for an incidence angle going from nearly 0 to 70 degrees in steps of 5 degrees. As the [100] planes present a square lattice, the two possible orientation are the one following a square diagonal and the one parallel to a square edge. The main results are also presented in Ref. [143].

To better understand the experimental measurements, we performed photonic band dispersion calculations of a bulk opal made of polystyrene spheres ($\varepsilon_{\mathrm{poly}} = 2.53$) in air.
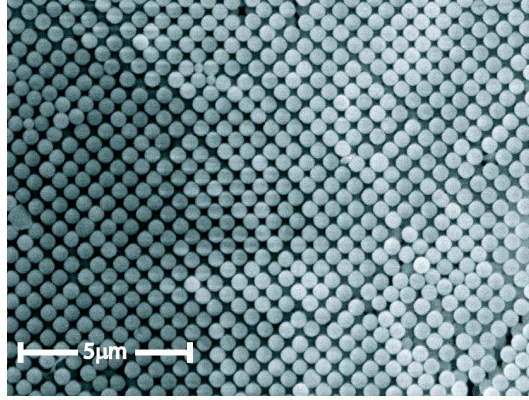
73

Figure 5.8: Scanning electron microscope (SEM) image of the surface of an opal whose horizontal layers are defined as (100) planes. (Courtesy of Dr. Galisteo-López).

First of all we compare the band dispersion calculated along ΓX, that is the direction described by a reciprocal vector perpendicular to (100) planes, to reflectance and transmittance spectra, obtained for an finite incidence angle of 3 degrees, near to normal incidence. These results are presented in Fig. 5.9.

For reduced frequency below 0.9 the photonic band dispersion is analogous to that of a transparent medium: it shows only the free-photon like bands folded at the edge of the Brillouin zone, as we can see from Fig. 5.9. Contrarily to other directions, such as the ΓL one, there is no pseudo gap at the X point. It has been demonstrated [144] that this gap can be tuned in artificial opals by varying the index contrast and we have seen in Sect. 2.4 that it opens up when we break the spherical symmetry by substituting each spheres with one or three cylinders. The absence of a Bragg peak, associated to a possible pseudo gap, it is noticed also in transmittance and reflectance spectra. In this low-energy region the former is quite high, while the latter shows the characteristic Fabry-Pérot oscillation, due to interference between the beams reflected at the air and substrate interfaces of the sample. The two spectra confirm the behaviour of the sample as a transparent medium.

Above the energy of $0.9\omega a/(2\pi c)$, where the wavelength of light is nearly the same as the lattice constant, diffraction effects come into play. The band structure presents a number of low-dispersion bands that can be ascribed to diffraction from other crystallographic planes. In this region reflectance shows peaks that are no more associated with Fabry-Pérot oscillations, while the transmittance drops abruptly, presenting two strong dips in correspondence of flat bands in the photonic frequency dispersion. Light is no more reflected nor transmitted through the crystal, but it is diffracted in other directions, according to the symmetry of the structure. Diffraction structures are more visible in transmission spectra, as mentioned in Sect. 3.2, therefore the latter is more suitable to characterize samples oriented along [100], where the optical properties are strongly affected by diffraction bands.
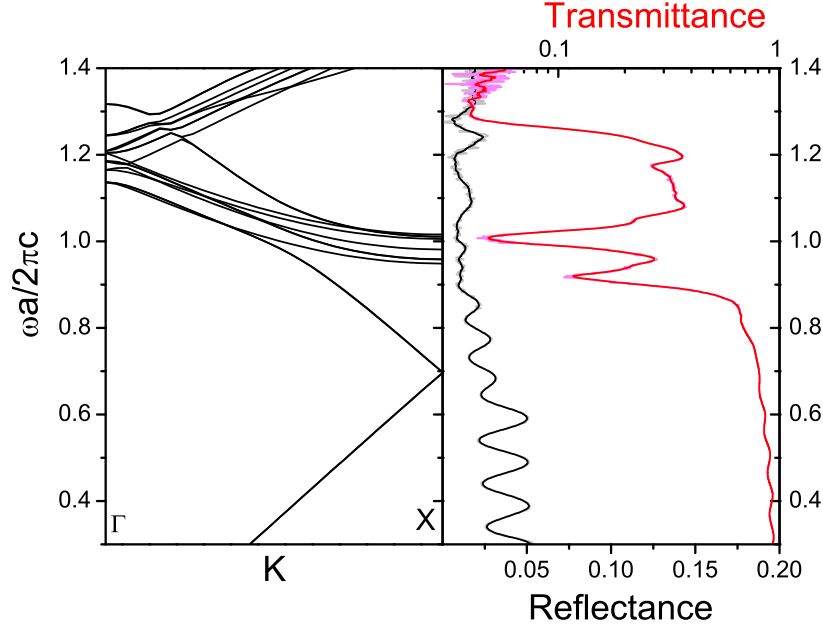
Figure 5.9: Left panel: photonic band structure of a bulk opal, made of polystyrene spheres in air along the ΓX direction in the first Brillouin zone. Right panel: reflectance (black line) and transmittance (red line) spectra of a 7-layer sample measured for an incidence angle of 3 degrees. The opal has the [100] planes parallel to the surface.

Subsequently angle resolved transmission measurements for two different sample orientations have been interpreted by means of band structure calculations performed along two proper lines in reciprocal space.

In Fig. 5.10 band dispersion calculated along the line XUU' are presented. The coordinates of points involved in calculations are the followings:

$$X = \frac{2\pi}{a}(0, 0, 1),$$
$$U = \frac{2\pi}{a}(1/4, 1/4, 1),$$
$$U' = \frac{2\pi}{a}(3/4, 3/4, 1).$$

(5.3)

The U' point is chosen in such a way that it lies on XU line and the distance $\overline{UU'}$ is double with respect to $\overline{XU}$. In this way we can obtain results for all the incidence angles probed experimentally even in the high-energy region. A similar work has been done for the other orientation investigated in the experiment, shown in Fig. 5.11. The broken line now is given by the following points:

$$X = \frac{2\pi}{a}(0, 0, 1),$$
$$W = \frac{2\pi}{a}(1/2, 0, 1),$$
$$W' = \frac{2\pi}{a}(3/4, 3/4, 1).$$

(5.4)

75

Figure 5.10: Band structure calculation along the XUU' direction in the first Brillouin zone, indicated in the drawing on the right, of an fcc lattice.

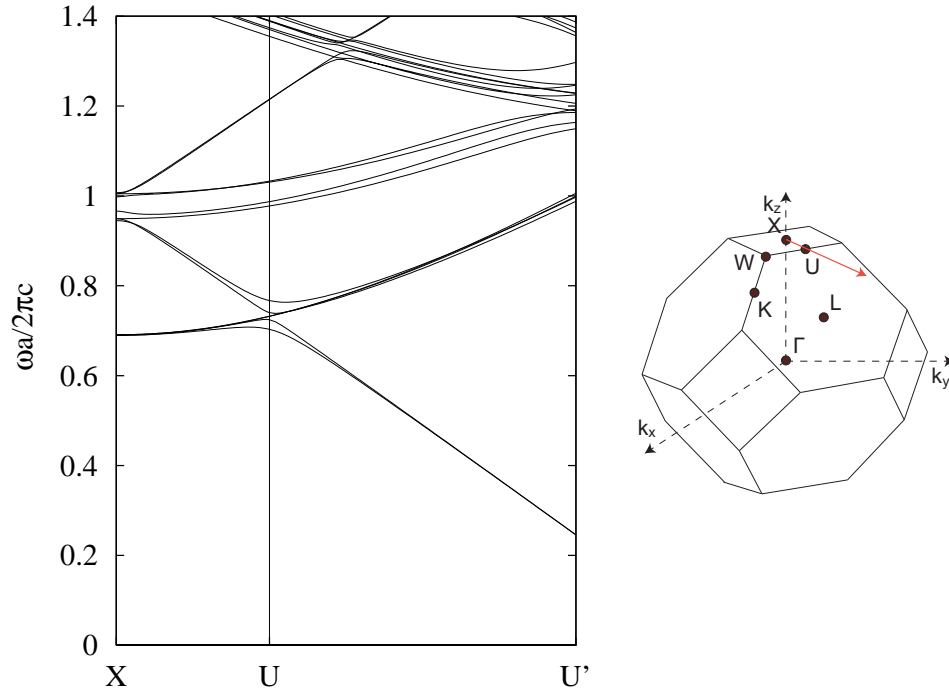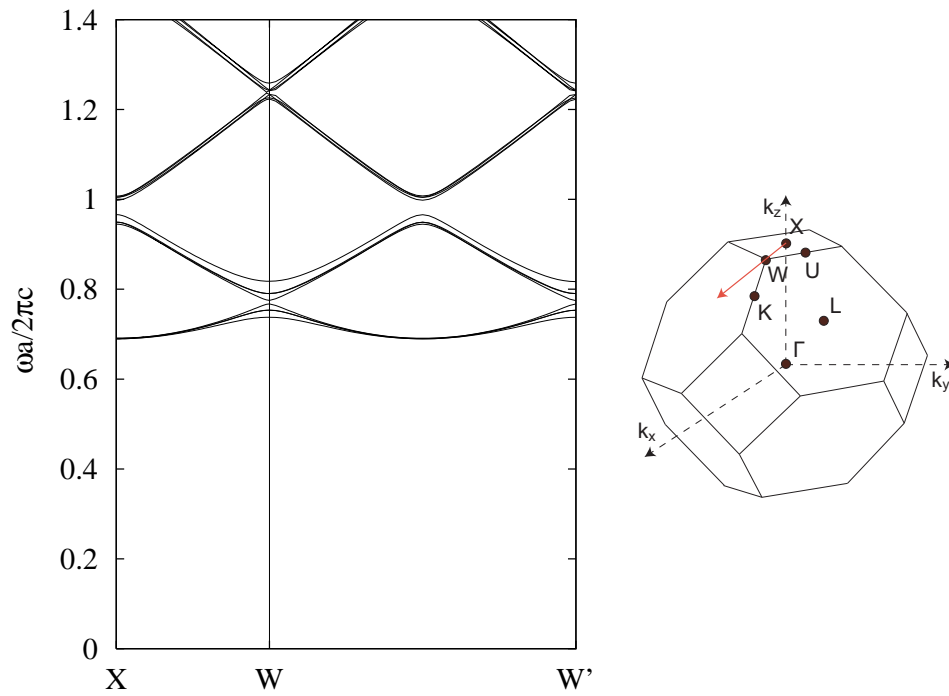Figure 5.11: Band structure calculation along the XWW' direction in the first Brillouin zone, indicated in the drawing on the right, of an fcc lattice.
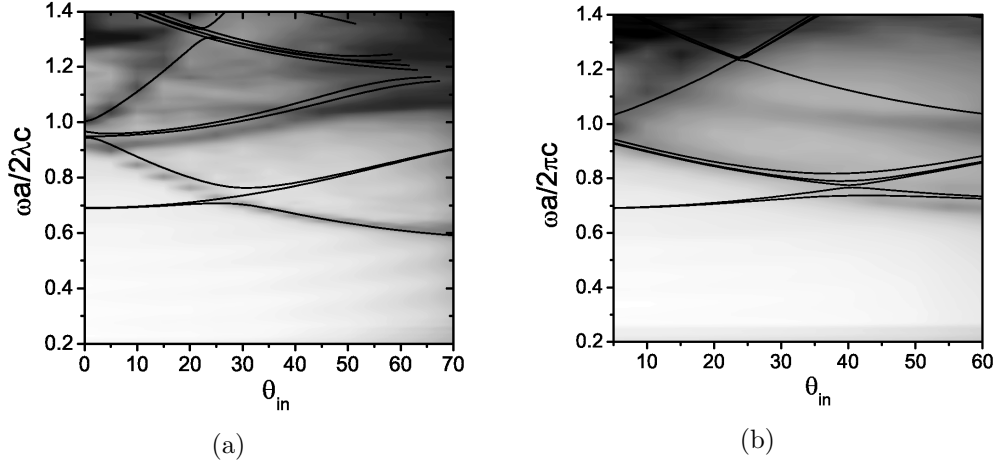
(a)   (b)

Figure 5.12: Contour plots of experimental transmittance spectra with respect to incidence angle. Spectra are taken varying the incidence angle in a plane parallel (a) to the edge of a square face and (b) to the square diagonal.

Experimental transmission spectra are presented in Fig. 5.12 in a contour plot form to appreciate the dispersion with respect to the incidence angle. The spectra have been taken for s-polarization and for an incidence angle going from nearly normal incidence to 70 degrees in step of 5 degrees. Superimposed in the same figure, the photonic band structures with respect to the incidence angle θ_{in} are plotted. Since the two planes ΓXU and ΓXW represent symmetry planes for the fcc Brillouin zone and it is possible to define symmetric and antisymmetric modes for the bands along the direction previously described, we represent on the countour plot only the modes with the right parity with respect to light polarization. The incidence angle is retrieved from the wavevector $\mathbf{k}$ in reciprocal space by the following relationship, remembering that the in-plane momentum $\mathbf{k}_\parallel$ is preserved at the interface between air and sample:

$$\theta_{in} = \arcsin\left[\frac{c}{\omega}|\mathbf{k} - \mathbf{k}_{\Gamma X}|\right], \tag{5.5}$$

where c is the speed of light in vacuum, ω the frequency of incident light and $k_{\Gamma X}$ the component of the wavevector $\mathbf{k}$ inside the crystal along the vertical direction.

Starting from Fig. 5.12(a), the transmittance for s-polarization along XU direction, i.e. parallel to square edge, is presented. There are features appearing in the optical spectra that closely match the dispersion of the photonic bands. In particular, in the spectral region below $\omega a/(2\pi c) = 1.0$ pronounced dips in transmission follow the dispersion of two set of bands. On the other hand, the set of bands at higher frequencies have just a weak correspondence in the contour plot and the experimental features do not match so accurately the dispersion of the photonic bands. The same situation is highlighted in

77

Fig. 5.12(b), where the optical measurements are taken along XW direction, i.e. parallel to the square edge in the direct lattice. A possible reason for this discrepancy may be the finite size of the samples. Furthermore, it is worth noticing that the above comparison is not completely correct. As a matter of fact, when measuring transmission the optical response of the sample is dictated for every single frequency, by the light dispersion along a certain vector in reciprocal space and not only by the bands on the surface of Brillouin zone. Therefore some differences should be expected in the high-energy range. Nevertheless the analysis presented in this Section gives useful information on the nature of the transmission dips, that arise from flat bands and are related to diffraction along other directions than the [100].

Conclusions and future perspectives

In this thesis work a theoretical approach to study the optical properties of self-assembled colloidal crystals has been proposed. By means of this model an extensive analysis of such photonic materials has been presented, besides experimental measurements which demonstrate several phenomena of interest and account for the validity of the method.

The theoretical approximation, together with a short overview on the numerical methods employed in the work, has been presented in Chapt. 2. The opal structure is a face centered cubic (fcc) lattice of dielectric spheres embedded in air. The samples grown by self-assembly are usually oriented with the [111] direction perpendicular to the substrate, hence they can be described as a stacking of hexagonal planes properly shifted with respect to one another.

The scattering matrix has proven to be a reliable method to calculate zero order transmission and reflection of a patterned multilayer. A staircase approximation, that consists in subdividing each spheres of the opal structure by a set of cylindrical slices along the direction perpendicular to the sample surface, allowed us to implement the crystal structure in the transfer matrix code. Meanwhile the plane wave expansion is a well-established method to derive photonic band dispersion of the actual opal structure, but also of the approximate one, therefore it can be used to optimize the cylinder parameters. Different degrees of approximation have been tested. Starting from a single cylindrical slice, an approach which gives good results at normal incidence in the region of the first pseudogap, we found surprisingly accurate results slicing the sphere in five cylinders and, most of all, taking into consideration the region wherein two consecutive planes overlap. By describing this interpenetration region of the real structure, our approach accounts well for out-of-plane diffraction and thus it is suited to investigate optical properties even far from normal incidence and even in the high-energy region, when the light wavelength involved is of the order of the lattice constant.

Exploiting our theoretical model we investigate the optical behaviour of opal samples for light impinging at normal incidence and having a frequency corresponding to the region of the first pseudogap in the L point of fcc Brillouin zone and its surroundings. In particular our attention was focused on the evolution towards infinite crystal behaviour and to the dynamics of light propagation inside the crystal considering samples of different thickness. From the calculated transmittance and phase delay we derived the group velocity and the effective refractive index of the opal film and we compared all these quantities to experimental measurements. Finally we pointed out the presence of a region of slow light at the band edges of the Bragg peak and a superluminal behaviour inside the gap, coexisting with strong extinction. An important role is played by structural disorder that affects experimental measurements.

Moreover we investigated theoretically the transmission and reflection spectra for light impinging on sample surface with a finite incidence angle in a plane parallel to a hexagon face diagonal, i.e. LW direction in Brillouin zone. Here we showed the existence of diffraction peaks related to low-dispersion modes in the photonic band structure and the presence of a mixing between TE and TM polarization. Since the ΓLW plane does not represent a symmetry plane for the first Brillouin zone it is impossible to classify the photonic modes by parity: when the incoming light couples with these modes, it loses its well-defined polarization and the outgoing light results in a superposition of TE and TM modes. On the other hand, the spectra obtained for an incidence plane that is rotated by $\pi/6$ with respect to the previous one, i.e. probing ΓLU and ΓLK plane in reciprocal lattice, evidence a threefold symmetry axis for the sample surface, corresponding to the symmetry point group at the L point. Only transmittance point out the difference between the two orientation, that seems to be equivalent in reflection.

In Chapt. 4 a supercell approach is employed to study finite-size effects or defect states. The possibility of calculating the band structure of a bulk opal presenting a planar defect may reveal itself as an effective manner to design controlled imperfection and to understand the physics that lies beneath the light localization by such defects.

By calculating the photonic band structure of a lattice whose primitive cell is the finite system, embedded in air or in a dielectric medium, that we want to study, we can identify those features which are typical of a structure having a finite number of layers and which can be very different from those of a bulk crystal. These features strongly affect the optical properties above the diffraction threshold, as discussed in Chapt. 5. Firstly, we demonstrated a periodic behaviour of diffraction and transmission with respect to the crystal thickness. When two or more modes, one being that associated with transmitted beam, are allowed for light propagation inside the opal there is a mutual exchange of energy between the states; depending on the number of layers, the outgoing light can be diffracted or transmitted, resulting in a periodic trend, which is the optical analog of "Pendellösung" oscillations in the X-ray region.

When there is no permitted mode in photonic band dispersion for the transmitted beam, such as in the second pseudo gap or in some anticrossing with a low-dispersion band, only diffraction states are allowed, resulting in a strong extinction for light travelling through the crystal. In these region we observed abrupt jumps both in theoretical and experimental phase delay, measured for sample having an increasing number of layers. The group index, derived from phase data, denoted a transition from slow to superluminal and even negative group velocity depending on sample thickness. The latter does not represents a violation of causality principle since we are in a region of low, but non-zero, transmission.

Finally we studied the optical properties of a sample oriented with (100) planes parallel to the substrate. Here we demonstrated that optical spectra along ΓX direction and its surroundings are strongly influenced by diffraction bands arising in the high-energy region. Moreover, the absence of a pseudogap in X-point makes this region very different from those oriented along [111] direction, from the point of view of optical measurements.

Albeit a lot of work has been done on self-assembled colloidal crystals there are plenty of issues to be investigated and understood. Regarding bare opals the high-energy region deserves a more extensive investigation, most of all because of the improvements that have been made in sample quality. Moreover the realization of structures embedding a line or planar defect must be accurately characterized also from a theoretical point of view, at least as they may be one of the basic building blocks for the foreseen optical circuits.

Our theoretical model can be further improved subdividing the sphere in a higher number of slices and can be applied to inverse opals. The latter are very interesting structures for physics research and even for technological implementations. The presence of a complete photonic band gap can be exploited to study modification of spontaneous emission life time, but also to create an ideal optical cavity, with full 3D confinement. In particular, the scattering matrix method can be properly extended to study spontaneous emission processes, hence our approach can be fully exploited to analyse this kind of experiments.

Appendices

Geometrical description of the opal lattice

In this appendix we would like to recall some details about the sphere arrangement in opals photonic crystals. The face centered cubic (fcc) and the hexagonal close-packed (hcp) lattice are described by means of their primitive vectors. The respective reciprocal lattice vectors are given, together with the high-symmetry points of the first Brillouin zone. Finally a brief overview on the two dimensional graphite lattice is presented, as it is needed when dealing with the five cylinders approximation.

A.1   The face centered cubic lattice

The fcc lattice is obtained by repeating periodically in space a cubic cell of edge a with spheres at the corners and at the center of the faces. The primitive vectors of the fcc Bravais lattice, expressed in a Cartesian reference frame, are:

$$\mathbf{a}_1 = \frac{a}{2}(0,1,1)\,, \quad \mathbf{a}_2 = \frac{a}{2}(1,0,1)\,, \quad \mathbf{a}_3 = \frac{a}{2}(1,1,0)\,, \tag{A.1}$$

and they are shown in Fig. A.1(a). The volume of the primitive cell is $\Omega = \mathbf{a}_1 \cdot (\mathbf{a}_2 \times \mathbf{a}_3) = a^3/4$. The coordination number of the fcc structure, i.e. the number of nearest neighbours, is twelve: choosing the origin in a lattice site, these nearest neighbours are located in the positions $(a/2)(0,\pm 1,\pm 1)$ and cyclic permutations.

The primitive vectors of the reciprocal lattice can be found by means of the following expressions:

$$\mathbf{g}_1 = \frac{2\pi}{\Omega}\, \mathbf{a}_2 \times \mathbf{a}_3\,, \quad \mathbf{g}_2 = \frac{2\pi}{\Omega}\, \mathbf{a}_3 \times \mathbf{a}_1\,, \quad \mathbf{g}_3 = \frac{2\pi}{\Omega}\, \mathbf{a}_1 \times \mathbf{a}_2\,. \tag{A.2}$$

In particular, for the fcc case, one obtains:

$$\mathbf{g}_1 = \frac{2\pi}{a}(-1,1,1)\,, \quad \mathbf{g}_2 = \frac{2\pi}{a}(1,-1,1)\,, \quad \mathbf{g}_3 = \frac{2\pi}{a}(1,1,-1)\,. \tag{A.3}$$
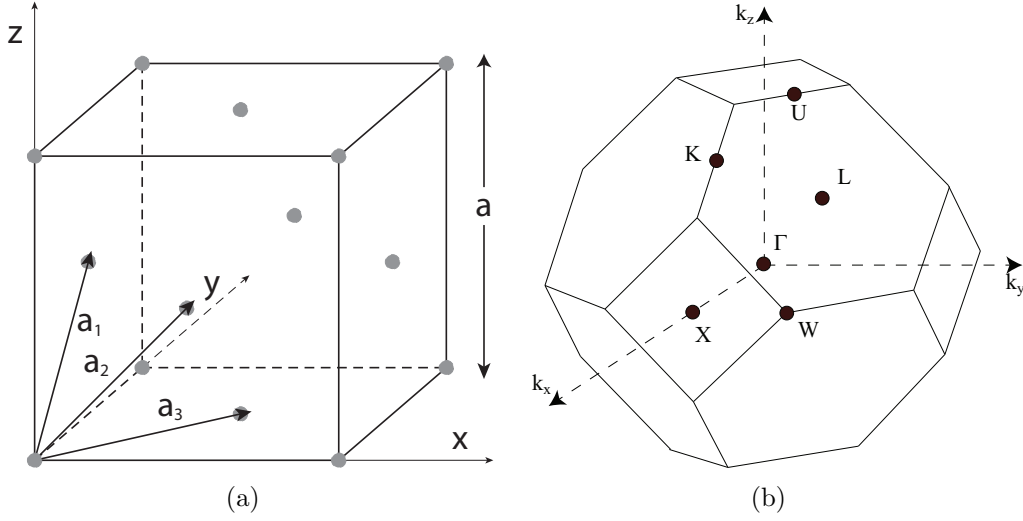
Figure A.1: (a) Fcc lattice and primitive translation vectors $\mathbf{a}_1$, $\mathbf{a}_2$ and $\mathbf{a}_3$ given in Eqs. (A.1). (b) Brillouin zone of the fcc structure. The high-symmetry points are also indicated.

Once the reciprocal lattice is known one can define the first Brillouin zone (or simply the Brillouin zone), that has the property that any point of the cell is closer to the chosen lattice point, taken as the origin ($\mathbf{g} \equiv 0$), than to any other. The Brillouin zone of the fcc lattice is the truncated octahedron shown in Fig. A.1(b). Here we list the coordinates of the high-symmetry points labelled in the figure:

$$
\begin{aligned}
\Gamma &= \tfrac{2\pi}{a}(0,0,0)\,, & X &= \tfrac{2\pi}{a}(1,0,0)\,, \\
L &= \tfrac{2\pi}{a}(1/2,1/2,1/2)\,, & W &= \tfrac{2\pi}{a}(1,1/2,0)\,, \\
U &= \tfrac{2\pi}{a}(1/4,1/4,1)\,, & K &= \tfrac{2\pi}{a}(3/4,0,3/4)\,.
\end{aligned}
\tag{A.4}
$$

Γ indicates the center of Brillouin zone and, consequently, the origin of the reciprocal lattice. The X point is the center of a square face, so there are six degenerate X points. W point is a corner of the zone and there are 24 of them. Points U and K are both placed at the center of the hexagon edge but they are not equivalent, as demonstrated in Sect. 3.3, since the former is also the center of a square edge. Usually the band dispersion is plotted along high-symmetry lines, joining two of the previous listed points, of the first Brillouin zone.

Every reciprocal lattice vector $\mathbf{G}_m = m_1\mathbf{g}_1 + m_2\mathbf{g}_2 + m_3\mathbf{g}_3$, where m_1, m_2 and m_3 are integer numbers having no common divisor, is normal to a family of parallel and equidistant planes containing all the direct lattice points. This bijective correspondence allows us to label each family of parallel planes in the direct lattice by means of the tern of integers m_1, m_2 and m_3, also known as Miller indices, of the reciprocal lattice vectors perpendicular to them. Standard notation indicates with round brackets a particular family of planes and with square brackets the direction normal to them. As an example, for an fcc lattice

Figure A.2: (a) Fcc lattice viewed as an hexagonal close-packed lattice. Primitive translation vectors $\mathbf{b}_1$, $\mathbf{b}_2$ and $\mathbf{b}_3$ and basis vectors $\mathbf{d}_1$, $\mathbf{d}_2$ and $\mathbf{d}_3$ given in Eqs. (A.8) are indicated. (b) Brillouin zone of the hcp structure. The main high-symmetry points are labelled.

the (111) planes are perpendicular to the cube diagonal and to the reciprocal lattice vectors that identifies ΓL line in Brillouin zone, while the [100] follows ΓX line and in direct lattice is parallel to cube edge.

A.2   The hexagonal close packed structure

The hexagonal arrangement that is usually presented in text books is described by the following primitive vectors, in Cartesian coordinates:

$$\mathbf{b}_1 = b\,(1,0,0)\ , \quad \mathbf{b}_2 = b\left(\frac{1}{2}, \frac{\sqrt{3}}{2}, 0\right)\ , \quad \mathbf{b}_3 = c\,(0,0,1)\ , \qquad (\text{A.5})$$

with two basis vectors defining the stacking sequence in the z direction:

$$\mathbf{d}_1 = (0,0,0)\ , \quad \mathbf{d}_2 = \left(0, \frac{b}{\sqrt{3}}, \frac{c}{2}\right)\ . \qquad (\text{A.6})$$

In the close packing situation, a particular case of hexagonal lattice wherein each lattice site is occupied by hard spheres touching each other, the lattice constant b is equal to sphere diameter and $c = \sqrt{8/3}\,b$. The stacking of the planes follows the sequence AB, AB, ...

87

The fcc structure is another case of a close-packed arrangement. The (111) planes, i.e. those perpendicular to cube diagonal, have their sites arranged in a triangular lattice and their stacking sequence along the [111] direction is ABC, ABC ... The lattice vectors describing the structure are the same as Eq. (A.5), where the lattice constant in the vertical direction c is equal to $\sqrt{6}\,b$. This situation is depicted in Fig. A.2(a). It is worth noticing that the sphere diameter b in the opal structure is equal to $1/\sqrt{2}$ times the fcc lattice constant a. It can be useful to describe the fcc lattice in terms of a stacking of hexagonal planes, as the opals are commonly grown with (111) planes parallel to the substrate. The unit cell volume of such a layout is

$$\Omega = \frac{3\sqrt{3}}{2}b^3 = \frac{3}{4}a^3\,,\tag{A.7}$$

i.e. three times the volume of the fcc unit cell. The sphere arrangement is then reproduced by means of three basis vectors, depicted in Fig. A.2(a):

$$\mathbf{d}_1 = (0,0,0)\,,\quad \mathbf{d}_2 = b\left(0,\frac{1}{\sqrt{3}},\sqrt{\frac{2}{3}}\right)\,,\quad \mathbf{d}_3 = b\left(0,-\frac{1}{\sqrt{3}},2\sqrt{\frac{2}{3}}\right)\,,\tag{A.8}$$

or, to preserve the inversion symmetry:

$$\mathbf{d}_1 = (0,0,0)\,,\quad \mathbf{d}_2 = b\left(0,\frac{1}{\sqrt{3}},\sqrt{\frac{2}{3}}\right)\,,\quad \mathbf{d}_3 = b\left(0,-\frac{1}{\sqrt{3}},-\sqrt{\frac{2}{3}}\right)\,.\tag{A.9}$$

In other words, the three planes are shifted with respect to the previous ones along the y direction by a quantity equal to $1/\sqrt{3}$.

Eqs. (A.2) allow us to derive the reciprocal lattice vectors of this particular hexagonal structure:

$$\mathbf{g}_1 = \frac{2\pi}{b}\left(1,-\frac{1}{\sqrt{3}},0\right)\,,\quad \mathbf{g}_2 = \frac{2\pi}{b}\left(0,\frac{2}{\sqrt{3}},0\right)\,,\quad \mathbf{g}_3 = \frac{2\pi}{b}\left(0,0,\frac{1}{\sqrt{6}}\right)\,.\tag{A.10}$$

They still describe a hexagonal lattice, whose Brillouin zone is depicted in Fig. A.2(b). The coordinates of the high-symmetry points are the followings:

$$
\begin{aligned}
&\Gamma = \frac{2\pi}{b}(0,0,0)\,, &&\mathrm{A} = \frac{2\pi}{b}\left(0,0,\frac{1}{\sqrt{6}}\right)\,,\\
&\mathrm{M} = \frac{2\pi}{b}\left(0,\frac{1}{\sqrt{3}},0\right)\,, &&\mathrm{L} = \frac{2\pi}{b}\left(0,\frac{1}{\sqrt{3}},\frac{1}{\sqrt{6}}\right)\,,\\
&\mathrm{K} = \frac{2\pi}{b}\left(\frac{1}{3},\frac{1}{\sqrt{3}},0\right)\,, &&\mathrm{H} = \frac{2\pi}{b}\left(\frac{1}{3},\frac{1}{\sqrt{3}},\frac{1}{\sqrt{6}}\right)\,.
\end{aligned}\tag{A.11}
$$

As in the previous case the Γ point is the center of the Brillouin zone, while the A point is the center of the hexagonal face. The center of a lateral face of the prism is labelled with the letter M. L is the midpoint of an hexagon edge,
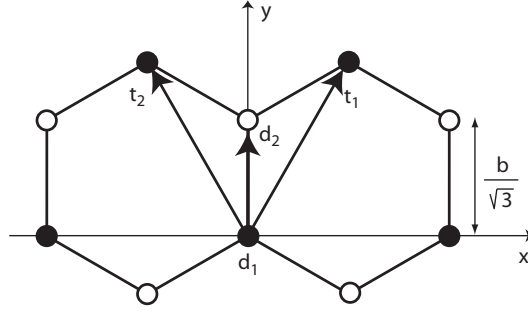
Figure A.3: Two dimensional graphite lattice. The primitive translation vectors $\mathbf{t}_1$ and $\mathbf{t}_2$ and the basis vectors $\mathbf{d}_1$ and $\mathbf{d}_2$, given in the text, are also indicated.

while K is the midpoint of a rectangle edge. Finally, H point indicates a vertex of the prism.

It has to be mentioned here that the only way to introduce the relaxed structure employed in Sect. 3.1 and in Sect. 5.2 in the plane wave expansion code is to describe the sphere layout as an hexagonal stacking sequence, where the distance between two consecutive planes is equal to $a/\sqrt{3}$ as in the fcc lattice and the in-plane lattice constant assumes a proper value greater that the sphere diameter.

A.3   The graphite lattice

As discussed in Sect. 2.1, within the interpenetration region between two consecutive (111) planes, the sphere caps of the opal structure are arranged in a graphite lattice. Moreover, the outermost cylinders in the five-cylinder approximation are displaced following the same layout. Hereafter we will give the geometrical parameters of this lattice.

The two dimensional graphite structure, illustrated in Fig. A.3, is a composite one and consists of two identical triangular sublattices (plotted with closed and open points for clarity). Therefore the primitive vectors are the same as the hexagonal lattice:

$$\mathbf{t}_1 = b\left(\frac{1}{2}, \frac{\sqrt{3}}{2}\right) \quad \mathbf{t}_2 = b\left(-\frac{1}{2}, \frac{\sqrt{3}}{2}\right), \tag{A.12}$$

with the choice of axes indicated in the figure. The two vectors describing the basis are the followings:

$$\mathbf{d}_1 = 0 \quad \mathbf{d}_2 = b\left(0, \frac{1}{\sqrt{3}}\right). \tag{A.13}$$

It would be impossible to define this lattice, also known as honeycomb structure, by means of a single basis vector. If so a translation vector joining

an atom with any of its first neighbours would have his opposite pointing at the center of an hexagon, where no atoms exists.

In our particular case, the two basis vectors identifies the sphere caps, or the cylinders, belonging to the upper and lower interpenetrating layers. Notice that in the sphere layout the inversion symmetry is broken by the fact that the cap radii changes across the vertical direction and they are equal only in the contact point. On the other hand the five-cylinder layout preserves the inversion symmetry as the radii are always identical. This property is essential in order to implement the structure in our scattering matrix code: without the inversion symmetry the eigenvalue problem of Eq. (2.26) is no more symmetric. Since the reciprocal lattice does not depend on the basis, but only on the primitive translation vectors, it is defined by the same vectors as the hexagonal one:

$$ g_1 = \frac{2\pi}{b}\left(1, \frac{1}{\sqrt{3}}\right) \quad g_2 = \frac{2\pi}{b}\left(-1, \frac{1}{\sqrt{3}}\right) . \tag{A.14} $$

It should be remembered that this property is essential in order to implement the interpenetration region in the scattering matrix code, as the condition of having the same reciprocal lattice vectors $\mathbf{G}$ in all the structure is automatically satisfied.

Appendix B

Fourier transforms of the dielectric function

Both the plane-wave expansion and the scattering matrix method presented in the text take advantage of the dielectric function periodicity by using the Fourier transform coefficients. In this appendix we would like to present in detail the analytical calculations that lead to the Fourier transform of the dielectric function of the structures studied in this thesis.

B.1 Three-dimensional Fourier transforms

Consider a lattice made of N spheres of radius R and dielectric constant ε_a embedded in a medium of dielectric constant ε_b and arranged in the primitive cell according to the basis vectors $\mathbf{d}_\nu$ ($\nu = 1, \ldots, N$). The spatial dependence of the total dielectric function $\varepsilon(\mathbf{r})$ can be expressed as follows:

$$\varepsilon(\mathbf{r}) = \varepsilon_b + \sum_{\mathbf{d}_\nu} (\varepsilon_a - \varepsilon_b) \theta_\nu(R - r) , \qquad (B.1)$$

where $\theta_\nu(R-r)$ is a particular case of step function in spherical coordinates that is equal to 1 inside each sphere and vanishes outside. The Fourier transform of such a function is written as:

$$
\begin{aligned}
\varepsilon(\mathbf{G}) &= \frac{1}{\Omega} \int_\Omega d\mathbf{r}\, \varepsilon(\mathbf{r}) e^{-i\mathbf{G}\cdot\mathbf{r}} \\
&= \frac{\varepsilon_b}{\Omega} \int_\Omega d\mathbf{r}\, e^{-i\mathbf{G}\cdot\mathbf{r}} + \frac{\varepsilon_a - \varepsilon_b}{\Omega} \sum_{\mathbf{d}_\nu} e^{-i\mathbf{G}\cdot\mathbf{d}_\nu} \int_{V_{\mathrm{sph}}} d\mathbf{r}\, e^{-i\mathbf{G}\cdot\mathbf{r}} ;
\end{aligned}
\qquad (B.2)
$$

where $\mathbf{G}$ is a reciprocal lattice vector, Ω the unit cell volume and V_{sph} the sphere volume.

Firstly, the Fourier transform has to be evaluated for $\mathbf{G} = 0$. In this case the first integral is equal to the unit cell volume, while the second corresponds

to the sphere volume and the summation reduces to the sphere number N. The Fourier transform is thus given by the following expression:

$$\varepsilon(\mathbf{G} = 0) = \varepsilon_b + (\varepsilon_a - \varepsilon_b)\frac{N\,V_{\mathrm{sph}}}{\Omega}\,, \tag{B.3}$$

i.e. it represents the mean value of the dielectric function over the whole unit cell.

On the other hand, when $\mathbf{G} \neq 0$, the first term of Eq. (B.2) vanishes and does not contribute to the Fourier transform. The second addendum can be rewritten as the product of a structure factor $S_\nu(\mathbf{G})$ and a form factor $\varepsilon_{\mathrm{sph}}(\mathbf{G})$, the former depending on basis vectors and the latter depending on the geometrical parameters of the spheres constituting the lattice. These factors are defined, respectively, as

$$S_\nu(\mathbf{G}) = \sum_{\mathbf{d}_\nu} e^{-i\mathbf{G}\cdot\mathbf{d}_\nu}\,, \tag{B.4}$$

$$\varepsilon_{\mathrm{sph}}(\mathbf{G}) = \int_{V_{\mathrm{sph}}} d\mathbf{r}\, e^{-i\mathbf{G}\cdot\mathbf{r}}\,. \tag{B.5}$$

Therefore one obtains the following relationship for the Fourier transform:

$$\varepsilon(\mathbf{G} \neq 0) = \frac{\varepsilon_a - \varepsilon_b}{\Omega}\, S_\nu(\mathbf{G})\, \varepsilon_{\mathrm{sph}}(\mathbf{G})\,. \tag{B.6}$$

In this thesis work, with the exception of Chapt. 4 where a supercell has been introduced, two different Bravais lattice have been employed, resulting in two structure factors. The first one concerns the face centered cubic (fcc) lattice: $S_\nu(\mathbf{G})$ is equal to unity, as there is only one sphere per unit cell, placed in the origin. On the other hand, when the fcc lattice is described as a hexagonal one, three basis vectors have to be defined. In the latter case the structure factor turns out to be:

$$S_{\mathbf{G}\nu} = 1 + e^{-ib\left(G_y/\sqrt{3} + G_z\sqrt{2/3}\right)} + e^{ib\left(G_y/\sqrt{3} + G_z\sqrt{2/3}\right)}\,. \tag{B.7}$$

Note that the above definition of the basis vectors correspond to the second one given in App. A, i.e. the one that preserve inversion symmetry. This way, the matrix whose elements are the Fourier components becomes real and it is possible to apply standard diagonalization methods for real matrices, which are less time-consuming than those for complex ones.

The definition of the form factor is easily extended to the instance of having one or more cylinders substituting each sphere. In this case the sphere form factor has to be replaced by a proper one:

$$\varepsilon_{\mathrm{cyl}}(\mathbf{G}) = \int_{V_{\mathrm{cyl}}} d\mathbf{r}\, e^{-i\mathbf{G}\cdot\mathbf{r}}\,. \tag{B.8}$$

In the following paragraphs the analytical expression of the form factors for the specific structures studied in the work will be derived.

One dielectric sphere. The form factor of a single dielectric sphere of radius R is obtained by solving the integral in Eq. (B.5) in spherical coordinates:

$$\varepsilon_{\mathrm{sph}}(\mathbf{G}) = \int_0^{2\pi} d\varphi \int_0^{\pi} d\vartheta \int_0^{R} dr\, r^2 \sin\vartheta\, e^{-iGr\cos\vartheta}$$
$$= 4\pi \frac{\sin GR - GR\cos GR}{G^3}\,, \tag{B.9}$$

where $G = |\mathbf{G}|$.

One dielectric cylinder. Consider now the case of a single cylinder of radius and height R_1 and H_1, respectively. This is the case of the one-cylinder approximation described in Sect. 2.4.

By solving Eq. (B.8) in cylindrical coordinates one gets:

$$\varepsilon_{\mathrm{cyl}} = \int_0^{2\pi} d\varphi \int_0^{R_1} dr\, re^{-i\mathbf{G}_\parallel \cdot \mathbf{r}_\parallel} \int_{-H_1/2}^{H_1/2} dz\, e^{-iG_z z}\,, \tag{B.10}$$

where $\mathbf{G}_\parallel$ and $\mathbf{r}_\parallel$ are, respectively, the projection of $\mathbf{G}$ and $\mathbf{r}$ in the horizontal plane.

Now it is necessary to study separately the cases of $\mathbf{G}_\parallel = 0$ and $\mathbf{G}_\parallel \neq 0$. In the first case the form factor is written as:

$$\varepsilon_{\mathrm{cyl}} = \pi R_1^2 H_1 \frac{\sin(G_z H_1/2)}{G_z H_1/2}\,. \tag{B.11}$$

On the other hand, when $\mathbf{G}_\parallel \neq 0$, one obtains:

$$\varepsilon_{\mathrm{cyl}} = 2\pi \frac{R_1}{G_\parallel} J_1(G_\parallel R_1) H_1 \frac{\sin(G_z H_1/2)}{G_z H_1/2}\,, \tag{B.12}$$

where $J_1(x)$ is the Bessel function of the first kind and having order 1.

Three dielectric cylinders. Here in each lattice site the sphere has been replaced by three cylinders touching each other and with their axis oriented along the z-direction. The cylinder radii and heights are R_1, R_2, R_3 and H_1, H_2, H_3 (the situation is depicted in Fig. 2.5 of in Chapt. 2), respectively. Recalling that $R_1 = R_3$ and $H_1 = H_3$ the form factor is written:

$$\varepsilon_{\mathrm{cyl}} = \int_0^{2\pi} d\varphi \int_0^{R_1} dr\, re^{-i\mathbf{G}_\parallel \cdot \mathbf{r}_\parallel} \int_{H_2/2}^{H_2/2+H_1} dz\, e^{-iG_z z}$$
$$+ \int_0^{2\pi} d\varphi \int_0^{R_2} dr\, re^{-i\mathbf{G}_\parallel \cdot \mathbf{r}_\parallel} \int_{-H_2/2}^{H_2/2} dz\, e^{-iG_z z} \tag{B.13}$$
$$+ \int_0^{2\pi} d\varphi \int_0^{R_1} dr\, re^{-i\mathbf{G}_\parallel \cdot \mathbf{r}_\parallel} \int_{-H_2/2-H1}^{-H_2/2} dz\, e^{-iG_z z}\,.$$

Again if $\mathbf{G}_\parallel = 0$, the form factor is given by:

$$\varepsilon_{\text{cyl}} = \pi R_1^2 H_1 \frac{\sin(G_z \frac{H_1}{2})}{G_z \frac{H_1}{2}} \cos\left[G_z \left(H_2 + \frac{H_1}{2}\right)\right] + \pi R_2^2 H_2 \frac{\sin(G_z \frac{H_2}{2})}{G_z \frac{H_2}{2}}, \quad \text{(B.14)}$$

while, if $\mathbf{G}_\parallel \neq 0$, one gets:

$$\begin{aligned}
\varepsilon_{\text{cyl}} =& 2\pi \frac{R_1}{G_\parallel} J_1(G_\parallel R_1) H_1 \frac{\sin(G_z \frac{H_1}{2})}{G_z \frac{H_1}{2}} \cos\left[G_z \left(H_2 + \frac{H_1}{2}\right)\right] \\
&+ 2\pi \frac{R_2}{G_\parallel} J_1(G_\parallel R_2) H_2 \frac{\sin(G_z \frac{H_2}{2})}{G_z \frac{H_2}{2}},
\end{aligned} \quad \text{(B.15)}$$

where $J_1(x)$ is the Bessel function of first kind, as in the previous example.

Five dielectric cylinders. The last example we deal with is illustrated in Fig. 2.6 of Chapt. 2: each sphere is now substituted by five cylinders of radii $R_1 = R_5$, $R_2 = R_3$ and R_3 and of heights $H_1 = H_5$, $H_2 = H_3$ and H_3. The form factor is the sum of five terms:

$$\begin{aligned}
\varepsilon_{\text{cyl}} =& \int_0^{2\pi} d\varphi \int_0^{R_1} dr\, r e^{-i\mathbf{G}_\parallel \cdot \mathbf{r}_\parallel} \int_{H_3/2+H_2}^{H_3/2+H_2+H_1} dz\, e^{-iG_z z} \\
&+ \int_0^{2\pi} d\varphi \int_0^{R_2} dr\, r e^{-i\mathbf{G}_\parallel \cdot \mathbf{r}_\parallel} \int_{H_3/2}^{H_3/2+H_2} dz\, e^{-iG_z z} \\
&+ \int_0^{2\pi} d\varphi \int_0^{R_3} dr\, r e^{-i\mathbf{G}_\parallel \cdot \mathbf{r}_\parallel} \int_{-H_3/2}^{H_3/2} dz\, e^{-iG_z z} \\
&+ \int_0^{2\pi} d\varphi \int_0^{R_2} dr\, r e^{-i\mathbf{G}_\parallel \cdot \mathbf{r}_\parallel} \int_{-H_3/3-H2}^{-H_3/2} dz\, e^{-iG_z z} \\
&+ \int_0^{2\pi} d\varphi \int_0^{R_1} dr\, r e^{-i\mathbf{G}_\parallel \cdot \mathbf{r}_\parallel} \int_{-H_3/2-H_2-H_1}^{-H_3/2-H_2} dz\, e^{-iG_z z}.
\end{aligned} \quad \text{(B.16)}$$

Once again one needs to distinguish the case of $\mathbf{G}_\parallel = 0$, that gives:

$$\begin{aligned}
\varepsilon_{\text{cyl}} =& \pi R_1^2 H_1 \frac{\sin(G_z H_1/2)}{G_z H_1/2} \cos\left[G_z(H_3 + 2H_2 + H_1)/2\right] \\
&+ \pi R_2^2 H_2 \frac{\sin(G_z H_2/2)}{G_z H_2/2} \cos\left[G_z(H_3 + H_2/2)\right] + \pi R_3^2 H_3 \frac{\sin(G_z H_3/2)}{G_z H_3/2},
\end{aligned} \quad \text{(B.17)}$$

while for $\mathbf{G}_\parallel \neq 0$ the form factor is:

$$\begin{aligned}
\varepsilon_{\text{cyl}} =& 2\pi \frac{R_1}{G_\parallel} J_1(G_\parallel R_1) H_1 \frac{\sin(G_z H_1/2)}{G_z H_1/2} \cos\left[G_z(H_3 + 2H_2 + H_1)/2\right] \\
&+ 2\pi \frac{R_2}{G_\parallel} J_1(G_\parallel R_2) H_2 \frac{\sin(G_z H_2/2)}{G_z H_2/2} \cos\left[G_z(H_3 + H_2/2)\right] \\
&+ 2\pi \frac{R_3}{G_\parallel} J_1(G_\parallel R_3) H_3 \frac{\sin(G_z H_3/2)}{G_z H_3/2},
\end{aligned} \quad \text{(B.18)}$$

where, once again, $J_1(x)$ is the Bessel function of the first kind.

Eventually, the case of a **supercell** deserves a detailed description. Three different examples of this particular unit cell have been introduced in the text. Firstly the case, relatively simple, of a symmetric cell constituted by n_1 dielectric spheres embedded in air. Secondly, an asymmetric supercell, wherein the sphere stacking lies on a homogeneous dielectric layer, has been employed to analyse the finite-size effects taking place in a thin opal film grown on a substrate. Finally, the particular case of an opal embedding a planar defect has been taken into account. All these structures have been extensively described in Chapt. 4.

The first instance can be easily traced back to the previous example by defining a proper structure factor from the basis vectors definitions of Eqs. (4.4) and (4.5) that we recall here for simplicity:

$$\mathbf{d}_\nu = b\left(0, \frac{\nu - 1/2}{\sqrt{3}}, (\nu - 1/2)\sqrt{\frac{2}{3}}\right), \qquad (B.19)$$

where $\nu = \pm 1, \pm 2, \ldots, \pm n_1/2$, for an even number of spheres n_1, and

$$\mathbf{d}_\nu = b\left(0, \frac{\nu}{\sqrt{3}}, \nu\sqrt{\frac{2}{3}}\right), \qquad (B.20)$$

where ν assumes all the integer numbers in the range $[-(n_1 - 1)/2; (n_1 - 1)/2]$, for a odd number of spheres.

In the other two examples, when a homogeneous layer, characterized by a thickness h_{lay} and a dielectric function ε_c, is introduced in the unit cell, the spatial dependence of the dielectric function can be expressed by the following relationship:

$$\varepsilon(\mathbf{r}) = \varepsilon_b + \sum_{\mathbf{d}_\nu}(\varepsilon_a - \varepsilon_b)\theta_\nu(R - r) + (\varepsilon_c - \varepsilon_b)\theta_c(h_{\text{lay}}/2 - |z|), \qquad (B.21)$$

where θ_c is a step function that is equal to one inside the homogeneous layer, and vanishes outside. The vectors describing the position of the layer are

$$\mathbf{d}_c = \left(0, 0, \frac{a}{\sqrt{3}}\frac{h_{\text{sub}} + h_{\text{op}}}{2}\right), \qquad (B.22)$$

for the asymmetric supercell, where h_{sub} and h_{op} are the total heights of the substrate and the opal defined in Chapt. 4, and

$$\mathbf{d}_c = (0, 0, 0), \qquad (B.23)$$

when it represents a planar defect embedded in a bulk opals. The Fourier transform of the dielectric function $\varepsilon(\mathbf{r})$ of the supercell is given by the following

relationship:

$$\varepsilon(\mathbf{G}) = \frac{\varepsilon_b}{\Omega} \int_{\Omega} d\mathbf{r}\, e^{-i\mathbf{G}\cdot\mathbf{r}} + \frac{\varepsilon_a - \varepsilon_b}{\Omega} \sum_{\mathbf{d}_\nu} e^{-i\mathbf{G}\cdot\mathbf{d}_\nu} \int_{V_{\mathrm{sph}}} d\mathbf{r}\, e^{-i\mathbf{G}\cdot\mathbf{r}}$$
$$+ \frac{\varepsilon_c - \varepsilon_b}{\Omega} e^{-i\mathbf{G}\cdot\mathbf{d}_c} \int_{V_c} d\mathbf{r}\, e^{-i\mathbf{G}\cdot\mathbf{r}} \,. \tag{B.24}$$

where Ω is the supercell volume and V_c is the layer volume.

First of all, the Fourier component corresponding to $\mathbf{G} = 0$ is equal to the mean value of the dielectric function $\varepsilon(\mathbf{r})$:

$$\varepsilon(\mathbf{G} = 0) = \varepsilon_b + \frac{n_1}{\Omega}(\varepsilon_a - \varepsilon_b) + \frac{h_l}{h_{\mathrm{SC}}}(\varepsilon_c - \varepsilon_b) \,. \tag{B.25}$$

When the reciprocal lattice vectors differs from zero, the Fourier transform can be written in terms of structure and form factors, remembering that the first addendum of Eq. (B.24) vanishes:

$$\varepsilon(\mathbf{G} \neq 0) = \frac{\varepsilon_a - \varepsilon_b}{\Omega} S_\nu(\mathbf{G})\, \varepsilon_{\mathrm{sph}}(\mathbf{G}) + \frac{\varepsilon_c - \varepsilon_b}{\Omega} e^{-i\mathbf{G}\cdot\mathbf{d}_c}(\mathbf{G})\, \varepsilon_{\mathrm{lay}}(\mathbf{G}) \,. \tag{B.26}$$

In particular, the homogeneous layer form factor $\varepsilon_{\mathrm{lay}}(\mathbf{G})$ is defined as follows:

$$\varepsilon_{\mathrm{lay}}(\mathbf{G}) = \int_S d\mathbf{r}_\| e^{-i\mathbf{G}_\|\cdot\mathbf{r}_\|} \int_{h_{\mathrm{lay}}/2}^{h_{\mathrm{lay}}/2} dz\, e^{-iG_z\cdot z} \,, \tag{B.27}$$

where S is the in-plane area of the supercell. It is now clear that $\varepsilon_{\mathrm{lay}}(\mathbf{G})$ is always equal to zero unless $\mathbf{G}_\| = 0$. In the latter case, it results in the following expression:

$$\varepsilon_{\mathrm{lay}}(\mathbf{G}) = \frac{h_{\mathrm{lay}}}{h_{\mathrm{SC}}} \frac{\sin G_z h_{\mathrm{lay}}/2}{G_z h_{\mathrm{lay}}/2} \,, \tag{B.28}$$

where h_{SC} is the cell height. In other words, the Fourier transform $\varepsilon(\mathbf{G})$ is affected by the presence of the homogeneous layer only when the in-plane reciprocal lattice vector is equal to zero.

Regarding the first term of Eq. (B.26), the structure factor $S_\nu(\mathbf{G})$ of the asymmetric supercell is the same of that of the symmetric cell, as sphere positions are left unchanged, while for the defect supercell it can be derived following the proper definitions of the basis vectors given in Chapt. 4 by Eqs. (4.8).

Moreover these calculations can be easily extended to the cylinder approximation case by replacing $\varepsilon_{\mathrm{sph}}$ by the relevant form factor.

B.2 Two dimensional Fourier transform

In the scattering matrix method the periodicity of the dielectric function is restricted to the plane perpendicular to the stacking direction, so it is described

by a two dimensional lattice and its Fourier transform is calculated over the unit cell surface. Considering only the case of circular rods of radius R and dielectric function ε_a in a medium of dielectric function ε_b, the total dielectric function is given by the following expression:

$$\varepsilon(\mathbf{r}) = \varepsilon_b + \sum_{\mathbf{d}_\nu} (\varepsilon_a - \varepsilon_b)\theta_\nu(R - r)\,, \tag{B.29}$$

where $\theta(\mathbf{r})$ represents the Heaviside function in polar coordinates and $\mathbf{d}_\nu$ are the bidimensional vectors of lattice basis.

The Fourier components are determined according to a procedure similar to the one employed in the previous section, bearing in mind that the integration is now restricted to two dimensions:

$$\varepsilon(\mathbf{G}) = \frac{1}{S} \int_S d\mathbf{r}\, e^{-i\mathbf{G}\cdot\mathbf{r}}\,, \tag{B.30}$$

where S is the unit cell area.

As in the previous section, the Fourier transform becomes equal to the mean value of the dielectric function when $\mathbf{G} = 0$:

$$\varepsilon(\mathbf{G} = 0) = \varepsilon_b + (\varepsilon_a - \varepsilon_b)\frac{N\, A_{\mathrm{rod}}}{S}\,, \tag{B.31}$$

where A_{rod} is the area of a single circle.

When $\mathbf{G} \neq 0$ we can once again express the Fourier transforms in terms of the form factor and the structure factor:

$$\varepsilon(\mathbf{G}) = \frac{\varepsilon_a - \varepsilon_b}{S}\, S_\nu(\mathbf{G})\, \varepsilon_{\mathrm{rod}}(\mathbf{G})\,. \tag{B.32}$$

As specified before, we restrict ourselves to the case of cylindric rods of radius R, hence the form factor is written as follows:

$$\varepsilon_{\mathrm{rod}}(\mathbf{G}) = \int_{A_{\mathrm{rod}}} d\mathbf{r}\, e^{-i\mathbf{G}\cdot\mathbf{r}} = \int_0^{2\pi} d\varphi \int_0^R e^{-iGr\cos\varphi} = 2\pi R^2 \frac{J_1(GR)}{GR}\,. \tag{B.33}$$

When dealing with the hexagonal lattice, that is the in-plane lattice of each (111) plane of the opal structure, the structure factor is easily obtained: as there is only one atom per unit cell, the factor is equal to unity. Otherwise, in the case of the graphite lattice the basis is constituted by two vectors and the structure factor results in:

$$S_{\mathbf{G}\nu} = 1 + e^{-ibG_y/\sqrt{3}}, \tag{B.34}$$

according to the definition given in App. A.3.

Bibliography

[1] E. Yablonovitch. Inhibited Spontaneous Emission in Solid-State Physics and Electronics. *Phys. Rev. Lett.*, **58** (20): 2059–2062, May 1987.

[2] S. John. Strong localization of photons in certain disordered dielectric superlattices. *Phys. Rev. Lett.*, **58** (23): 2486–2489, Jun 1987.

[3] M. Scalora, M. J. Bloemer, A. S. Manka, J. P. Dowling, C. M. Bowden, R. Viswanathan, and J. W. Haus. Pulsed second-harmonic generation in nonlinear, one-dimensional, periodic structures. *Phys. Rev. A*, **56** (4): 3166–3174, Oct 1997.

[4] M. Centini, C. Sibilia, M. Scalora, G. D'Aguanno, M. Bertolotti, M. J. Bloemer, C. M. Bowden, and I. Nefedov. Dispersive properties of finite, one-dimensional photonic band gap structures: Applications to nonlinear quadratic interactions. *Phys. Rev. E*, **60** (4): 4891 – 4898, 1999.

[5] G. D'Aguanno, M. Centini, M. Scalora, C. Sibilia, M. J. Bloemer, C. M. Bowden, J. W. Haus, and M. Bertolotti. Group velocity, energy velocity, and superluminal propagation in finite photonic band-gap structures. *Phys. Rev. E*, **6303** (3): 036610, 2001.

[6] Y. Dumeige, P. Vidakovic, S. Sauvage, I. Sagnes, J. A. Levenson, C. Sibilia, M. Centini, G. D'Aguanno, and M. Scalora. Enhancement of second-harmonic generation in a one-dimensional semiconductor photonic band gap. *Appl. Phys. Lett.*, **78** (20): 3021–3023, 2001.

[7] Y. Sugimoto, N. Ikeda, N. Carlsson, K. Asakawa, N. Kawai, and K. Inoue. Fabrication and characterization of different types of two-dimensional AlGaAs photonic crystal slabs. *J. Appl. Phys.*, **91** (3): 922–929, 2002.

[8] E. Chow, S. Y. Lin, S. G. Johnson, P. R. Villenueve, J. D. Joannopoulos, J. R. Wendt, and G. Vawter. Three-dimensional control of light in a two-dimensional photonic crystal slab. *Nature*, **407** (6807): 983–986, 2000.

[9] V. N. Astratov, D. M. Whittaker, I. S. Culshaw, R. M. Stevenson, M. S. Skolnick, T. F. Krauss, and R. M. De La Rue. Photonic band-structure effects in the reflectivity of periodically patterned waveguides. *Phys. Rev. B*, **60** (24): 16255–16258, 1999.

[10] S. G. Johnson, S. Fan, P. R. Villeneuve, J. D. Joannopoulos, and L. A. Kolodziejski. Guided modes in photonic crystal slabs. *Phys. Rev. B*, **60** (8): 5751–5758, 1999.

[11] S. G. Johnson, P. R. Villeneuve, S. Fan, and J. D. Joannopoulos. Linear waveguides in photonic-crystal slabs. *Phys. Rev. B*, **62** (12): 8212–8222, 2000.

[12] A. Chutinan and S. Noda. Waveguides and waveguide bends in two-dimensional photonic crystal slabs. *Phys. Rev. B*, **62** (7): 4488–4492, 2000.

[13] H. Benisty et al. Radiation losses of waveguide-based two-dimensional photonic crystals: Positive role of the substrate. *Appl. Phys. Lett.*, **76** (5): 532, 2000.

[14] P. Lalanne and G. M. Morris. Highly improved convergence of the coupled-wave method for TM polarization. *J. Opt. Soc. Am. A*, **13** (4): 779–784, 1996.

[15] D. Gerace and L. Andreani. Disorder-induced losses in photonic crystal waveguides with line defects. *Opt. Lett.*, **29** (16): 1897 – 1899, 2004.

[16] D. Gerace and L. Andreani. Low-loss guided modes in photonic crystal waveguides. *Opt. Express*, **13** (13): 4939 – 4951, 2005.

[17] V. N. Astratov, J. S. Culshaw, R. M. Stevenson, D. M. Whittaker, M. S. Skolnick, T. F. Krauss, and R. M. de la Rue. Resonant coupling of near-infrared radiation to photonic bandstructure waveguides. *J. Lightwave Technol.*, **17** (11): 2050–2057, 1999.

[18] M. Galli, M. Belotti, D. Bajoni, M. Patrini, G. Guizzetti, D. Gerace, M. Agio, L. C. Andreani, and Y. Chen. Excitation of radiative and evanescent defect modes in linear photonic crystal waveguides. *Phys. Rev. B*, **70** (8): 081307, 2004.

[19] J. C. Knight, T. A. Birks, P. S. J. Russell, and D. M. Atkin. All-silica single-mode optical fiber with photonic crystal cladding. *Opt. Lett.*, **21** (19): 1547, 1996.

[20] P. Russell. Photonic Crystal Fibers. *Science*, **299** (5605): 358–362, 2003.

[21] A. M. Zheltikov. Nanoscale nonlinear optics in photonic-crystal fibres. *J. Opt. A: Pure Appl. Opt.*, **8**: S47–S72, 2006.

[22] K. Busch and S. John. Photonic band gap formation in certain self-organizing systems. *Phys. Rev. E*, **58** (3): 3896–3908, Sep 1998.

[23] A. Blanco, E. Chomski, S. Grabtchak, M. Ibisate, S. John, S. W. Leonard, C. López, F. Meseguer, H. Miguez, J. P. Mondia, G. A. Ozin, O. Toader, and H. M. van Driel. Large-scale synthesis of a silicon photonic crystal with a complete three-dimensional bandgap near 1. 5 micrometres. *Nature*, **405** (6785): 437 – 440, 2000.

[24] T. Ochiai and J. Sánchez-Dehesa. Superprism effect in opal-based photonic crystals. *Phys. Rev. B*, **64** (24): 245113, Dec 2001.

[25] A. Imhof, W. L. Vos, R. Sprik, and A. Lagendijk. Large Dispersive Effects near the Band Edges of Photonic Crystals. *Phys. Rev. Lett.*, **83** (15): 2942–2945, Oct 1999.

[26] Y. A. Vlasov, S. Petit, G. Klein, B. Hönerlage, and C. Hirlimann. Femtosecond measurements of the time of flight of photons in a three-dimensional photonic crystal. *Phys. Rev. E*, **60** (1): 1030–1035, Jul 1999.

[27] R. M. Amos, J. G. Rarity, P. R. Tapster, T. J. Shepherd, and S. C. Kitson. Fabrication of large-area face-centered-cubic hard-sphere colloidal crystals by shear alignment. *Phys. Rev. E*, **61** (3): 2929–2935, Mar 2000.

[28] G. von Freymann, S. John, S. Wong, V. Kitaev, and G. A. Ozin. Measurement of group velocity dispersion for finite size three-dimensional photonic crystals in the near-infrared spectral region. *Appl. Phys. Lett.*, **86** (5): 053108, 2005.

[29] J. F. Galisteo-López, M. Galli, M. Patrini, A. Balestreri, L. C. Andreani, and C. López. Effective refractive index and group velocity determination of three-dimensional photonic crystals by means of white light interferometry. *Phys. Rev. B*, **73** (12): 125103, 2006.

[30] H. M. van Driel and W. L. Vos. Multiple Bragg wave coupling in photonic band-gap crystals. *Phys. Rev. B*, **62** (15): 9872–9875, Oct 2000.

[31] W. L. Vos and H. M. van driel. Higher order Bragg diffraction by strongly photonic fcc crystals: onset of a photonic bandgap. *Phys. Lett. A*, **272** (1-2): 101 – 106, 2000.

[32] L. M. Goldenberg, J. Wagner, J. Stumpe, B. R. Paulke, and E. Gornitz. Optical properties of ordered arrays of large latex particles. *Physica E*, **17** (1-4): 433 – 435, 2003.

[33] F. Garcia-Santamaria, J. F. Galisteo-López, P. V. Braun, and C. López. Optical diffraction and high-energy features in three-dimensional photonic crystals. *Phys. Rev. B*, **71** (19): 195112, 2005.

[34] H. P. Schriemer, H. M. van Driel, A. F. Koenderink, and W. L. Vos. Modified spontaneous emission spectra of laser dye in inverse opal photonic crystals. *Phys. Rev. A*, **63** (1): 011801, Dec 2000.

[35] A. F. Koenderink, L. Bechger, H. P. Schriemer, A. Lagendijk, and W. L. Vos. Broadband Fivefold Reduction of Vacuum Fluctuations Probed by Dyes in Photonic Crystals. *Phys. Rev. Lett.*, **88** (14): 143903, Mar 2002.

[36] M. Megens, J. E. G. J. Wijnhoven, A. Lagendijk, and W. L. Vos. Fluorescence lifetimes and linewidths of dye in photonic crystals. *Phys. Rev. A*, **59** (6): 4727–4731, Jun 1999.

[37] K. Yoshino, S. Tatsuhara, Y. Kawagishi, M. Ozaki, A. A. Zakhidov, and Z. V. Vardeny. Amplified spontaneous emission and lasing in conducting polymers and fluorescent dyes in opals as photonic crystals. *Appl. Phys. Lett.*, **74** (18): 2590–2592, 1999.

[38] J. D. Joannopoulos, R. D. Meade, and J. N. Winn. *Photonic Crystals: Molding the Flow of Light*. Princeton University Press, Princeton, NJ, 1995.

[39] N. W. Ashcroft and N. D. Mermin. *Solid State Physics*. Saunders College Publishing (Philadelphia), 1976.

[40] G. Grosso and G. Pastori Parravicini. *Solid State Physics*. Academic Press, 2000.

[41] A. Yariv and P. Yeh. *Optical Waves in Crystals: Propagation and Control of Laser Radiation*. Wiley, 1984.

[42] J. D. Joannopoulos and S. G. Johnson. *Photonic Crystals: The Road from Theory to Practice*. Kluwer Academic Pub, 2002.

[43] K. Sakoda. *Optical Properties Of Photonic Crystals*. Springer, 2004.

[44] K. K. Inoue and K. K. Ohtaka. *Photonic Crystals: Physics, Fabrication, and Applications*. Springer, 2004.

[45] K. Busch, S. Lölkes, R. B. Wehrspohn, and H. Föll. *Photonic Crystals: Advances in Design, Fabrication, and Characterization*. Wiley-VCH, 2004.

[46] J. M. Lourtioz, H. Benisty, V. Berger, J. M. Gérard, D. Maystre, A. Tchelnokov, and A. Tchelnokov. *Photonic Crystals: Towards Nanoscale Photonic Devices*. Springer, 2005.

[47] E. Yablonovitch, T. J. Gmitter, and K. M. Leung. Photonic band structure: The face-centered-cubic case employing nonspherical atoms. *Phys. Rev. Lett.*, **67** (17): 2295–2298, Oct 1991.

[48] C. C. Cheng, V. Arbet-Engels, A. Scherer, and E. Yablonovitch. Nanofabricated three dimensional photonic crystals operating at optical wavelengths. *Phys. Scr.*, **1996** (T68): 17–20, 1996.

[49] A. Chelnokov, K. Wang, S. Rowson, P. Garoche, and J. M. Lourtioz. Near-infrared Yablonovite-like photonic crystals by focused-ion-beam etching of macroporous silicon. *Appl. Phys. Lett.*, **77** (19): 2943 – 2945, 2000.

[50] C. Cuisin, A. Chelnokov, J. M. Lourtioz, D. Decanini, and Y. Chen. Sub-micrometer resolution Yablonovite templates fabricated by x-ray lithography. *Appl. Phys. Lett.*, **77** (6): 770 – 772, 2000.

[51] F. Romanato, D. Cojoc, E. D. Fabrizio, M. Galli, and D. Bajoni. X-ray and electron-beam lithography of three-dimensional array structures for photonics. *J. Vac. Sci. Technol., B*, **21** (6): 2912–2917, 2003.

[52] D. C. Meisel, M. Wegener, and K. Busch. Three-dimensional photonic crystals by holographic lithography using the umbrella configuration: Symmetries and complete photonic band gaps. *Phys. Rev. B*, **70** (16): 165104, 2004.

[53] S. Y. Lin, J. G. Fleming, D. L. Hetherington, B. K. Smith, W. Zubrzycki, S. R. Kurtz, J. Bur, R. Biswas, K. M. Ho, and M. M. Sigalas. A three-dimensional photonic crystal operating at infrared wavelengths. *Nature*, **394** (6690): 251–253, 1998.

[54] S. Noda, K. Tomoda, N. Yamamoto, and A. Chutinan. Full Three-Dimensional Photonic Bandgap Crystals at Near-Infrared Wavelengths. *Science*, **289** (5479): 604–606, 2000.

[55] M. Qi, E. Lidorikis, P. T. Rakich, S. G. Johnson, J. D. Joannopoulos, E. P. Ippen, and H. I. Smith. A three-dimensional optical photonic crystal with designed point defects. *Nature*, **429** (6991): 538–542, 2004.

[56] V. Berger, O. Gauthier-Lafaye, and E. Costard. Photonic band gaps and holography. *J. Appl. Phys.*, **82** (1): 60–64, 1997.

[57] M. Campbell, D. N. Sharp, M. T. Harrison, R. G. Denning, and A. J. Turberfield. Fabrication of photonic crystals for the visible spectrum by holographic lithography. *Nature*, **404** (6773): 53–6, 2000.

[58] Y. V. Miklyaev, D. C. Meisel, A. Blanco, G. von Freymann, K. Busch, W. Koch, C. Enrich, M. Deubel, and M. Wegener. Three-dimensional face-centered-cubic photonic crystal templates by laser holography: fabrication, optical characterization, and band-structure calculations. *Appl. Phys. Lett.*, **82** (8): 1284–1286, 2003.

[59] X. Wang, J. F. Xu, H. M. Su, Z. H. Zeng, Y. L. Chen, H. Z. Wang, Y. K. Pang, and W. Y. Tam. Three-dimensional photonic crystals fabricated by visible light holographic lithography. *Appl. Phys. Lett.*, **82** (14): 2212–2214, 2003.

[60] O. Toader, T. Y. M. Chan, and S. John. Photonic Band Gap Architectures for Holographic Lithography. *Phys. Rev. Lett.*, **92** (4): 043905, 2004.

[61] D. Gevaux. Three-dimensional photonic crystals - Microscale holography. *Nat. Phot.*, **1** (4): 213 – 213, 2007.

[62] F. Garcia-Santamaria, H. T. Miyazaki, A. Urquia, M. Ibisate, M. Belmonte, N. Shinya, F. Meseguer, and C. López. Nanorobotic manipulation of microspheres for on-chip diamond architectures. *Adv. Mater.*, **14** (16): 1144 – 1147, 2002.

[63] C. López. Materials aspects of photonic crystals. *Adv. Mater.*, **15** (20): 1679 – 1704, 2003.

[64] Y. A. Vlasov, V. N. Astratov, A. V. Baryshev, A. A. Kaplyanskii, O. Z. Karimov, and M. F. Limonov. Manifestation of intrinsic defects in optical properties of self-organized opal photonic crystals. *Phys. Rev. E*, **61** (5): 5784–5793, May 2000.

[65] R. Mayoral, J. Requena, J. S. Moya, C. López, A. Cintas, H. Miguez, F. Meseguer, L. Vazquez, M. Holgado, and A. Blanco. 3D long-range ordering in an SiO2 submicrometer-sphere sintered superstructure. *Adv. Mater.*, **9** (3): 257 – &, 1997.

[66] A. van Blaaderen, R. Ruel, and P. Wiltzius. Template-directed colloidal crystallization. *Nature*, **385** (6614): 321 – 324, 1997.

[67] P. Jiang, J. F. Bertone, K. S. Hwang, and V. L. Colvin. Single-Crystal Colloidal Multilayers of Controlled Thickness. *Chem. Mater.*, **11** (8): 2132–2140, 1999.

[68] Y. A. Vlasov, X.-Z. Bo, J. C. Sturm, and D. J. Norris. On-chip natural assembly of silicon photonic bandgap crystals. *Nature*, **414** (6861): 289–293, 2001.

[69] Y. Yin and Y. Xia. Growth of Large Colloidal Crystals with Their(100) Planes Orientated Parallel to the Surfaces of Supporting Substrates. *Adv. Mater.*, **14** (8): 605, 2002.

[70] S. Wong, V. Kitaev, and G. Ozin. Colloidal crystal films: Advances in universality and perfection. *JACS*, **125** (50): 15589 – 15598, 2003.

[71] A. Mihi, M. Ocana, and H. Miguez. Oriented colloidal-crystal thin films by spin-coating microspheres dispersed in volatile media. *Adv. Mater.*, **18** (17): 2244–2249, 2006.

[72] C. Jin, M. A. McLachlan, D. W. McComb, R. M. DeLaRue, and N. P. Johnson. Template-Assisted Growth of Nominally Cubic (100)-Oriented Three-Dimensional Crack-Free Photonic Crystals. *Nano Lett.*, **5** (12): 2646–2650, 2005.

[73] V. N. Astratov, Y. A. Vlasov, O. Z. Karimov, A. A. Kaplyanskii, Y. G. Musikhin, N. A. Bert, V. N. Bogomolov, and A. V. Prokofiev. Photonic band gaps in 3D ordered fcc silica matrices. *Phys. Lett. A*, **222** (5): 349 – 353, 1996.

[74] V. N. Astratov, Y. A. Vlasov, V. N. Bogomolov, A. A. Kaplyanskii, O. Z. Karimov, D. A. Kurdjukov, and A. V. Prokofiev. Influence of refractive index contrast on photonic band gap in 3D periodic SiO2 matrices filled with a semiconductor. In *Compound Semiconductors 1996*, number 155 in Institute Of Physics Conference Series, pages 73 – 76. IOP Publishing LTD, 1997.

[75] O. D. Velev, T. A. Jede, R. F. Lobo, and A. M. Lenhoff. Porous silica via colloidal crystallization. *Nature*, **389** (6650): 447–448, 1997.

[76] J. E. G. J. Wijnhoven and W. L. Vos. Preparation of Photonic Crystals Made of Air Spheres in Titania. *Science*, **281** (5378): 802–804, 1998.

[77] A. Arsenault, F. Fleischhaker, G. von Freymann, V. Kitaev, H. Miguez, A. Mihi, N. Tetreault, E. Vekris, I. Manners, S. Aitchison, D. Perovic, and G. A. Ozin. Perfecting imperfection - Designer defects in colloidal photonic crystal. *Adv. Mater.*, **18** (20): 2779 – 2785, 2006.

[78] R. Pozas, A. Mihi, M. Ocana, and H. Miguez. Building nanocrystalline planar defects within self-assembled photonic crystals by spin-coating. *Adv. Mater.*, **18** (9): 1183, 2006.

[79] J. F. Galisteo-López, M. Galli, L. C. Andreani, A. Mihi, R. Pozas, M. Ocana, and H. Miguez. Phase delay and group velocity determination at a planar defect state in three dimensional photonic crystals. *Appl. Phys. Lett.*, **90** (10): 101113, 2007.

[80] M. Egen, R. Voss, B. Griesebock, R. Zentel, S. Romanov, and C. S. Torres. Heterostructures of polymer photonic crystal films. *Chem. Mater.*, **15** (20): 3786 – 3792, 2003.

[81] Y. X. Zhao, K. Wostyn, G. de schaetzen, K. Clays, L. Hellemans, A. Persoons, M. Szekeres, and R. A. Schoonheydt. The fabrication of photonic band gap materials with a two-dimensional defect. *Appl. Phys. Lett.*, **82** (21): 3764 – 3766, 2003.

[82] J. V. Sanders. Colour of precious opal. *Nature*, **204** (4964): 1151–1153, 1964.

[83] J. V. Sanders. Diffraction of light by opals. *Acta Crystallogr., Sect. A: Found. Crystallogr.*, **24** (4): 427–434, 1968.

[84] V. N. Astratov, V. N. Bogomolov, A. A. Kaplyanskii, A. V. Prokofiev, L. A. Samoilovich, S. M. Samoilovich, and Y. A. Vlasov. Optical spectroscopy of opal matrices with CdS embedded in its pores: Quantum confinement and photonic band gap effects. *Nuovo Cimento Soc. Ital. Fis., D*, **17** (11-12): 1349 – 1354, 1995.

[85] H. S. Sözüer, J. W. Haus, and R. Inguva. Photonic bands: Convergence problems with the plane-wave method. *Phys. Rev. B*, **45** (24): 13962–13972, Jun 1992.

[86] A. Moroz. Three-Dimensional Complete Photonic-Band-gap Structures in the Visible. *Phys. Rev. Lett.*, **83** (25): 5274–5277, Dec 1999.

[87] K. M. Ho, C. T. Chan, and C. M. Soukoulis. Existence of a photonic gap in periodic dielectric structures. *Phys. Rev. Lett.*, **65** (25): 3152–3155, Dec 1990.

[88] K. W. K. Shung and Y. C. Tsai. Surface effects and band measurements in photonic crystals. *Phys. Rev. B*, **48** (15): 11265–11269, Oct 1993.

[89] D. M. Mittleman, J. F. Bertone, P. Jiang, K. S. Hwang, and V. L. Colvin. Optical properties of planar colloidal crystals: Dynamical diffraction and the scalar wave approximation. *J. Chem. Phys.*, **111** (1): 345–354, 1999.

[90] A. Mihi, H. Miguez, I. Rodriguez, S. Rubio, and F. Meseguer. Surface resonant modes in colloidal photonic crystals. *Phys. Rev. B*, **71** (12): 125131, 2005.

[91] K. S. Yee. Numerical solution of boundary value problems involving Maxwell equations in isotropic media. *IEEE Transactions on Antennas and Propagation*, **14** (3): 302–307, 1966.

[92] A. Chutinan and S. John. Diffractionless flow of light in two- and three-dimensional photonic band gap heterostructures: Theory, design rules, and simulations. *Phys. Rev. E*, **71** (2): 026605, 2005.

[93] J. B. Pendry and A. MacKinnon. Calculation of photon dispersion relations. *Phys. Rev. Lett.*, **69** (19): 2772–2775, Nov 1992.

[94] A. Reynolds, F. López-Tejeira, D. Cassagne, F. J. García-Vidal, C. Jouanin, and J. Sánchez-Dehesa. Spectral properties of opal-based photonic crystals having a SiO_2 matrix. *Phys. Rev. B*, **60** (16): 11422–11426, Oct 1999.

[95] D. Cassagne, A. Reynolds, and C. Jouanin. Modelling of 3D photonic crystals based on opals. *Opt. Quantum Electron.*, **32** (6): 923–933, 2000.

[96] S. G. Romanov, T. Maka, C. M. Sotomayor Torres, M. Müller, R. Zentel, D. Cassagne, J. Manzanares-Martinez, and C. Jouanin. Diffraction of light from thin-film polymethylmethacrylate opaline photonic crystals. *Phys. Rev. E*, **63** (5): 056603, Apr 2001.

[97] V. Yannopapas, N. Stefanou, and A. Modinos. Theoretical analysis of the photonic band structure of face-centred cubic colloidal crystals. *J. Phys.: Condens. Matt.*, **9** (46): 10261–10270, 1997.

[98] N. Stefanou, V. Yannopapas, and A. Modinos. Heterostructures of photonic crystals: frequency bands and transmission coefficients. *Comput. Phys. Commun.*, **113** (1): 49 – 77, 1998.

[99] V. Yannopapas, N. Stefanou, and A. Modinos. Effect of Stacking Faults on the Optical Properties of Inverted Opals. *Phys. Rev. Lett.*, **86** (21): 4811–4814, May 2001.

[100] N. Stefanou, V. Yannopapas, and A. Modinos. MULTEM 2: A new version of the program for transmission and band-structure calculations of photonic crystals. *Comput. Phys. Commun.*, **132** (1-2): 189 – 196, 2000.

[101] L. A. Dorado, R. A. Depine, and H. Miguez. Effect of extinction on the high-energy optical response of photonic crystals. *Phys. Rev. B*, **75** (24): 241101, 2007.

[102] I. I. Tarhan and G. H. Watson. Photonic band structure of fcc colloidal crystals. *Phys. Rev. Lett.*, **76** (2): 315–318, Jan 1996.

[103] V. N. Astratov, A. M. Adawi, S. Fricker, M. S. Skolnick, D. M. Whittaker, and P. N. Pusey. Interplay of order and disorder in the optical properties of opal photonic crystals. *Phys. Rev. B*, **66** (16): 165215, 2002.

[104] J. F. Galisteo-López, E. Palacios-Lidón, E. Castillo-Martínez, and C. López. Optical study of the pseudogap in thickness and orientation controlled artificial opals. *Phys. Rev. B*, **68** (11): 115109, Sep 2003.

[105] E. Pavarini, L. C. Andreani, C. Soci, M. Galli, F. Marabelli, and D. Comoretto. Band structure and optical properties of opal photonic crystals. *Phys. Rev. B*, **72** (4): 045102, 2005.

[106] J. F. Galisteo-López and C. López. High-energy optical response of artificial opals. *Phys. Rev. B*, **70** (3): 035108, 2004.

[107] H. Miguez, V. Kitaev, and G. A. Ozin. Band spectroscopy of colloidal photonic crystal films. *Appl. Phys. Lett.*, **84** (8): 1239–1241, 2004.

[108] M. Notomi. Theory of light propagation in strongly modulated photonic crystals: Refractionlike behavior in the vicinity of the photonic band gap. *Phys. Rev. B*, **62** (16): 10696 – 10705, 2000.

[109] H. Kosaka, T. Kawashima, A. Tomita, M. Notomi, T. Tamamura, T. Sato, and S. Kawakami. Superprism phenomena in photonic crystals. *Phys. Rev. B*, **58** (16): R10096–R10099, Oct 1998.

[110] L. J. Wang, A. Kuzmich, and A. Dogariu. Gain-assisted superluminal light propagation. *Nature*, **406** (6793): 277 – 279, 2000.

[111] A. Dogariu, A. Nahata, R. A. Linke, L. J. Wang, and R. Trebino. Optical pulse propagation through metallic nano-apertures. *Appl. Phys. B*, **74**: S69 – S73, 2002.

[112] G. Dolling, C. Enrich, M. Wegener, C. M. Soukoulis, and S. Linden. Simultaneous negative phase and group velocity of light in a metamaterial. *Science*, **312** (5775): 892 – 894, 2006.

[113] M. Soljacic, S. G. Johnson, S. H. Fan, M. Ibanescu, E. Ippen, and J. D. Joannopoulos. Photonic-crystal slow-light enhancement of nonlinear phase sensitivity. *J. Opt. Soc. Am. B*, **19** (9): 2052 – 2059, 2002.

[114] H. Gersen, T. J. Karle, R. J. P. Engelen, W. Bogaerts, J. P. Korterik, N. F. van hulst, T. F. Krauss, and L. Kuipers. Real-space observation of ultraslow light in photonic crystal waveguides. *Phys. Rev. Lett.*, **94** (7): 073903, 2005.

[115] Y. A. Vlasov, M. O'boyle, H. F. Hamann, and S. J. Mcnab. Active control of slow light on a chip with photonic crystal waveguides. *Nature*, **438** (7064): 65 – 69, 2005.

[116] Y. A. Vlasov, V. N. Astratov, O. Z. Karimov, A. A. Kaplyanskii, V. N. Bogomolov, and A. V. Prokofiev. Existence of a photonic pseudogap for visible light in synthetic opals. *Phys. Rev. B*, **55** (20): R13357–R13360, May 1997.

[117] D. M. Whittaker and I. S. Culshaw. Scattering-matrix treatment of patterned multilayer photonic structures. *Phys. Rev. B*, **60** (4): 2610–2618, Jul 1999.

[118] P. Lalanne. Electromagnetic analysis of photonic crystal waveguides operating above the light cone. *IEEE J. Quantum Electron.*, **38** (7): 800–804, 2002.

[119] S. Tikhodeev, A. Yablonskii, E. Muljarov, N. Gippius, and T. Ishihara. Quasiguided modes and optical properties of photonic crystal slabs. *Phys. Rev. B*, **66** (4): 45102, 2002.

[120] A. Balestreri, L. C. Andreani, and M. Agio. Optical properties and diffraction effects in opal photonic crystals. *Phys. Rev. E*, **74** (3): 036603, 2006.

[121] S. G. Johnson and J. D. Joannopoulos. Three-dimensionally periodic dielectric layered structure with omnidirectional photonic band gap. *Appl. Phys. Lett.*, **77** (22): 3490–3492, 2000.

[122] M. Galli, F. Marabelli, and G. Guizzetti. Direct measurement of refractive-index dispersion of transparent media by white-light interferometry. *Appl. Opt*, **42**: 3910–3914, 2003.

[123] N. G. Sultanova, I. D. Nikolov, and C. D. Ivanov. Measuring the refractometric characteristics of optical plastics. *Opt. Quantum Electron.*, **35** (1): 21–34, 2003.

[124] M. Galli, D. Bajoni, F. Marabelli, L. C. Andreani, L. Pavesi, and G. Pucker. Photonic bands and group-velocity dispersion in Si/SiO_ {2} photonic crystals from white-light interferometry. *Phys. Rev. B*, **69** (11): 115107, 2004.

[125] F. López-Tejeira, T. Ochiai, K. Sakoda, and J. Sánchez-Dehesa. Symmetry characterization of eigenstates in opal-based photonic crystals. *Phys. Rev. B*, **65** (19): 195110, Apr 2002.

[126] W. Lee, S. A. Pruzinsky, and P. V. Braun. Multi-Photon Polymerization of Waveguide Structures Within Three-Dimensional Photonic Crystals. *Adv. Mater.*, **14** (4): 271, 2002.

[127] N. Tetreault, H. Miguez, S. Yang, V. Kitaev, and G. Ozin. Refractive index patterns in silicon inverted colloidal photonic crystals. . *Adv. Mater.*, **15** (14): 1167–1172, 2003.

[128] B. H. Juarez, D. Golmayo, P. A. Postigo, and C. López. Selective formation of inverted opals by electron-beam lithography. *Adv. Mater.*, **16** (19): 1732–1736, 2004.

[129] E. Vekris, V. Kitaev, G. von Freymann, D. D. Perovic, J. S. Aitchison, and G. A. Ozin. Buried Linear Extrinsic Defects in Colloidal Photonic Crystals. *Adv. Mater.*, **17** (10): 1269–1272, 2005.

[130] Y. Jun, C. A. Leatherdale, and D. J. Norris. Tailoring air defects in self-assembled photonic bandgap crystals. *Adv. Mater.*, **17** (15): 1908–1911, 2005.

[131] P. Massé, S. Reculusa, K. Clays, and S. Ravaine. Tailoring planar defects in three-dimensional colloidal crystals. *Chem. Phys. Lett*, **422**: 251, 2006.

[132] E. Palacios-Lidón, J. F. Galisteo-López', B. H. Juarez, and C. López. Engineered planar defects embedded in opals. *Adv. Mater.*, **16** (4): 341–345, 2004.

[133] N. Tetreault, A. Mihi, H. Miguez, I. Rodriguez, G. A. Ozin, F. Meseguer, and V. Kitaev. Dielectric Planar Defects in Colloidal Photonic Crystal Films. *Adv. Mater.*, **16** (4): 346–349, 2004.

[134] P. P. Ewald. Zur Theorie der Interferenzen der Röntgenstrahlen. *Physik Z*, **14**: 465–472, 1913.

[135] P. P. Ewald. Zur Begründung der Kristalloptik. III. Röntgenstrahlen. *Ann. Phys.*, **54**: 519–597, 1917.

[136] P. P. Ewald. Crystal Optics for Visible Light and X Rays. *Rev. Mod. Phys.*, **37** (1): 46–56, Jan 1965.

[137] V. Mocella. Negative refraction in Photonic Crystals: thickness dependence and Pendellösung phenomenon. *Opt. Express*, **13** (5): 1361–1367, 2005.

[138] A. Dogariu, A. Kuzmich, H. Cao, and L. Wang. Superluminal light pulse propagation via rephasing in a transparent anomalously dispersive medium. *Opt. Express*, **8** (6): 344–350, 2001.

[139] J. F. Galisteo-López, M. Galli, A. Balestreri, M. Patrini, L. C. Andreani, and C. López. Slow to superluminal light waves in thin 3D photonic crystals. *Opt. Express*, **15** (23): 15342–15350, 2007.

[140] H. Miguez, S. Yang, N. Tetreault, and G. Ozin. Oriented Free-Standing Three-Dimensional Silicon Inverted Colloidal Photonic Crystal Microfibers. *Adv. Mater.*, **14** (24): 1805–1808, 2002.

[141] Y. Yin, Z. Y. Li, and Y. Xia. Template-directed growth of (100)-oriented colloidal crystals. *Langmuir*, **19** (3): 622–631, 2003.

[142] E. Palacios-Lidón, A. Blanco, M. Ibisate, F. Meseguer, C. López, and J. Sánchez-Dehesa. Optical study of the full photonic band gap in silicon inverse opals. *Appl. Phys. Lett.*, **81** (26): 4925–4927, 2002.

[143] J. F. Galisteo-López, M. Galli, A. Balestreri, L. C. Andreani, and C. López. Optical response of artificial opals oriented along the ΓX direction. *Appl. Phys. Lett.*, **90** (23): 231112, 2007.

[144] P. D. García, J. F. Galisteo-López, and C. López. Tuning and optical study of the ΓX and ΓL photonic pseudogaps in opals. *Appl. Phys. Lett.*, **87** (20): 201109, 2005.

List of personal publications

- J.F. Galisteo-López, M. Galli, A. Balestreri, M. Patrini, L.C. Andreani, C. López, *Slow to superluminal light waves in thin 3D photonic crystals*, Opt. Express **15** (23), 15342-15350 (2007)

- J.F. Galisteo-López, M. Galli, A. Balestreri, L.C. Andreani, and C. López, *Optical response of artificial opals oriented along the ΓX direction*, Appl. Phys. Lett. **90**, 231112 (2007)

- A. Balestreri, L.C. Andreani, M. Agio, *Optical properties and diffraction effects in opal photonic crystals*, Phys. Rev. E **74** (3), 036603 (2006); Phys. Rev. E **75** (5), 059906E (2007)

- L. Pallavidino, D.S. Razo, F. Geobaldo, A. Balestreri, D. Bajoni, M. Galli, L.C. Andreani, C. Ricciardi, E. Celasco, M. Quaglio, F. Giorgis, *Synthesis, characterization and modelling of silicon based opals*, J. Non-Cryst. Sol. **352** (9-20), 1425-1429 (2006)

- J.F. Galisteo-López, M. Galli, M. Patrini, A. Balestreri, L.C. Andreani, C. López *Effective refractive index and group velocity determination of three-dimensional photonic crystals by means of white light interferometry*, Phys. Rev. B **73** (12), 125103 (2006)